Deposit & Copying of Dissertation Declaration

UNIVERSITY OF CAMBRIDGE

Board of Graduate Studies

Please note that you will also need to bind a copy of this Declaration into your final, hardbound copy of thesis - this has to be the very first page of the hardbound thesis.

1	Surname (Family Name)	Forenames(s)	Title
2	Title of Dissertation as approved by the Degree Committee		

In accordance with the University Regulations in *Statutes and Ordinances* for the PhD, MSc and MLitt Degrees, I agree to deposit one print copy of my dissertation entitled above and one print copy of the summary with the Secretary of the Board of Graduate Studies who shall deposit the dissertation and summary in the University Library under the following terms and conditions:

1. Dissertation Author Declaration

I am the author of this dissertation and hereby give the University the right to make my dissertation available in print form as described in 2. below.

My dissertation is my original work and a product of my own research endeavours and includes nothing which is the outcome of work done in collaboration with others except as declared in the Preface and specified in the text. I hereby assert my moral right to be identified as the author of the dissertation.

The deposit and dissemination of my dissertation by the University does not constitute a breach of any other agreement, publishing or otherwise, including any confidentiality or publication restriction provisions in sponsorship or collaboration agreements governing my research or work at the University or elsewhere.

2. Access to Dissertation

I understand that one print copy of my dissertation will be deposited in the University Library for archival and preservation purposes, and that, unless upon my application restricted access to my dissertation for a specified period of time has been granted by the Board of Graduate Studies prior to this deposit, the dissertation will be made available by the University Library for consultation by readers in accordance with University Library Regulations and copies of my dissertation may be provided to readers in accordance with applicable legislation.

3	Signature	Date

Corresponding Regulation

Before being admitted to a degree, a student shall deposit with the Secretary of the Board one copy of his or her hard-bound dissertation and one copy of the summary (bearing student's name and thesis title), both the dissertation and the summary in a form approved by the Board. The Secretary shall deposit the copy of the dissertation together with the copy of the summary in the University Library where, subject to restricted access to the dissertation for a specified period of time having been granted by the Board of Graduate Studies, they shall be made available for consultation by readers in accordance with University Library Regulations and copies of the dissertation provided to readers in accordance with applicable legislation.

UNIVERSITY OF CAMBRIDGE

Direct numerical simulation of particulate flows in viscoplastic media

Arndt Ryo Koblitz

St. Catharine's College

The Laboratory for Scientific Computing,
Cavendish Laboratory,
University of Cambridge

February 2019

This dissertation is submitted for the degree of Doctor of Philosophy

Declaration

Cavendish Laboratory
February 2019

This dissertation is the result of my own work and includes nothing which is the outcome of work done in collaboration except as declared in the Preface and specified in the text. It is not substantially the same as any that I have submitted, or, is being concurrently submitted for a degree or diploma or other qualification at the University of Cambridge or any other University or similar institution except as declared in the Preface and specified in the text. I further state that no substantial part of my dissertation has already been submitted, or, is being concurrently submitted for any such degree, diploma or other qualification at the University of Cambridge or any other University of similar institution except as declared in the Preface and specified in the text. It does not exceed the limit of sixty thousand words prescribed by the Degree Committee for Physics and Chemistry.

Arndt R. Koblitz

Abstract

Direct numerical simulation of particulate flows in viscoplastic media

Arndt Ryo Koblitz

The oilfield primary cementing process is vital to successful and safe extraction. It is the first cementing operation performed after the casing string has been placed in the newly drilled wellbore, and is critical to prevent loss of well control or contamination of water sources. While a conceptually simple operation, real-world cementing operations are complicated by a slew of operation specific issues such as high wellbore deviation, weak formation walls, and high bottom hole formation pressure. This makes a quantitative understanding of the cement slurry rheology imperative. Cement slurry rheometry can be difficult in practice due to its non-linear stress-strain behaviour. Complicating matters further, the cement slurries we are interested in contain suspensions of relatively large particles—micro beads—that are problematic for convential measurement tools such as concentric cylinder rheometers. This motivates a computational treatment.

There are two overriding aspects to modelling suspensions in viscoplastic fluid flows. Firstly, for fully resolved particle suspensions—regardless of the carrier fluid—the discretisation scheme must cope with disparate length scales at the particle boundaries and wider flow field. In this work we adopt the overset grid method, allowing each particle to be explicitly represented with a curvilinear grid, thereby enabling cost-effective resolution of boundary layer flows. Secondly, the governing equations of viscoplatic fluid flow are non-linear, even

in the absence of inertia, requiring specialised solution strategies. We adopt an augmented Lagrangian approach that allows for an exact treatment of the constitutive equation, enabling truly unyielded zones in our solutions.

Even with an efficient discretisation scheme, the solution of viscoplatic fluid flow problems remains prohibitively expensive. In this work, we are primarily interested in yield stress effects, and so we use the ideal Bingham constitutive model as a proxy for our cement slurry. We begin by investigating the viscoplatic squeeze flow between approaching particles, finding that under certain conditions yield stress effects external to the closing gap contribute greatly to the lubrication force. This enables viscoplastic lubrication theory to be used as a sub-grid scale model in coarse grained suspension simulations.

By restricting ourselves to quasi-steady, non-inertial, two-dimensional suspensions of infinite circular cylinders we are able to simulate suspension flows with two orders of magnitude more particles than in the literature. We first investigate the yielding transition in negatively buoyant suspensions under quiescent flow conditions. We identify three distinct sedimentation regimes, including a mixed regime where clusters of particles preferentially settle while isolated particles remain fixed. Finally, we investigate neutrally buoyant suspensions under shear, where we find that unyielded material may act as additional particles, increasing the apparent solid volume fraction, and extend an existing micro-mechanical model to take this in to account.

Acknowledgements

Firstly I wish to thank my academic and industrial supervisors, Dr Nikos Nikiforakis and Dr Sean Lovett, who provided much valuable advice, mentorship and encouragement. I also wish to thank Dr Paul Hammond and Dr Franck Monmont of Schlumberger Cambridge Research for many useful discussions and careful reading of the article manuscripts, and gratefully acknowledge the financial support of Schlumberger Cambridge Research.

Chapter 5 is the product of working closely with Prof Bill Henshaw of Rensselaer Polytechnic Institute, New York, whose support with the Overture codebase was invaluable.

I am fortunate to have benefited from fantastic educators throughout my schooling, who have all influenced my eventual academic path, and am particularly grateful to Matthew Farthing, Prof Ian Eames, and Dr Hendrik Ülpre.

I am grateful to my parents, Yasue and Donald Koblitz, who have always been supportive of my academic studies, and to my sisters, Ariana and Avril, who made me graft that little bit harder by continuously raising the bar, in all aspects.

Finally, I thank my wife, Yifan Li, for never wavering in her support, even when my studies at times placed an unfair burden upon her.

Contents

List of Figures

List of Tables

Nomenclature

Greek Symbols

δ	Subgrid stabilisation term, page 42
$[\eta]$	Intrinsic viscosity, page 119
ϵ	Small constant, page 19
η	Plastic viscosity, page 17
$\dot{\boldsymbol{\gamma}}$	Rate-of-strain tensor, page 16
$\dot{\Gamma}$	Macroscopic shear rate, page 114
$\dot{\gamma}_{\mathrm{local}}$	Locate shear rate, page 81
Γ	Body surface, page 33
$\tilde{\dot{\gamma}}$	Average local shear rate, page 114
$\tilde{\dot{\gamma}}_e$	Effective average local shear rate, page 126
Λ	Normalised second invariant of the velocity gradient tensor, page 74
λ	Lagrange multiplier field, page 41
λ	Second coefficient of viscosity, page 16
μ	Scalar viscosity coefficient, page 16
ν	Kinematic viscosity, page 31

Ω Domain, page 96

ω Angular velocity, page 32

$\partial\Omega$ Domain boundary, page 96

$\hat{\Phi}$ Viscous dissipation, page 74

ϕ Solid volume fraction, page 92

$\phi_{\max}$ Maximum packing fraction, page 119

ϕ_e Excluded volume fraction, page 124

$\tilde{\phi}$ Effective solid volume fraction, page 124

ρ Density, page 31

ρ_f Fluid density, page 48

ρ_p Particle density, page 48

ρ_r Density ratio, page 10

ρ_r Density ratio, page 55

σ Total stress tensor, page 16

τ Deviatoric stress tensor, page 16

τ_f Fluid relaxation time, page 54

τ_p Particle relaxation time, page 54

τ_y Yield stress, page 17

Roman Symbols

A Moment of inertia tensor, page 32

$a(\boldsymbol{v}, \boldsymbol{w})$ Viscous dissipation functional, page 108

B^*	Gap Bingham number, page 72
Bn	Bingham number, page 17
B	Particle Bingham number, page 108
$\boldsymbol{e}_i$	Principal axes of inertia, page 33
e_{global}	Global energy dissipation, page 117
e_{local}	Local energy dissipation, page 117
$\boldsymbol{F}$	Applied force, page 33
$\boldsymbol{f}$	Body force, page 31
$\mathcal{G}$	Composite grid, page 27
$\mathcal{G}_k$	Component grid where $k = 1, 2, \dots N_g$, page 27
$\mathrm{g}(\phi)$	Newtonian response, page 116
H	Minimum separation distance, page 68
h	Non-dimensional separation distance, page 74
I	Identity tensor, page 16
$j(\boldsymbol{v})$	Plastic dissipation functional, page 108
K	Consistency index, page 19
$\hat{l}'$	Characteristic length scale, page 91
$\mathcal{L}$	Characteristic length scale, page 17
$L(\boldsymbol{v})$	Buoyancy work functional, page 108
m_b	Mass of the body, page 32
n	Flow index, page 19

N_g	Number of component grids forming a composite grid, page 27
∂P	Particle boundary, page 96
P	Particle, page 96
p	Hydrostatic pressure, page 16
$\boldsymbol{q}$	Auxiliary tensor, page 41
Re	Reynolds number, page 10
r	Penalty parameter, page 42
Stk	Stokes number, page 54
$\boldsymbol{T}$	Applied torque, page 33
$\hat{U}_p$	Particle settling velocity, page 108
$\mathcal{U}$	Characteristic velocity scale, page 17
u	Velocity vector, page 16
U_w	Wall velocity, page 75
$\boldsymbol{v}_b$	Velocity of the centre of mass, page 32
$\langle \hat{V}_{\phi,Y} \rangle$	Mean suspension settling velocity, page 99
V	Approach velocity, page 68
$\hat{W}$	Rate of working the fluid, page 74
$\boldsymbol{x}_b$	Position of the centre of mass, page 32
X	Plug boundary location, page 73
Y	Yield number, page 91
Y_0^*	Critical yield number for an isolated body, page 91
Y_ϕ^*	Critical yield number for a given solid volume fraction, page 92

1 Introduction

The oil and gas industry uses many complex fluids in a wide range of applications. These fluids are usually Wn-Newtonian in character and possess a variety of characteristics which are not well understood, such as viscoelasticity (polymeric fluids such as those used in hydraulic fracturing), viscoplasticity (yield stress fluids such as cement slurries) and time-dependency (structure forming fluids such as drilling mud). Many of these characteristics originate from local microscopic interactions in the fluid, particularly in complex fluids containing particle or polymer molecule additives. In such fluids the interactions between the suspended material, the suspension fluid, and the domain boundaries give rise to non-Newtonian characteristics of the bulk fluid.

The objective of this project is to better understand the physics of viscoplastic fluids containing non-colloidal particles. Particle-laden fluids are encountered in a large number of relevant oilfield operations, including well cementing (both primary and remedial), hydraulic fracturing, wellbore cleanup, and gravel packing. This work is focused on the primary cementing operation.

1.1 Primary cementing process

The oilfield primary cementing process is vital to successful and safe extraction. It is the first cementing operation performed after the steel casing string has been lowered into the newly drilled wellbore. The primary objective is to ensure zonal isolation between different parts of the rock formation, viz. the prevention of uncontrolled fluid (liquid and gas) communication between zones, by forming a hydraulic seal between the casing and cement, and the cement and formation.

Failure to do so can result in loss of well control or contamination of water sources (Abbas *et al.*, 2002). Other objectives include preventing corrosion of the casing, providing strength for installation of wellhead equipment, and providing pressure integrity.

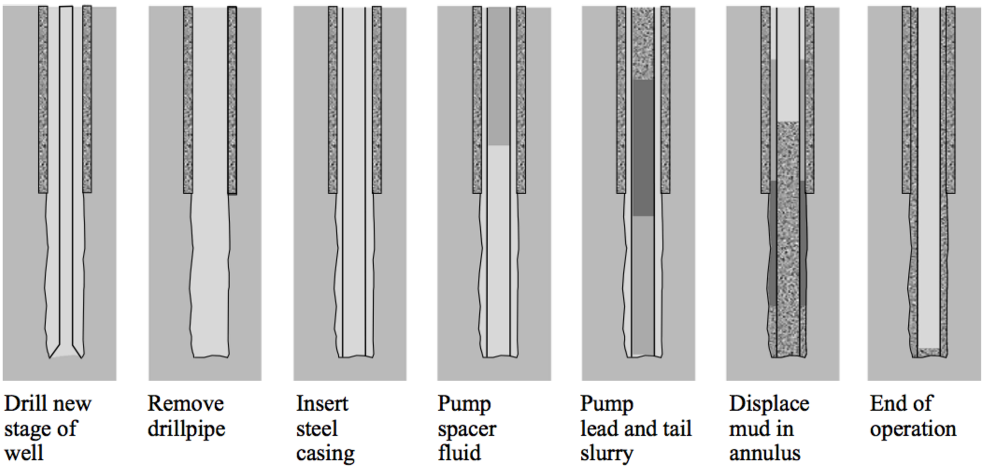

FIGURE 1.1: Schematic of the basic primary cementing operation without plugs (Malekmohammadi *et al.*, 2010).

Figure fig. 1.1 shows a schematic representation of the basic primary cementing operation. After a new stage of the well has been drilled the drill pipe is removed and a casing string run down the length of the borehole, typically with an annular gap of approximately 2 cm between the outside of the casing and the formation wall (Malekmohammadi *et al.*, 2010), although this can vary between 3–80 mm due to casing eccentricity (Roustaei *et al.*, 2015). At this stage, a sequence of fluids is pumped into the well to displace the drilling mud and clean the formation and casing walls. Generally, a low viscosity spacer fluid is pumped first, where the low viscosity allows for turbulent pipe flow beneficial to mud displacement at practical pumping rates (Bittleston, 1991). This is followed by a cement slurry and finally drilling mud. The cement is pumped down to the bottom of the casing and back up the annular gap between formation wall and casing at least past the production zone, but typically higher in order to prevent casing corrosion or freshwater contamination. A few meters of cement are left in the bottom of the hole, which is later drilled out when drilling of the new wellbore stage is commenced.

From the late 1970s onward there has been increasing interest in horizontal well bores, with a fairly recent surge as producers seek to maximise production from existing sites and tap harder to reach reserves. Cased completion in horizontal wells is necessary because, generally, the formations are horizontally heterogeneous. In fact, the heterogeneity can be exploited by guiding the wellbore through natural fracture systems. This requires zonal isolation to prevent fluid loss (Brown *et al.*, 1990). Zonal isolation may be achieved through a number of means other than primary cementing, such as casing packers and slotted or perforated liners. However, cementing remains the most successful means of ensuring zonal isolation and is, in fact, mandatory for injection wells unless substantial evidence that no contamination of underground drinking water would result (40 C.F.R. §146.32).

The success of a primary cementing operation depends heavily on the ability to control the rheology of the cement slurry. The schematic shown in figure 1.1 is an idealisation that does not convey the immense challenges faced by real world cementing operations: with longer/deeper wells fluid loss from the cement slurry to the formation becomes more problematic; as mentioned before, wells can be highly deviated and even horizontal, making gravitational settling of suspended material an important consideration; formation walls may have imperfections (washouts) that negatively impact mud removal and thus cementing; high bottom hole formation pressure can make it difficult to control well fluids without increased slurry density, conversely, low density slurries may be needed to reduce hydrostatic pressure where formations are weak. Initially, cementing guidelines were based on field observations and basic experimentation (Bittleston, 1991). While these guidelines were—to an extent—successful, they failed to prevent problems in many primary cementing jobs (Bittleston, 1991). As well bores become more ambitious in their reach, deviation angle and surrounding formations, flexibility in cement performance is required (Nelson, 1990; Brown *et al.*, 1990). To achieve this, additives are continually developed to control properties of the set cement, such as strength, porosity and durability, and physical properties of the slurry, such as density, viscosity and yield stress.

1.2 Motivation and outline

Increasingly difficult drilling operations and resulting high performance cement requirements necessitate a quantitative understanding of the cement slurry rheology in order to improve cementing guidelines. To that end, there has been growing interest in performing resolved direct numerical simulations of particulate flows in non-Newtonian carrier fluids in order to predict the macroscopic effect of added non-Brownian particles on the flow properties of cement. From a numerical standpoint, there are two overriding aspects of the problem that are particularly challenging: the particle–particle, particle–wall, and particle–fluid interactions; and the non-linear behaviour of the viscoplastic carrier fluid.

The investigations in this work are relevant to the final two stages of the cementing operation depicted in figure fig. 1.1. An important aspect of the penultimate displacement stage is the shear response of the slurry mixture. We investigate this in Chapter chapter 8 through an idealised system of neutrally buoyant, rigid particles in a Bingham plastic fluid under simple shear. Likewise, we investigate the stability of suspended bodies in the slurry mixture after the cessation of pumping through an idealised system of negatively buoyant, rigid particles in a Bingham plastic fluid in Chapter chapter 7. The squeeze flow behaviour investigated in Chapter chapter 6 is relevant to both the displacement and flow cessation stages of the basic primary cementing process.

The dissertation is organised as follows. Chapter 2 provides an overview of discretisation techniques used in fluid structure interaction problems, and Chapter 3 an overview of viscoplastic modelling techniques, both in the context of particle laden flows. Chapter 4 explores the numerical methods used in this work in more detail, starting with a thorough description of the discretisation method chosen for the fluid structure interaction before examining the Newtonian and non-Newtonian flow solvers. The overset grid methodology is evaluated for particle laden flow simulations in Chapter 5, using Newtonian carrier fluids only. In the following three chapters we explore viscoplastic particle laden flows beginning with micro-scale particle–particle interactions in chapter 6 before exploring large scale suspension sedimentation and shear experiments in Chapter

7 and 8, respectively. The dissertation concludes with a summary in Chapter 9.

1.3 Main contributions

The main scientific contributions of this work are as follows.

Aspects of the work in this dissertation have been presented in the following publications with co-author contributions made explicit where applicable:

- **A.R. Koblitz**, S. Lovett, N. Nikiforakis & W.D. Henshaw 2017 Direct numerical simulation of particulate flows with an overset grid method. *J. Comp. Phys.* **343**, 414–431.
  An efficient overset grid method is evaluated for two- and three-dimensional simulations with arbitrarily moving rigid bodies. The method is found to perform favourably in terms of accuracy and efficiency for problems involving large domains and where moving bodies are strongly influenced by the resolution of boundary layers.

  ARK and SL conceived of the idea. WDH developed and implemented the code. **ARK** planned and carried out the simulations and analysed the data. **ARK** wrote the manuscript in consultation with WDH, and SL while NN supervised the project.

- **A.R. Koblitz**, S. Lovett & N. Nikiforakis 2018 Viscoplastic squeeze flow between two identical infinite circular cylinders. *Phys. Rev. Fluids.* **3**, 023301.
  The interstitial squeeze flow between two approaching cylinders in a viscoplastic medium is studied numerically and semi-analytically. Yield stress effects external to the gap—not picked up by viscoplastic lubrication theory—are found to significantly affect the lubrication pressure.

  ARK and SL conceived of the idea. SL and **ARK** performed the analytic calculations, while **ARK** designed and carried out the simulations. **ARK** and SL analysed the data and developed the narrative jointly. **ARK** wrote the manuscript in consultation with SL and NN.

- **A.R. Koblitz**, S. Lovett & N. Nikiforakis 2018 Direct numerical simulation of particle sedimentation in a Bingham fluid. *Phys. Rev. Fluids*. **3**, 093302.
  Two-dimensional numerical simulations of a suspension of sedimenting particles in a Bingham fluid find three possible regimes: all, a fraction, and none of the particles sedimenting.

  ARK conceived of the idea, planned, and carried out the simulations. **ARK** and SL analysed the data and developed the narrative jointly. **ARK** wrote the manuscript in consultation with SL and NN.

- **A.R. Koblitz**, S. Lovett & N. Nikiforakis 2018 Reduced effective viscosity in viscoplastic suspension flows: a shadow region effect. (*in preparation*)

  ARK and SL conceived of the idea, and planned the numerical experiments. **ARK** carried out the simulations and analysed the data. **ARK** developed the narrative, and wrote the manuscript in consultation with SL and NN.

and additionally at the following conferences:

- **A.R. Koblitz**, S. Lovett, N. Nikiforakis 2017 Interacting circular cylinders in viscoplastic media *British Society of Rheology Mid-Winter Meeting, Bristol, U.K.*
- **A.R. Koblitz**, S. Lovett, N. Nikiforakis 2018 Direct numerical simulations of non-colloidal suspensions in viscoplastic fluids. *British Society of Rheology Non-Newtonian Club Meeting, Cambridge, U.K.*
- **A.R. Koblitz**, S. Lovett, N. Nikiforakis 2018 Direct numerical simulations of particle suspensions in Bingham fluids. *Non-Newtonian Fluid Mechanics Special Interest Group Meeting, Cambridge, U.K.*

as well as at Schlumberger internal meetings in Cambridge, U.K. (September 2015, May 2016, July 2017).

2 Fluid structure interaction

Flows of finite-sized particles in viscous fluids are common to many industrial as well as natural processes, such as primary cementing in the oil and gas industry (Nelson & Guillot, 2006) and blood flow (Bagchi, 2007). Being so ubiquitous, particulate-flow problems span a large range of material and flow properties. Of interest to this work are laminar flows of an incompressible generalised Newtonian fluid at finite Reynolds numbers, where the Reynolds number describes the relative strength of inertial to viscous forces, laden with rigid, spherical (circular) particles.

Direct numerical simulation[1] methods designed for such flow regimes broadly fit into two categories: those methods that use a static grid that is unaligned with the particle boundaries, and those that use boundary-conforming grids. Below we give a brief overview of these two classes of methods and their application to particulate flow problems.

2.1 Body conformal methods

Arbitrary Lagrangian Eulerian (ALE) methods were developed for deforming boundary problems as a response to the difficulties encountered when using fully Lagrangian schemes in problems with large amounts of circulation, see for example, Behr & Tezduyar (1994). The ALE method belongs to the class of

[1] The definition of what constitutes a direct numerical simulation is taken to be that of a simulation within a finite Reynolds number regime where no sub-grid closure models, such as turbulence or wall models, are used and the governing equations can be directly solved such that all continuum time- and length-scales can be resolved through grid refinement alone.

boundary conformal methods, to which the boundary integral method (only applicable to inviscid, irrotational flow) and the overset grid method belong. The semi-discrete, viz. finite element in space and finite difference in time, method of Hughes *et al.* (1981) has proved popular with general fluid structure interaction (FSI) problems and has been continually developed over the last few decades. In this ALE approach, nodal velocities explicitly enter the convective terms of the momentum equations allowing the underlying grid to distort with the moving boundary, while an Eulerian description can be used in regions of large circulation. Hu *et al.* (2001) used an ALE method with a combined fluid–solid formulation to simulate pairs of spheres interacting in Newtonian and viscoelastic liquids, and 2D sedimentation simulations of 90 circular particles.

This ALE method can be considered a special case of the deforming spatial domain or stabilised space time (DSD/SST) method developed by Tezduyar *et al.* (1992), where a finite element formulation is used both in space and time. By extending the finite element formulation in time any grid deformation is automatically accounted for (Tezduyar *et al.*, 1992). To avoid turning a three dimensional problem into a four dimensional problem courtesy of the time dimension, a discontinuous-in-time space-time finite element formulation of the problem is solved for one space-time 'slab' at a time. Johnson & Tezduyar (2001) used the DSD/SST method to simulate up to 125 spheres in tri-periodic domains.

Both the conventional ALE and DSD/SST methods use unstructured grids to explicitly represent the particle surface. Unstructured grids allow for complex surfaces to be represented but are generally not amenable to fast elliptic solvers, such as geometric multigrid.

The distortion of the underlying grid inevitably causes elements to become increasingly skewed. Highly skewed elements can often cause problems relating to accuracy and stability, requiring a new grid to be computed on to which the solution is then projected. Both the regridding and projection steps are costly procedures and are the main drawbacks of ALE and DSD/SST type methods (Haeri & Shrimpton, 2012). Particulate flow simulations generally encounter large deformations, requiring frequent regridding.

Various approaches have been developed to improve the quality of the deformed mesh. Johnson & Tezduyar (1996), for example, used the equations of linear elasticity to govern the deformation of the grid for their particulate flow simulations. The grid distortion was controlled through a stiffness parameter, effectively weighting distortion towards larger elements. This preserved smaller elements in the surface regions that are important to the accuracy of the overall solution. By promoting less important elements, i.e. those far away from the particle surfaces, to distort more easily, regridding is reduced since the grid quality is, potentially, preserved for longer. However, this comes at the cost of solving an additional partial differential equation for the grid deformation.

2.2 Static grid methods

Due to the complexities and costs of the unstructured regridding associated with boundary-conforming grid methods, the static grid methods have gained favour with many researchers for approaching FSI problems. Static grid methods can be split into two categories based on the treatment of the solid–fluid interface: diffuse interface and sharp interface methods. An efficient class of diffuse interface methods is the immersed boundary (IB) method. The original IB method of Peskin (1972) was developed to study flow patterns around heart valves. The entire computational domain is represented by a Cartesian grid and the interface is represented by a collection of massless Lagrangian points. The velocity of these Lagrangian points is used to compute the stress on the elastic interface through a constitutive relation, such as Hooke's law. This singular force distribution is transmitted from the Lagrangian interface points to the Eulerian fluid through a forcing term in the momentum equation. The information transfer is facilitated by a discrete Dirac delta function, smoothly spreading the force from the Lagrangian to the Eulerian grid. Aside from inherent stability benefits, this approach is attractive because only the right-hand side of the momentum equation is affected, so no changes to the underlying solver are required. Assuming constant density across the entire domain also allows fast Poisson solvers to be used without modification (Kempe & Fröhlich, 2012*b*).

Directly applying Peskin's original IB method to rigid boundary problems is not straightforward because the constitutive relation for the elastic boundary is generally not well behaved in the rigid limit (Mittal & Iccarino, 2005). Uhlmann (2005) used the direct forcing formulation of Mohd-Yusof (1997) whilst retaining the smooth information transfer between Lagrangian and Eulerian grid points. Direct forcing methods use a virtual forcing term determined by the difference between the desired interface velocities and the velocities interpolated from the underlying Eulerian grid. Uhlmann proposed evaluating the forcing term at the Lagrangian interface points before smoothly transferring it to Eulerian grid points in order to reduce spatial oscillations common to direct forcing methods. With this direct forcing IB method, Uhlmann & Doychev (2014) performed sedimentation simulations with $\mathcal{O}(10^4)$ spherical particles in tri-periodic domains.

Kempe & Fröhlich (2012*b*) modified the interpolation and spreading procedure of Uhlmann (2005), greatly improving on the Courant–Friedrichs–Lewy (CFL) time step restriction and the stability for light bodies, achieving particle–fluid density ratios as low as $\rho_r = 0.3$ for spherical particles. With this IB method Vowinckel *et al.* (2014) investigated turbulent channel flow with mobile beds consisting of $\mathcal{O}(10^4)$ spherical particles.

Glowinski *et al.* (2001) developed a distributed Lagrange multiplier/fictitious domain method (DLM/FD) reminiscent of Peskin's IB method using the principle of variational inequality in a finite element context. A combined variational formulation of the fluid-solid coupling was used—similar to that of Hu (1996)—but the rigidity was enforced in the particle subdomains through Lagrange multipliers, thereby allowing the governing equations to be solved on stationary grids. The original DLM/FD method imposed velocity on the particle subdomain. Patankar *et al.* (2000) imposed the deformation-rate tensor instead in order to simplify treatment for irregularly shaped particles, while Wachs (2009) used this formulation in conjunction with a discrete element method to develop an improved collision mechanism for irregularly shaped bodies.

The smoothing intrinsic to diffuse interface methods reduces the solution accuracy in the immediate vicinity of the interface. This can be addressed through increased grid resolution, but at the cost of greatly increased calculation size given the grid uniformity. This problem is particularly severe in high Re flows, where the viscous boundary layer is thin. One popular way to improve accuracy at the interface is through the use of sharp interface methods which generally reconstruct the solution near the interface, thereby enforcing the boundary conditions strongly.

Fadlun *et al.* (2000) developed a hybrid approach that borrowed on the momentum forcing approach of Peskin (1972) but with the goal of enforcing boundary conditions exactly. Fadlun *et al.* (2000) used the direct forcing formulation of Mohd-Yusof (1997), but imposed boundary conditions by directly modifying the coefficients of the linear system rather than explicitly calculating the forcing. This was done in order to avoid solving an implicit system for the forcing, which comes about because of the implicit treatment of the viscous terms in their fractional step time advancement scheme (Fadlun *et al.*, 2000). In effect, this is equivalent to applying momentum forcing inside the fluid domain, leading to problems with moving grids when previously 'solid' grid points are converted to 'fluid' points.

Yang & Balaras (2006) demonstrated that unphysical information carried by a previously solid point into the flow field makes the evaluation of the right-hand side of the momentum equation in the fractional step algorithm problematic. They developed a 'field extension' strategy, whereby the velocity and pressure fields are extended into the solid phase at the end or beginning of each sub-step.

Recently, Yang & Stern (2015) improved on this field extension strategy through the introduction of temporary non-inertial reference frames attached to the solid phases. This is based on the fluid–solid coupling strategy of Kim & Choi (2006) and allows the velocity coupling to be done in a non-iterative fashion. Crucially, Yang & Stern (2015) only use the non-inertial reference frame for the forcing, solving the flow field on the inertial reference frame and thereby allowing for an arbitrary number of solid phases. By allowing non-iterative methods to be used for the forcing and rigid-body motion calculations, Yang & Stern (2015) improved the performance by up to an order of magnitude. However, such field extension strategies reduce the sharpness of the immersed boundary, diminishing the advantage over diffuse methods (Seo & Mittal, 2011).

All of the flow reconstruction based sharp interface methods suffer from force oscillations in moving boundary problems (Luo *et al.*, 2012). This is caused by the instantaneous role reversal of a grid point from an interpolation to a discrete Navier–Stokes point, and vice versa, when crossed by the boundary. This role reversal involves an immediate change in computational stencil, causing a temporal discontinuity (Luo *et al.*, 2012). Even the field extension of Yang & Balaras (2006) does not address this (Luo *et al.*, 2012).

An interesting semi-analytical approach is that of Tagaki *et al.* (2003), where an analytical Stokes solution is combined with a numerical Navier–Stokes solution to provide an efficient solution methodology to inertial particulate flow simulations. Tagaki *et al.* (2003) argue by continuity that the no-slip boundary condition results in a region adjacent to the particle surface where the inertial terms of the Navier–Stokes equations are small enough that, locally, the velocity and pressure satisfy the Stokes equations. By defining two sets of points surrounding the particle surface, an inner and outer set, the outer velocities of the Navier–Stokes solution can be used as boundary conditions to calculate the analytical Stokes solution on the inner set. In practice this is done by computing the coefficients of the stream function solution to the Stokes flow to match the velocities of the Navier–Stokes solution on the outer points in an iterative process. These coefficients are then used to calculate the analytical Stokes solution on the inner set of points. Zhang & Prosperetti (2003) successfully extended this semi-analytical approach to arbitrarily moving cylinders; however, it is yet to be applied to three-dimensional problems.

Much recent effort has been focused on static grid methods for particulate flow, owing to the high efficiency of such methods and the desire to simulate engineering flows containing huge numbers of particles. Broadly speaking, boundary conformal methods can offer superior accuracy near the solid/fluid interface but may be inefficient for problems with large spatial deformations due to the costs associated with re-meshing at each time step. On the other hand, static grid methods, which can be highly efficient, have difficulty resolving the boundary layers near particles and may require very fine grids or adaptive mesh refinement to obtain accurate results (Wachs *et al.*, 2015).

In chapter chapter 5 we will evaluate the overset grid, or Chimera grid, method for viscous particulate flow. Overset grid methods have been widely used for problems with moving geometries. They were recognised early on to be a useful technique for treating rigid moving bodies, such as aircraft store separation (Dougherty & Kuan, 1989), and have subsequently been applied to many other moving-grid aerodynamic applications, see for example Meakin (1993); Henshaw & Schwendeman (2006); Zahle *et al.* (2007); Chan (2009); Chandar & Damodaran (2010); Lani *et al.* (2012). The basic approach of moving overset grids used in this dissertation was developed for high-speed compressible and reactive flows by Henshaw & Schwendeman (2006) and included the support for adaptive mesh refinement. The deforming composite grid (DCG) approach was developed in Banks *et al.* (2012) for treating deforming bodies with overset grids, and a partitioned scheme was developed for light deforming bodies that was stable without sub-iterations. A method to overcome the added-mass instability with compressible flows and rigid bodies was developed in Banks *et al.* (2013). More recently, stable partitioned schemes for incompressible flows and deforming solids have been developed (Banks *et al.*, 2014*a*,*b*; Li *et al.*, 2016) and extended to non-linear solids (Banks *et al.*, 2016).

The method described in this dissertation retains much of the efficiency of static structured grid methods whilst still allowing for sharp representation of solid boundaries. The overset grid method can be seen as a bridge between the static and boundary conformal grid methods described previously; the curvilinear particle grids allow for higher than first-order accuracy and boundary conditions to be implemented strongly, while grid connectivity with the static Cartesian background grid is only locally updated. Since the grid connectivity is only updated locally, the regridding procedure is less costly and complex than for unstructured body conformal methods, such as ALE. Local grid refinement allows boundary layers to be fully resolved without appreciably affecting the total grid point count. This is in contrast with general static grid methods where the solver efficiency is offset by the unfavourable scaling associated with uniform grids, making large fully resolved simulations very costly (Wachs *et al.*, 2015). For these reasons, we evaluate the suitability of the method for fully resolved simulations of incompressible fluid flow with rigid particles.

3 Viscoplastic modelling

The system of interest to this work consists of non-colloidal, inert particles transported by an oilfield cement slurry. The cement slurry is itself a highly concentrated suspension of solid particles in water, usually consisting of tricalcium silicate, dicalcium silicate, tricalcium aluminate and tetracalcium alumino-ferrite mineral components (Banfill, 2006), all of which react with water. Though we are principally concerned with flows in small physical domains of order $\mathcal{O}(10\,\mathrm{cm})$, the disparate lengthscales of the inert particles ($\mathcal{O}(500\,\mu\mathrm{m})$) and cement particles ($\mathcal{O}(50\,\mu\mathrm{m})$) allows for a continuum treatment of the cement slurry. The state of this fluid evolves with the familiar continuum conservation laws of mass and momentum but with a different treatment of the constitutive relationship between stress and strain that gives the fluid its non-Newtonian character. In this work, we consider simple (time independent) yield stress fluids in viscously dominated flow regimes.

This chapter will begin by examining some of the basic fluid mechanics describing important characteristics of the slurry, before putting the current work into context by examining numerical methods used to approach such problems, and previous work in the literature.

3.1 Yield stress fluids

We begin with a discussion on viscosity and the definition of a Newtonian fluid before considering the non-Newtonian yield stress fluids of interest. In a fluid at rest the stress tensor, $\boldsymbol{\sigma}$, is comprised solely of the hydrostatic pressure, p, such that

$$\boldsymbol{\sigma} = -p\boldsymbol{I}, \tag{3.1}$$

where $\boldsymbol{I}$ is the identity tensor. For a fluid in motion the stress tensor takes the form of $\boldsymbol{\sigma} = -p\boldsymbol{I} + \boldsymbol{\tau}$, where p is a scalar mechanical pressure (not the same as the thermodynamic pressure) and $\boldsymbol{\tau}$ a traceless deviatoric stress tensor, existing solely due to the fluid motion (Batchelor, 1967).

The deviatoric stress tensor represents a transport of momentum and is assumed to only depend on the instantaneous local fluid velocity distribution, $\nabla\boldsymbol{u}$. To derive a constitutive relationship between $\boldsymbol{\tau}$ and $\nabla\boldsymbol{u}$ we make the approximation that $\boldsymbol{\tau}$ is a linear combination of the various velocity gradient components, provided that these have sufficiently small magnitudes. Thus, the deviatoric stress tensor is linked to the velocity distribution by a tensor coefficient that depends directly on the local state of the fluid but not the velocity distribution as a whole (Batchelor, 1967):

$$\tau_{ij} = A_{ijkl}\frac{\partial u_k}{\partial x_l}. \tag{3.2}$$

Here, the tensor coefficient is necessarily symmetrical in i, j (since $\boldsymbol{\tau}$ is) and, under the assumption that the fluid is *isotropic* it is symmetrical in k, l too. This allows (3.2) to be reduced to

$$\boldsymbol{\tau} = \mu\dot{\boldsymbol{\gamma}} + \lambda(\nabla \cdot \boldsymbol{u}), \tag{3.3}$$

where μ is the scalar viscosity coefficient, λ the second coefficient of viscosity and $\dot{\boldsymbol{\gamma}}$ is the rate-of-strain tensor $\nabla\boldsymbol{u} + \nabla\boldsymbol{u}^T$.

Finally, for an incompressible fluid the conservation of mass reduced to $\nabla\cdot\boldsymbol{u} = 0$, and so the constitutive equation for a Newtonian incompressible fluid becomes

$$\boldsymbol{\tau} = \mu\dot{\boldsymbol{\gamma}}. \tag{3.4}$$

A non-Newtonian fluid exhibits behaviour departing from the above linear model, e.g. a non-linear $\tau(\dot{\gamma})$ flow curve or one that does not pass through the origin. In this work we are concerned with simple (time independent) yield stress fluids.

A yield stress fluid is not a true fluid in the sense that it does not flow under an imposed stress unless it exceeds a threshold value (Bonn *et al.*, 2017). Such fluids behave as solids until their yield stress is exceeded, after which they flow under a state transformation that is reversible in the absence of chemical reactions (Coussot, 2014).

There has been much controversy surrounding the existence of a true yield stress, that is to say a critical separation point between a true solid and fluid state. This was fuelled when improvements in measurement device capabilities allowed experimentalists to measure stain rates of $\mathcal{O}(10^{-9})\,\mathrm{s}^{-1}$, finding so-called transitions to Newtonian flow curves well below the supposed yield stress (Barnes & Walters, 1985). The implication is that the yield stress marks a temporary transition between two Newtonian fluids with radically different viscosities, rather than fluid/solid regimes (Barnes & Walters, 1985; Barnes, 1999). However, Møller *et al.* (2009) demonstrated that these low stress Newtonian viscosities are in fact artefacts arising in non-steady state experiments and the consensus seems to be that in experimental time scales a true yield stress model is appropriate.

The simple Bingham viscoplastic fluid model is used in this work. Here, the flow curve is linear after the imposed stress exceeds the material yield stress. As is common in the literature, dimensionless numbers are maintained in the same form as the Newtonian ones, where the viscosity is replaced by the plastic viscosity parameter of the Bingham model (Thompson & Soares, 2016). The exception being the Bingham number:

$$\mathrm{Bn} = \frac{\tau_y \mathcal{L}}{\eta \mathcal{U}}, \tag{3.5}$$

where L and U are appropriate length and velocity scales, τ_y is the material yield stress, and η is the scalar plastic viscosity coefficient. This is the only dimensionless number used that characterises the fluid plasticity. Recently, a characteristic stress definition, effectively including the yield stress in all viscous effect related dimensionless number, has been proposed by Thompson & Soares (2016). This will be helpful in problems where appropriate velocity scales are not readily

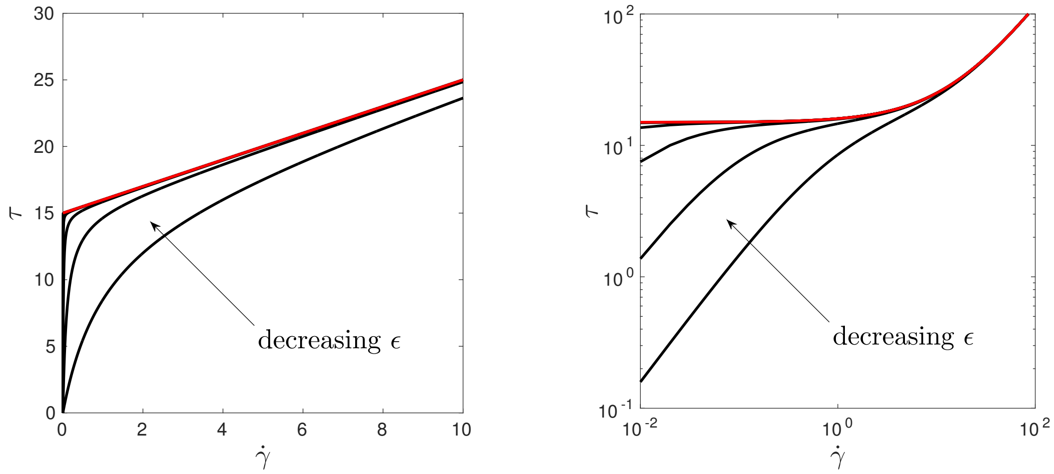

FIGURE 3.1: Flow curves on linear (left) and log (right) scales for the ideal (—) and regularised Bingham model (—), demonstrating the improved approximation with decreasing regularisation parameter, ϵ.

apparent but characteristic stresses may be, such as shear induced particle sedimentation.

Other rheological models exist which demonstrate non-linear $\tau(\dot{\gamma})$ flow curves, for example, the shear-thinning Herschel-Bulkley model which has been used as a continuum model for cement. The framework used here is sufficiently general to allow for more exotic models than the Bingham model.

For a Bingham plastic, we have a discontinuous constitutive relationship where for an imposed stress below the yield stress the material is a rigid solid, such that

$$\dot{\boldsymbol{\gamma}} = 0, \text{ if } ||\boldsymbol{\tau}|| \leq \tau_y \tag{3.6}$$

while after the yield stress is exceeded

$$\boldsymbol{\tau} = \left(\eta + \frac{\tau_y}{||\dot{\boldsymbol{\gamma}}||}\right)\dot{\boldsymbol{\gamma}}, \text{ if } ||\boldsymbol{\tau}|| > \tau_y \tag{3.7}$$

where η is the plastic viscosity, and τ_y the yield stress. The discontinuous nature of this apparently simple model is challenging as it requires the application of two different constitutive laws across a priori unknown yield surfaces (Papanastasiou, 1987).

Empirically, Herschel-Bulkley fits are found for a wide variety of systems within the exponent range $n = 0.2$–0.8 (Bonn *et al.*, 2017). Numerically, the extension of the solvers presented in the following section to the Herschel-Bulkley model is trivial:

$$\boldsymbol{\tau} = \left(K||\dot{\boldsymbol{\gamma}}||^{n-1} + \frac{\tau_y}{||\dot{\boldsymbol{\gamma}}||} \right) \dot{\boldsymbol{\gamma}}, \text{ if } ||\boldsymbol{\tau}|| > \tau_y \tag{3.8}$$

where K is the consistency index, n the flow index, and $n = 1$ returns the simple Bingham model. However, we continue to use the Bingham model because the experiments presented in the following chapters are purely computational, and thus there is analogue material to tune Herschel-Bulkley model to.

Bingham type models are not applicable to all yield stress materials. In the excellent review article of Bonn *et al.* (2017) three classes are described: soft glassy materials; jammed materials; colloidal gels. Bingham type models may fair well for some jammed materials, e.g. emulsions, but typically fail for materials exhibiting more exotic behaviour, particularly time or temperature dependence.

3.2 Regularisation

A common approach to circumventing the challenges posed by this discontinuous constitutive relationship is to regularise it such that the flow curve is forced through the origin, thereby transforming the problem into a purely viscous one.

Bercovier & Engelman (1980) regularised the constitutive law by perturbing the rate-of-strain magnitude in (3.7) by some small constant ϵ such that $||\dot{\boldsymbol{\gamma}}||_\epsilon = \sqrt{||\dot{\boldsymbol{\gamma}}||^2 + \epsilon^2}$, thereby approximating the unyielded solid regions by a high viscosity fluid.

$$\boldsymbol{\tau} = \left(\eta + \frac{\tau_y}{||\dot{\boldsymbol{\gamma}}||_\epsilon} \right) \dot{\boldsymbol{\gamma}}. \tag{3.9}$$

Lipscomb & Denn (1984) and Gartling & Phan-Thien (1984) developed a bi-viscosity model that treats the unyielded zones as high viscosity fluids:

$$\tau = \begin{cases} \frac{\eta}{\epsilon}\dot{\gamma}, & \text{if } ||\dot{\gamma}|| < \epsilon\tau_y/\eta, \\ \left(\eta + \frac{(1-\epsilon)\tau_y}{||\dot{\gamma}||}\right)\dot{\gamma}, & \text{if } ||\dot{\gamma}|| \geq \epsilon\tau_y/\eta. \end{cases} \tag{3.10}$$

Papanastasiou (1987) regularised the constitutive law by introducing an exponential stress growth governed by an exponent with units time

$$\tau = \left(\eta + \frac{\tau_y}{||\dot{\gamma}||}\left(1 - \exp\left(-\frac{\dot{\gamma}}{\epsilon}\right)\right)\right)\dot{\gamma}, \tag{3.11}$$

which holds uniformly in both yielded and unyielded regions, since

$$\lim_{||\dot{\gamma}||\to 0} \tau = \left(\eta + \tau_y/\epsilon\right)\dot{\gamma}. \tag{3.12}$$

Regularisation methods should all approach the ideal Bingham model as $\epsilon \to 0$, however, in practice this is not attainable as the solution procedure involves the inversion of a matrix system with coefficients scaling as τ_y/ϵ, making the system progressively ill-conditioned. These numerical realities have the consequence that with any regularisation method there exists a balance between accuracy and stability.

Frigaard & Nouar (2005) performed detailed convergence studies on regularisation methods, determining flow dependent convergence properties. Regularisation methods were all found to perform best for flows in which the deviatoric stress exceeds the yield stress globally—flows for which the ideal Bingham model may be applied without regularisation in the first place. The largest errors were found to occur in flows where large regions of the flow field exhibit deviatoric stresses close to the yield stress, making yield surface determination difficult. It was also shown that regularisation methods are not appropriate for hydrodynamic stability problems, predicting instability where the ideal Bingham model does not.

3.3 Augmented Lagrangian Methods

A second class of methods is the so-called Augmented Lagrangian Method developed by Lions and Glowinski between 1973 and 1984 but only finding widespread use fairly recently. This class of methods is based on variational inequalities, first derived for creeping flow by Prager (1952) and for fully inertial flows by Huilgol (2002). These variational inequalities correspond to a functional that is minimised by the solution to the initial boundary value problem. A common strategy is to frame the variational inequality as a constrained minimisation problem whereby a Lagrangian multiplier and quadrature penalisation are used to relax the velocity gradient computation.

This class of methods has been shown to be robust and can be used without regularisation, allowing for truly unyielded zones with zero strain rates and accurate detection of yield surfaces. However, they are more complex to implement than primitive variable regularisation methods and many ALM approaches are hampered by slow convergence rates. This is the method used to compute viscoplastic flows in this work, notwithstanding slow convergence rates, and will be discussed in detail in section 4.5.

3.4 Previous work

In this section we describe applications in the literature of the aforementioned methods for particulate flow problems.

Blackerly & Mitsoulis (1997) investigated the creeping flow of a Bingham plastic fluid past a sphere in a tube using Papanastasiou regularisation, confirming an increase in drag coefficient with an increase in Bingham number over a range of $0 \leq \mathrm{Bn} \leq 1000$. Though limited to coarse computational meshes by the computing power available at the time, yield surfaces were determined for the unyielded envelope surrounding the cylinder and its growth with decreasing plasticity was demonstrated.

Tokpavi *et al.* (2008) investigated the creeping viscoplastic flow of a cylinder travelling rectilinearly between parallel plates using Papanastasiou regularisation with the commercial Polyflow (Fluent inc) package, extending the drag coefficient results of Mitsoulis (2004) to $\mathrm{Bn} = 2 \times 10^5$. Results were presented for flow field kinematics, including stress and strain profiles along axes of symmetry. A viscoplastic boundary layer was identified and velocity profiles across the layer were compared against theoretical predictions of Piau (2002) and Piau & Debiane (2004), with discrepancies at large Bn considered to be largely due to numerical errors.

Nirmalkar *et al.* (2012) investigated creeping flow past a square cylinder using Papanastasiou regularisation, presenting drag coefficients for Bingham number ranges spanning five orders of magnitude. Similar to Tokpavi *et al.* (2008), Nirmalkar examined the extent of viscoplastic boundary layers and provided approximate expressions for the non-dimensional boundary layer thickness as a function of Bn, albeit with significant errors (averaging 15 %) at Bn below 1000.

The dependence of maximum shear rate on not only the stress growth parameter—as is expected—but also the mesh quality was demonstrated, highlighting the difficulty in selecting appropriate model parameters to ensure confidence in the numerical results.

Mossaz *et al.* (2010) used Papanastasiou regularisation with the commercial Fluent package to investigate inertial viscoplastic flow past an unconfined circular cylinder using the Herschel-Bulkley model, which is equivalent to the Bingham model in the limiting case. Increasing plasticity of the fluid was found to have a stabilising effect, decreasing the shedding frequency of vortices past the cylinder for a fixed Reynolds number (based on the plastic viscosity η). The Papanastasiou regularisation was found to present unphysical aberrations in limiting cases, such as the onset of recirculation behind the cylinder caused by low strain rates in nominally unyielded regions.

Liu *et al.* (2003) simulated two infinite cylinders translating colinearly in a Bingham plastic fluid, investigating the influence of separation distance on the drag coefficient. It was demonstrated that the range of interaction in a yield stress fluid is markedly smaller than in a Newtonian fluid, with a drag reduction of

30 % found between the extrema configurations. For two approaching cylinders Liu *et al.* (2003) noted a decrease in drag with decreased separation distance—the opposite of what is found in a Newtonian fluid. Liu *et al.* (2003) attributed this drag reduction to the shear thinning property of the Bingham fluid, which would lower the viscosity in the vicinity of the cylinders as they approach. In chapter chapter 7 we will find that localised shear thinning leads to an increased settling efficiency with solid volume fraction in particle suspensions in viscoplastic media.

Yu & Wachs (2007) performed sedimentation simulations of one and two spheres in a viscoplastic fluid using an augmented Lagrangian method. Yu & Wachs (2007) investigated the drag reduction by approaching cylinders noted by Liu *et al.* (2003), though at significantly lower Bingham number ranges. The drag reduction with reduced separation distance was reproduced, however, at separation distances lower than those investigated by Liu *et al.* (2003) a drag increase was found. Yu & Wachs (2007) concluded that the plastic force is indeed shear-thinning and dominates the drag force until the spheres approach a critical distance past which the lubrication force dominates. In chapter chapter 6 we investigate the squeeze flow between two approaching circular cylinders, fi nding that the lubrication force scales with the Bingham number.

Prashant (2011) performed simulations of two particles sedimenting in a Bingham plastic fluid using dual viscosity regularisation and a Lattice Boltzmann method. Plasticity effects were weak ($\mathrm{Bn} < 1$) but, nevertheless, at low Reynolds numbers approaching spheres were prevented from touching each other by the formation of an unyielded zone connecting the spheres at low separation distances, raising interesting questions regarding particle aggregation in yield stress fluid suspensions. In chapter chapter 7 we find bridged clusters in particle suspensions in viscoplastic media, leading to increased mobility at high yield stresses.

Meaningful experimental studies of complex viscoplastic fluid flow have only recently become available with improvements in flow field measurement techniques. Carbopol-940 is broadly considered an ‘ideal’ viscoplastic fluid and as such is the most commonly used. Quantitative comparison, even with Carpobol, with theoretical or numerical results is difficult, with wall slip and possible normal stress effects (usually associated with elastic or thixotropic material) posing particular challenges.

The first experimental study providing quantitative information on the flow field kinematics is that of Atapattu *et al.* (1995), where a laser-speckle tracer method was employed. Yield surface locations were inferred from the velocity field, allowing yield envelopes qualitatively similar to those of Beris *et al.* (1985) to be determined. The plasticity effects were fairly weak, with $1.87 \leq \mathrm{Bn} \leq 3.28$ and no asymmetry in the flow field was reported, in-line with numerical studies.

Merkak *et al.* (2006) investigated the interaction of spherical particle pairs in high yield stress Carbopol-940 solutions at low Reynolds number. Both coaxial and side-by-side configurations were considered and results for the drag coefficient in the former case agreed to within 10 % of those of Liu *et al.* (2003). The interaction range was found to be significantly shorter than for the Newtonian equivalent, again similar to Liu *et al.* (2003). The side-by-side configuration resulted in a lower drag coefficient for any separation distance presumed to be the result of flow between the spheres preventing the formation of a connecting rigid zones. No quantitative measurements were taken of the flow field kinematics.

Putz *et al.* (2008) used particle image velocimetry (PIV) to study the viscoplastic flow around a sphere. Once again, Carbopol-940 was used as the yield stress fluid. Most strikingly, strong fore-aft asymmetries were found in the viscoplastic experiments. Inertial influence was discounted since equivalent Newtonian tests showed no such asymmetries in the flow field. Putz *et al.* (2008) determined that the asymmetry was due to elastic properties of the Carbopol-940 solution. Having demonstrated a hysteresis region near the yield stress Putz *et al.* (2008) agreed with Harlen (2002), who investigated the negative wake behind a sedimenting sphere in a viscoelastic fluid, that relaxation of shear stresses in the wake promote the asymmetry.

Tokpavi *et al.* (2009) investigated the sedimentation of a cylinder in Carbopol-940 with higher plasticity effects ($20 \leq \mathrm{Bn} \leq 32$). The authors were able to conclude that elastic relaxation was unlikely to cause the asymmetrical flow field, agreeing instead with Joseph & Feng (1995) that normal stresses in the fluid could instead be the cause.

While there exists a consensus amongst experimentalists that viscoelastic effects are the likely cause for fore-aft asymmetry, the mechanics remain unclear. However, it is becoming clear that current continuum models do not adequately describe the materials for which there exist experimental data. We emphasise that although a simple model (Bingham plastic) is considered in this report, the computational framework is sufficiently general to encompass more complex models as required.

3.5 Conclusions

Much of the work on viscoplastic particulate flows has been limited to studies of fewer than five particles, in both two and three dimensions, with and without inertia, and using both regularised and exact solution methods. While interesting flow behaviours have been identified at this scale, e.g. localised shear thinning leading to a drag reduction for nearby particles; the stabilising effect of the plasticity on unsteady wakes; unyielded material forming connecting 'bridges' between nearby particles, such effects on larger particle systems has yet to be explored.

In this work, we aim to make inroads into the regime of particle suspensions in non-inertial viscoplastic fluids by reducing the complexity of the model and using state-of-the-art computational approaches. In the following chapter, we give an overview of the numerical methods used in this work.

4 Numerical methods

This chapter provides an overview of the overset grid discretisation scheme, the spatial discretisation using overset grids, and the Newtonian and non-Newtonian flow solvers used in this work. We make use of the open source Overture library, an object oriented toolkit for solving partial differential equations on overset grids (Brown *et al.*, 1999). We begin with an overview of the overset grid method as is applicable to fluid structure interaction.

4.1 Overset grids

The method of overset grids (also called overlapping, overlaid or chimera[1] grids) bridges the stationary and boundary conformal grid methods. A complex domain is represented by multiple body-fitted curvilinear grids that are allowed to overlap, as shown in Fig. 4.1. Overset grids bring flexibility to grid generation since component grids are not required to align along block boundaries. This flexibility allows component grids to be added in a relatively independent manner, requiring only local changes to grid connectivity.

A composite grid $\mathcal{G}$ consists of logically rectangular component grids $\mathcal{G}_k$, with $k = 1, 2, \ldots N_g$. As illustrated in Fig. 4.1 the grid points of $\mathcal{G}$ are classified as interior points, boundary points, interpolation points and exterior or unused points. The algorithm for generating a composite grid from a collection of component grids is intricate; a detailed description is beyond the remit of this work and so it will be only briefly discussed, with the intention of showing why the

[1] In reference to disparate component grids coming together to form a complex body.

method of overset grids is appropriate for particulate flow problems. The interested reader is referred to Chesshire & Henshaw (1990) and Henshaw (1998) for a full description of the algorithm and implementation.

A composite grid $\mathcal{G}$ consists of logically rectangular component grids $\mathcal{G}_k$, with $k = 1, 2, \dots N_g$. All the grid points of $\mathcal{G}$ must be classified as one of the following:

1. *Interior point*. An interior point can be discretised in terms of points on its component grid $\mathcal{G}_k$ alone.
2. *Boundary point*. A boundary point lies on a physical boundary of $\mathcal{G}$ and can be discretised in terms of points on $\mathcal{G}_k$ alone.
3. *Interpolation point*. An interpolation point can be interpolated from interior, boundary or interpolation points from component grids $\mathcal{G}_{k' \neq k}$
4. *Exterior point*. An exterior point is neither an interior, boundary, or an interpolation point. It lies outside the computational domain and is therefore unused, reducing the computational cost.

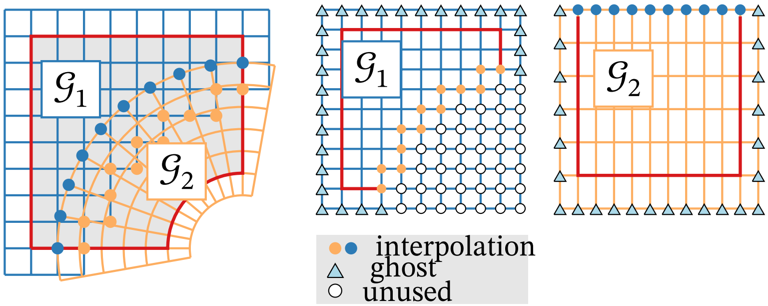

FIGURE 4.1: Left: an overlapping grid consisting of two structured curvilinear component grids, $\boldsymbol{x} = \mathcal{G}_1(\boldsymbol{r})$ and $\boldsymbol{x} = \mathcal{G}_2(\boldsymbol{r})$. Middle and right: component grids for the square and annular grids in the unit square parameter space $\boldsymbol{r}$. Grid points are classified as discretisation points, interpolation points or unused points. Ghost points are used to apply boundary conditions. The physical boundary is represented by the solid red line.

Interior and boundary points can be collectively referred to as discretisation points. Finally, discretisation and interpolation points are not mutually exclusive. To facilitate the construction of a valid composite grid, component grids are labelled $k = 1, 2, \dots, N_g$ in order of ascending priority, with the idea being that higher priority grids are overlayed on top of lower priority grids. The simplified grid generation algorithm reads as follows:

Step 1 Initially, all component grid points are initialised as discretisation points.

Step 2 Non-boundary points of grid k (i.e. interior points at this stage) that lie close to physical boundary points of k', with $k \neq k'$, are marked as exterior points as they lie outside the computational domain.

Step 3 Starting from the highest numbered grid to the lowest each grid point is examined to find the highest component grid it can be interpolated from.

Step 4 Step 3 results in more interpolation points than are strictly necessary, which increases the storage overhead. Working from the lowest grid upwards, interpolation points that are definitely needed by higher grids are marked.

Step 5 Finally, unnecessary interpolation points are marked as exterior points and the composite grid can be generated.

When moving grids are used, as is the case in particulate flow problems where each particle is represented by a separate component grid, the relative position of overset grids changes continuously. As a result, overlapping connectivity information, i.e. Chimera holes (regions of exterior points in the overset component grids) and interpolation points, must be recomputed at every time-step. Crucially, this is cheaper than complete grid regeneration and the required connectivity information recomputation can be locally confined to those grids affected by the moving grid.

Values of the solution at interpolation points are determined by standard tensor-product Lagrange-interpolation. We use quadratic interpolation (three-point stencil in each direction) for the results in this work, as required for second-order accuracy (Chesshire & Henshaw, 1990). This interpolation is not locally conservative. Locally conservative interpolation on overset grids is possible (Chesshire & Henshaw, 1994) but has not been found necessary in our experience (Henshaw, 2017). Corrections to ensure global conservation are also possible and have been shown to have advantages, see for example (Tang *et al.*, 2003).

4.2 Spatial discretisation

The equations of motion are discretised to second-order accuracy in space using finite difference methods on overset grids, see Henshaw (1994) and Henshaw & Petersson (2003). An overset grid consists of logically rectangular grids that cover a grid region and overlap where they coincide. The solutions between adjacent grids are connected via interpolation conditions. Each component grid (numbered $k = 1, 2, \dots, N_g$) is associated with a transformation $\boldsymbol{d}_k : \mathbb{R}^3 \to \mathbb{R}^3$ from the unit square, with coordinates denoted by $\boldsymbol{r} = (r_1, r_2, r_3)$, into physical space, $\boldsymbol{x} = (x_1, x_2, x_3)$, and denoted by $\boldsymbol{d}_k(\boldsymbol{r}, t) = \boldsymbol{x}(\boldsymbol{r}, t)$, which allows for body fitted grids of non-rectangular shapes. Consider solving the equations in three space dimensions on a square component grid $\mathcal{G}_k$, with grid spacing $h_m = 1/N_m$, for a positive integer N_m:

$$\mathcal{G}_k = \{\boldsymbol{x}_{\boldsymbol{i},k} \mid \boldsymbol{i} = (i_1, i_2, i_3),\ N_{m,a,k} - 1 \le i_m \le N_{m,b,k} + 1,\ m = 1, 2, 3\},$$

where $\boldsymbol{i} = (i_1, i_2, i_3)$ is a multi-index and a and b denote the beginning and end grid line numbers, respectively. Ghost points are included at the boundaries, $i_m = N_{m,a,k}$ or $i_m = N_{m,b,k}$, to facilitate discretising to second order. The component grid number k will be dropped in the following discussion.

Derivatives with respect to $\boldsymbol{r}$ are standard second-order centred finite difference approximations, for example,

$$\begin{aligned}
\frac{\partial \boldsymbol{u}}{\partial r_m} &\approx D_{r_m} \boldsymbol{U}_{\boldsymbol{i}} := \frac{\boldsymbol{U}_{\boldsymbol{i}+\boldsymbol{e}_m} - \boldsymbol{U}_{\boldsymbol{i}-\boldsymbol{e}_m}}{2h_m}, \\
\frac{\partial^2 \boldsymbol{u}}{\partial r_m^2} &\approx D_{r_m r_m} \boldsymbol{U}_{\boldsymbol{i}} := \frac{\boldsymbol{U}_{\boldsymbol{i}+\boldsymbol{e}_m} - 2\boldsymbol{U}_{\boldsymbol{i}} + \boldsymbol{U}_{\boldsymbol{i}-\boldsymbol{e}_m}}{h_m^2},
\end{aligned}$$

where $\boldsymbol{e}_m$ is the unit vector in the m-th coordinate direction and $\boldsymbol{U}_{\boldsymbol{i}}$ is the numerical approximation of $\boldsymbol{u}$. Using the chain rule the derivatives with respect to $\boldsymbol{x}$ are defined as

$$
\begin{aligned}
\frac{\partial \boldsymbol{u}}{\partial x_m} &= \sum_n \frac{\partial r_n}{\partial x_m}\frac{\partial \boldsymbol{u}}{\partial r_n} \approx D_{x_m}\boldsymbol{U_i} := \sum_n \frac{\partial r_n}{\partial x_m} D_{r_n}\boldsymbol{U_i},\\
\frac{\partial^2 \boldsymbol{u}}{\partial x_m^2} &= \sum_{n,l} \frac{\partial r_n}{\partial x_m}\frac{\partial r_l}{\partial x_m}\frac{\partial^2 \boldsymbol{u}}{\partial r_n \partial r_l} + \sum \frac{\partial^2 r_n}{\partial x_m^2}\frac{\partial \boldsymbol{u}}{\partial r_n}\\
&\approx D_{x_m}D_{x_m}\boldsymbol{U_i} := \sum_{n,l} \frac{\partial r_n}{\partial x_m}\frac{\partial r_l}{\partial x_m} D_{r_m r_l}\boldsymbol{U_i} + \sum_n \left(D_{x_m}\frac{\partial r_n}{\partial x_m}\right) D_{r_n}\boldsymbol{U_i},
\end{aligned}
$$

where the entries in the Jacobian matrix, $\partial r_m / \partial x_n$ are obtained from the mapping $\boldsymbol{x} = \boldsymbol{d}_k(\boldsymbol{r}, t)$.

4.3 Newtonian flow solver

In chapter chapter 5 we make use of the CGINS (version 24) incompressible flow solver built upon the Overture framework Henshaw (2010). Incompressible flow is governed by the Navier–Stokes equations,

$$
\begin{aligned}
\frac{\partial \boldsymbol{u}}{\partial t} + (\boldsymbol{u} \cdot \nabla)\boldsymbol{u} &= -\frac{1}{\rho}\nabla p + \nu \nabla^2 \boldsymbol{u} + \boldsymbol{f},\\
\nabla \cdot \boldsymbol{u} &= 0,
\end{aligned}
$$

where $\boldsymbol{u}$ is the vector of Cartesian components of the velocity u_i, p the pressure field, ρ the fluid density, and $\nu = \mu/\rho$ the kinematic viscosity. For discretising the equations on a moving grid (on an overset grid some grids are static while others are attached to, and move with the body), we make a change of dependent variables $\boldsymbol{x}$ and t to a frame that moves with the grid. As a result, on moving domains, the governing equations transform to

$$
\frac{\partial \boldsymbol{u}}{\partial t} + ((\boldsymbol{u} - \boldsymbol{w})) \cdot \nabla \boldsymbol{u} = -\frac{1}{\rho}\nabla p + \nu \nabla^2 \boldsymbol{u} + \boldsymbol{f}, \tag{4.1}
$$

$$
\nabla \cdot \boldsymbol{u} = 0, \tag{4.2}
$$

where $\boldsymbol{w}$ is the velocity of a point attached to the moving domain. The partial derivative in time in the moving frame, as appearing in (4.1), is therefore the derivative in time when keeping the spatial location fixed to a point that is attached to the moving domain.

We solve an alternative formulation of system (4.1)-(4.2). A pressure Poisson equation is derived by taking the divergence of the momentum equation (4.1) and using (4.2). The resulting velocity–pressure formulation of the initial-boundary value problem is

$$
\begin{aligned}
\frac{\partial \boldsymbol{u}}{\partial t} + ((\boldsymbol{u}-\boldsymbol{w})\cdot\nabla)\boldsymbol{u} + \frac{1}{\rho}\nabla p - \nu\nabla^2\boldsymbol{u} - \boldsymbol{f} &= 0, && \forall \boldsymbol{x}\in\Omega, && (4.3)\\
\mathcal{J}(\nabla\boldsymbol{u}) + \frac{1}{\rho}\nabla^2 p - \nabla\cdot\boldsymbol{f} &= 0, && \forall \boldsymbol{x}\in\Omega, && (4.4)\\
B(\boldsymbol{u},p) &= \boldsymbol{0}, && \forall \boldsymbol{x}\in\partial\Omega, && (4.5)\\
\nabla\cdot\boldsymbol{u} &= 0, && \forall \boldsymbol{x}\in\partial\Omega, && (4.6)\\
\boldsymbol{u}(\boldsymbol{x},0) &= \boldsymbol{u}_0(\boldsymbol{x}), && \text{at}\quad t=0, && (4.7)
\end{aligned}
$$

where $\mathcal{J}(\nabla\boldsymbol{u}) \equiv \nabla\boldsymbol{u} : \nabla\boldsymbol{u}$ and Ω denotes the fluid domain in n_d space dimensions. There are n_d primary boundary conditions, denoted by $B(\boldsymbol{u},p)=\boldsymbol{0}$. The velocity–pressure formulation requires an additional boundary condition for the pressure. Here, the velocity divergence (4.6) is applied as the boundary condition on the pressure, making the velocity–pressure formulation equivalent to the velocity–divergence formulation (Henshaw, 1994). For the second-order accurate scheme used here, boundary conditions are required to determine $\boldsymbol{u}$ and p at a line of fictitious (ghost) points outside the domain boundary. Some of the numerical boundary conditions are *compatibility conditions*, derived by applying the momentum and pressure equations on the boundary.

The motion of a rigid body immersed in the fluid is governed by the Newton–Euler equations,

$$
\frac{\mathrm{d}\boldsymbol{x}_b}{\mathrm{d}t} = \boldsymbol{v}_b, \quad m_b\frac{\mathrm{d}\boldsymbol{v}_b}{\mathrm{d}t} = \boldsymbol{F}, \quad A\frac{\mathrm{d}\boldsymbol{\omega}}{\mathrm{d}t} = -\boldsymbol{\omega}\times A\boldsymbol{\omega} + \boldsymbol{T}, \quad \frac{\mathrm{d}\boldsymbol{e}_i}{\mathrm{d}t} = \boldsymbol{\omega}\times\boldsymbol{e}_i.
$$

Here $\boldsymbol{x}_b(t)$ and $\boldsymbol{v}_b(t)$ are the position and velocity of the centre of mass, respectively, m_b is the mass of the body, $\boldsymbol{\omega}$ is the angular velocity, A is the moment of inertia matrix, $\boldsymbol{e}_i$ are the principal axes of inertia, $\boldsymbol{F}(t)$ is the applied force, and $\boldsymbol{T}(t)$ is the applied torque about the centre of mass of the body. The principal axes of inertia are integrated over time to find the rotation matrix which is used to update positions, velocities and acceleration of points attached to the body surface.

The force and torque on the body are determined from both body forces, such as gravity, and hydrodynamic forces arising from the stresses exerted by the fluid on the body surface, Γ,

$$\boldsymbol{F} = \int_\Gamma (-p\boldsymbol{n} + \boldsymbol{\tau}\cdot\boldsymbol{n})\,\mathrm{d}s + \boldsymbol{f}_b, \qquad \boldsymbol{T} = \int_\Gamma (\boldsymbol{x} - \boldsymbol{x}_b)\times(-p\boldsymbol{n} + \boldsymbol{\tau}\cdot\boldsymbol{n})\,\mathrm{d}s + \boldsymbol{t}_b,$$

where $\boldsymbol{x}$ is a point on Γ, $\boldsymbol{\tau} = \mu(\nabla\boldsymbol{u} + (\nabla\boldsymbol{u})^T)$ is the viscous stress tensor, $\boldsymbol{n}$ is the unit normal vector to the body surface (outward pointing from the fluid domain), $\boldsymbol{f}_b$ is any external body force and $\boldsymbol{t}_b$ is any external body torque.

Let $\boldsymbol{U}_{\boldsymbol{i}} \approx \boldsymbol{u}(\boldsymbol{x}_{\boldsymbol{i}}, t)$, $\boldsymbol{W}_{\boldsymbol{i}} \approx \boldsymbol{w}(\boldsymbol{x}_{\boldsymbol{i}}, t)$, and $P_{\boldsymbol{i}} \approx p(\boldsymbol{x}_{\boldsymbol{i}}, t)$ be the numerical approximations to $\boldsymbol{u}$, $\boldsymbol{w}$ and p, respectively. The momentum and pressure equations are discretised with second-order finite difference stencils, such that the discretised governing equations are

$$\begin{aligned}\frac{\mathrm{d}}{\mathrm{d}t}\boldsymbol{U}_{\boldsymbol{i}} + ((\boldsymbol{U}_{\boldsymbol{i}} - \boldsymbol{W}_{\boldsymbol{i}})\cdot\nabla_2)\boldsymbol{U}_{\boldsymbol{i}} + \frac{1}{\rho}\nabla_2 P_{\boldsymbol{i}} - \nu\nabla_2^2\boldsymbol{U}_{\boldsymbol{i}} - \boldsymbol{f}_{\boldsymbol{i}} &= 0,\\ \frac{1}{\rho}\nabla_2^2 P_{\boldsymbol{i}} + \mathcal{J}(\nabla_2\boldsymbol{U}_{\boldsymbol{i}}) - \nabla_2\cdot\boldsymbol{f}_{\boldsymbol{i}} &= 0,\end{aligned}$$

where $\nabla_2\boldsymbol{U}_{\boldsymbol{i}} = (D_{x_1}\boldsymbol{U}_{\boldsymbol{i}}, D_{x_2}\boldsymbol{U}_{\boldsymbol{i}}, D_{x_3}\boldsymbol{U}_{\boldsymbol{i}})$, $\nabla_2^2\boldsymbol{U}_{\boldsymbol{i}} = (D_{x_1x_1} + D_{x_2x_2} + D_{x_3x_3})\boldsymbol{U}_{\boldsymbol{i}}$, and $\nabla_2\cdot\boldsymbol{U}_{\boldsymbol{i}} = D_{x_1}\boldsymbol{U}_{1,\boldsymbol{i}} + D_{x_2}\boldsymbol{U}_{2,\boldsymbol{i}} + D_{x_3}\boldsymbol{U}_{3,\boldsymbol{i}}$.

4.3.1 Temporal discretisation

The method of lines is used for solving the equations in time. After discretising the governing equations in space they can be regarded as a system of ODEs,

$$\frac{\mathrm{d}}{\mathrm{d}t}\boldsymbol{U} = \boldsymbol{F}(\boldsymbol{U}, \boldsymbol{t}),$$

where pressure is considered a function of the velocity, $P = P(\boldsymbol{U})$. The equations are integrated in time using either a fully explicit or semi-implicit scheme, depending on the stability restriction imposed by the viscous time-step characteristic to the problem. The explicit scheme uses a second-order accurate Adams-Bashforth predictor followed by a second-order accurate Adams-Moulton corrector. For light rigid bodies, multiple correction steps are used to stabilise the scheme, under-relaxing the computed forces on the bodies. The semi-implicit scheme treats the viscous term of the momentum equation implicitly with a second-order Crank-Nicolson method, which is once again combined with Adams-Moulton corrector steps if under-relaxed sub-iterations are required. To illustrate this we will use the momentum equations as an example. Splitting the equations into explicit and implicit components we have

$$\frac{\mathrm{d}\boldsymbol{u}}{\mathrm{d}t} = -((\boldsymbol{u} - \boldsymbol{w}) \cdot \nabla)\boldsymbol{u} - \frac{1}{\rho}\nabla p \quad + \nu\nabla^2\boldsymbol{u} \quad \equiv \boldsymbol{F}_E + \boldsymbol{F}_I,$$

where $\boldsymbol{F}_E$ and $\boldsymbol{F}_I$ are the explicit and implicit components, respectively

$$\boldsymbol{F}_E = -((\boldsymbol{u} - \boldsymbol{w}) \cdot \nabla)\boldsymbol{u} - \frac{1}{\rho}\nabla p, \quad \boldsymbol{F}_I = \nu\nabla^2\boldsymbol{u}. \tag{4.8}$$

The equations are integrated using either fully explicit or semi-implicit schemes. The explicit integration scheme used in the present work is the second-order in time Adams predictor–corrector method. It consists of an Adams–Bashforth predictor

$$\frac{\boldsymbol{u}^p - \boldsymbol{u}^n}{\Delta t} = \beta_0\boldsymbol{F}^n + \beta_1\boldsymbol{F}^{n-1},$$

with the constants $\beta_0 = 1 + \frac{\Delta t}{2\Delta t_1}$ and $\beta_1 = -\frac{\Delta t}{2\Delta t_1}$ chosen for second-order accuracy even with a variable time-step where $\Delta t_1 = t_n - t_{n-1}$, and an Adams–Moulton corrector

$$\frac{\boldsymbol{u}^{n+1} - \boldsymbol{u}^n}{\Delta t} = \frac{1}{2}\boldsymbol{F}^p + \frac{1}{2}\boldsymbol{F}^n.$$

Though only one corrector step was taken here, one may in practice correct multiple times. In fact, this is necessary when dealing with moving, light rigid bodies and partitioned fluid–solid coupling, as will be discussed later.

A semi-implicit approach is taken in some diffusion dominated problems where the explicit diffusive time-step is overly restrictive. Generally, this is the case when the Reynolds number is very low or the grid is highly refined near solid boundaries. Here, the non-linear convective terms are treated with the explicit Adams predictor–corrector method while the viscous terms are treated with the implicit second-order in time Crank–Nicolson method. Using the notation introduced in (4.8) then the time-step consists of a predictor,

$$\frac{\boldsymbol{u}^p - \boldsymbol{u}^n}{\Delta t} = \beta_0 \boldsymbol{F}_E^n - \beta_1 \boldsymbol{F}_E^{n-1} + \alpha \boldsymbol{F}_I^p + (1-\alpha)\boldsymbol{F}_I^n,$$

and a corrector

$$\frac{\boldsymbol{u}^c - \boldsymbol{u}^n}{\Delta t} = \frac{1}{2}\boldsymbol{F}_E^p + \frac{1}{2}\boldsymbol{F}_E^n + \alpha \boldsymbol{F}_I^c + (1-\alpha)\boldsymbol{F}_I^n,$$

where the superscript c denotes the corrected solution and $\alpha = \frac{1}{2}$ gives the second-order Crank–Nicolson method.

The basic Navier–Stokes solver uses a solution algorithm that decouples the pressure and velocity fields Henshaw (1994); Henshaw & Petersson (2003) in a similar fashion to many fractional-step and projection schemes, cf. Almgren *et al.* (1998); Ferziger & Perić (2002); Patankar & Spalding (1972) and many others. The advantage of the current scheme over typical projection schemes is that the boundary conditions for the pressure are well-defined and it is straightforward to obtain full second-order accuracy for all variables.

Assume that at time $t - \Delta t$ the values of $\boldsymbol{U}(t-\Delta t)$ and $P(t-\Delta t)$ are known at all points in the solution domain and the values of $\boldsymbol{F}(\boldsymbol{U}(t-\Delta t), t-\Delta t)$ are known at all interior points. To advance the solution in time to t the fully explicit algorithm proceeds as follows:

Step 1 Determine an intermediate solution $\boldsymbol{U}_{\boldsymbol{i}}^*(t)$ at all interior nodes using a predictor sub-step

$$\boldsymbol{U}_{\boldsymbol{i}}^*(t) = \boldsymbol{U}_{\boldsymbol{i}}(t-\Delta t) + \alpha \Delta t \boldsymbol{F}_{\boldsymbol{i}}(\boldsymbol{U}_{\boldsymbol{i}}(t-\Delta t), t-\Delta t), \qquad \forall \boldsymbol{i} \in \Omega$$

Step 2 Determine $\boldsymbol{U}^*(t)$ at the boundary and ghost nodes by solving the boundary conditions

$$\left.\begin{aligned} \boldsymbol{U}_{\boldsymbol{i}}^*(t) - \boldsymbol{u}_B(\boldsymbol{x}_{\boldsymbol{i}}, t) = 0 \\ \nabla_2 \cdot \boldsymbol{U}_{\boldsymbol{i}}^*(t) = 0 \\ \text{Extrapolate ghost values of } \mathbf{t}_\mu \cdot \boldsymbol{U}_{\boldsymbol{i}}^* \end{aligned}\right\} \forall \boldsymbol{i} \in \partial\Omega$$

where $\mu = 1, \dots, n_d - 1$ and only the tangential component of the momentum equation is used.

Step 3 Determine $P_{\boldsymbol{i}}(t)$ by solving the pressure Poisson equation along with the remaining boundary conditions

$$\begin{aligned} \nabla_2^2 P_{\boldsymbol{i}}(t) &= -\mathcal{J}(\nabla_2 \boldsymbol{U}_{\boldsymbol{i}}^*(t)) + \nabla_2 \cdot \boldsymbol{f}_{\boldsymbol{i}}(t), \qquad \forall \boldsymbol{i} \in \Omega \\ \boldsymbol{n} \cdot \nabla_2 P_{\boldsymbol{i}}(t) &= -\boldsymbol{n} \cdot \left[\frac{\partial \boldsymbol{U}_{\boldsymbol{i}}^*(t)}{\partial t} + ((\boldsymbol{U}_{\boldsymbol{i}}^*(t) - \boldsymbol{W}_{\boldsymbol{i}}(t)) \cdot \nabla_2) \boldsymbol{U}_{\boldsymbol{i}}^*(t) \right. \\ &\qquad \left. + \nu \nabla_2 \times \nabla_2 \times \boldsymbol{U}_{\boldsymbol{i}}^*(t) - \boldsymbol{f}(t) \right], \qquad \forall \boldsymbol{i} \in \partial\Omega. \end{aligned}$$

The normal component of the momentum equation is used here as a Neumann boundary condition for the pressure Poisson equation. The $\nu\Delta\mathbf{u}$ term has been replaced by $-\nu\nabla \times \nabla \times \mathbf{u}$ to avoid a viscous time-step restriction[2], see (Petersson, 2001) for more details.

Step 4 Given $\boldsymbol{U}^*(t)$ and $P(t)$ the pressure gradients can be computed and $\boldsymbol{F}(\boldsymbol{U}^*(t), t)$ found at interior nodes.

Step 5 Correction steps can now be taken to either increase the time-step, or as needed, to stabilise the algorithm for light rigid bodies. The correction steps consists of the Adams-Moulton corrector for the velocity followed by an additional pressure solve. For light bodies, when added mass effects are large, under-relaxed sub-iterations are used during these corrector steps to stabilise the scheme. Typically 3–7 corrector steps are used in the present work, depending on the significance of added mass effects in the problem.

For moving grids, additional steps in the algorithm are required to evolve the

[2]Solving the momentum and pressure equations of the velocity-pressure formulation separately requires boundary conditions for the pressure. When treating viscous terms implicitly, ie in a semi-implicit manner, careful consideration of the pressure boundary condition is required to ensure a time step restriction governed by the convective term only.

rigid-body equations (as discussed in the next section) and subsequently move the component grids. After the component grids have been moved the overset grid connectivity information is regenerated. Note that since the governing equations are solved in a reference frame moving with the grid, no additional interpolation is needed to transfer the solution at discretisation points from one time step to the next. As grids move, however, some unused points may become active and values at these *exposed-points* are interpolated at previous times as discussed in Henshaw & Schwendeman (2006)

For small problems (number of grid points $\mathcal{O}(10^4)$) the linear systems of equations for the velocity components and the separate system of equations for the pressure are effectively solved using direct solution methods. Larger problems necessitate iterative approaches; we use Krylov subspace methods from the PETSc library (Balay *et al.*, 2013), algebraic multigrid solvers from the the Hypre package (Falgout & Yang, 2002) and the geometric multigrid solvers for overset grids from Overture (Henshaw, 2005).

4.3.2 Fluid-solid coupling

This system of ODEs governing the particle motion is discretised in time using a Leapfrog predictor and Adams–Moulton corrector scheme. The predictor consists of

$$
\begin{aligned}
\boldsymbol{v}_b^p &= \boldsymbol{v}_b^{n-1} + \frac{2\Delta t}{m_p}\boldsymbol{F}^n,\\
\boldsymbol{x}_b^p &= 2\boldsymbol{x}_b^n - \boldsymbol{x}^{n-1} + \frac{\Delta t}{m_p}\boldsymbol{F}^n,\\
\boldsymbol{\omega}^p &= \boldsymbol{\omega}^{n-1} + 2\Delta t(-\boldsymbol{\omega}^n \times A\boldsymbol{\omega}^n + \boldsymbol{T}^n),\\
\boldsymbol{e}_i^p &= \boldsymbol{e}_i^{n-1} + 2\Delta t(\boldsymbol{\omega}^n) \times \boldsymbol{e}_i^n,
\end{aligned}
$$

and is performed before Step 1 in the time-stepping algorithm of Section 4.3.1. The corrector is

$$
\begin{aligned}
\boldsymbol{v}_b^{n+1} &= \boldsymbol{v}_b^n + \frac{\Delta t}{2m_p}(\boldsymbol{F}^n + \boldsymbol{F}^p),\\
\boldsymbol{x}_b^{n+1} &= \boldsymbol{x}_b^n + \frac{\Delta t}{2m_p}(\boldsymbol{v}_b^n + \boldsymbol{v}_b^p),\\
\boldsymbol{\omega}^{n+1} &= \boldsymbol{\omega}^n + \frac{\Delta t}{2}(-\boldsymbol{\omega}^n \times A\boldsymbol{\omega}^n + \boldsymbol{T}^n - \boldsymbol{\omega}^p \times A\boldsymbol{\omega}^p + \boldsymbol{T}^p),\\
\boldsymbol{e}_i^{n+1} &= \boldsymbol{e}_i^n + \frac{\Delta t}{2}(\boldsymbol{\omega}^n \times \boldsymbol{e}_i^n + \boldsymbol{\omega}^p \times \boldsymbol{e}_i^p).
\end{aligned}
$$

and is performed after Step 3 (pressure solve) in the time-stepping algorithm. A predictor-corrector scheme is used to facilitate the fluid-solid coupling, and to allow for sub-time-step iterations for light bodies as discussed next.

Low solid/fluid density ratios can cause the standard time-stepping routine to become unstable, owing principally to the added-mass instability (Banks *et al.*, 2014*a*). To alleviate this, under-relaxed sub-iterations are performed during the correction stages (i.e. fluid velocity solve and pressure solve) of the time-stepping algorithm. These sub-iterations are thus relatively expensive although the implicit systems are not changed during these iterations. The approach used here is similar to that used by many previous authors, although we prefer to under-relax the force on the rigid-body as opposed to under-relaxing the entire state of the rigid-body. Note that more sophisticated approaches exist to reduce the required number of sub-iterations such as those based on Aitken acceleration (Küttler & Wall, 2008; Borazjani *et al.*, 2008).

We illustrate the relaxed sub-iteration through consideration of the rigid-body velocity equation, though this is performed for the angular velocity equation as well. The force-relaxation sub-iteration replaces the update for $\boldsymbol{v}_b^{n+1}$ in the corrector step above by the iteration

$$
\boldsymbol{v}_b^{n+1,k} = \boldsymbol{v}_b^n + \frac{\Delta t}{2}(\boldsymbol{F}^n + \boldsymbol{F}^{n+1,k}), \qquad k = 1, 2, \ldots
$$

where k denotes the iteration count. The iterative forcing used to evolve the equation is

$$\boldsymbol{F}^{n+1,k} = (1-\alpha)\boldsymbol{F}^{n+1,k-1} + \alpha\widetilde{\boldsymbol{F}}^{k}, \qquad \alpha \in (0,1]$$

where α is a relaxation parameter and $\widetilde{\boldsymbol{F}}^{k}$ is the forcing at step k, which initially is simply the predicted force from the previous fluid solve step, i.e. $\widetilde{\boldsymbol{F}}^{1} = \boldsymbol{F}^{p}$. During each sub-iteration, the fluid velocity and fluid pressure are recomputed and these updated fluid values are used to compute the next approximation to the force on the rigid body. A small α can ensure stability—at the cost of increased iterations. An optimal value of α is problem dependent and some experimentation is required to reach a good compromise between stability and computational cost. For example, a value of 0.1 was used in the pure wake interaction test case of §5.1.4 where the maximum number of sub-iterations was 39 during the first few time-steps, likely due to the non-smooth forcing at start up, and the minimum and average number of sub iterations were 5 and 7, respectively. Iterations are performed until the absolute or relative change in the force fall below their respective convergence criteria, $\Delta F^k < \tau_a$, or $\Delta F^k/(|\boldsymbol{F}^k| + \epsilon_F) < \tau_r$, where $\Delta F^k = |\boldsymbol{F}^{n+1,k} - \boldsymbol{F}^k|$.

Collision model

A hard-sphere collision model based on the linear conservation of momentum is used to handle cases in which particles touch[3]. During the predictor step of the particle advancement scheme the new positions are used to determine whether or not particles breach the minimum separation distance, as stipulated by the requirements of the interpolation stencils. If this minimum separation distance is breached, a collision is deemed to have occurred and the particle velocities are corrected. The velocity corrections are calculated by

$$\hat{\boldsymbol{v}}_{b,A}^{n+1} = \boldsymbol{v}_{b,A}^{n+1} + \left[v_A^n - v_A^{n+1} - \frac{(1+e_r)m_{b,B}}{m_{b,A}+m_{b,B}}(v_A^n + v_B^n) \right] \boldsymbol{n}_A,$$
$$\hat{\boldsymbol{v}}_{b,B}^{n+1} = \boldsymbol{v}_{b,B}^{n+1} + \left[v_B^n - v_B^{n+1} - \frac{(1+e_r)m_{b,A}}{m_{b,A}+m_{b,B}}(v_A^n + v_B^n) \right] \boldsymbol{n}_B,$$

[3] Note that in principle the particles should never actually touch, but resolving the near contact would require a very fine grid.

where $v_A = \boldsymbol{v}_{b,A} \cdot \boldsymbol{n}_A$, $v_B = \boldsymbol{v}_{b,B} \cdot \boldsymbol{n}_B$, e_r is the coefficient of restitution and $\boldsymbol{n}_A = -\boldsymbol{n}_B$ is the unit normal vector pointing from the centre of mass of particle A to the centre of mass of particle B. In this work, collisions were modelled as perfectly elastic with a coefficient of restitution of $e_r = 1$. This is a frictionless model, so tangential forces are assumed to be zero during the collision, and angular velocities are not corrected by the model. This hard-sphere model is also restricted to the contact of only two particles at any given moment in time.

4.4 Non-Newtonian flow solver

For viscoplastic fluid flows we limit our attention to incompressible, non-inertial, and time-independent flow. As with the Newtonian fluid, the flow is governed by conservation of mass and momentum:

$$\boldsymbol{\nabla} \cdot \boldsymbol{\tau} + \nabla p = \boldsymbol{f}, \qquad \boldsymbol{\nabla} \cdot \mathbf{u} = 0, \tag{4.9}$$

where, as before, $\mathbf{u}$ is the velocity vector, p the pressure field, and $\boldsymbol{\tau}$ the shear stress tensor. We choose the Bingham model to close our system:

$$\begin{cases} \tau = \left(\eta + \dfrac{\tau_y}{||\dot{\gamma}||}\right)\dot{\gamma} & \text{if } ||\tau|| > \tau_y, \\ \dot{\gamma} = 0 & \text{if } ||\tau|| \leq \tau_y, \end{cases} \tag{4.10}$$

where τ_y is the material yield stress, η the plastic viscosity, and $\boldsymbol{\gamma}$ the rate of strain tensor defined as $\dot{\boldsymbol{\gamma}} \coloneqq (\nabla\mathbf{u} + \nabla\mathbf{u}^{\intercal})$, and $||\cdot||$ is the induced norm of the Frobenius inner product:

$$\boldsymbol{a} : \boldsymbol{b} \coloneqq \frac{1}{2}\sum_{ij} A_{ij}B_{ij}, \tag{4.11}$$

such that $||\dot{\gamma}|| = \sqrt{\dot{\gamma} : \dot{\gamma}}$.

When posed in the mobility sense, i.e. by prescribing a force rather than a velocity on an embedded body, we impose null force and torque constraints on the body, solving for the hydrodynamic force and torque using two additional equations:

$$\boldsymbol{F} = \int\limits_{\partial P} (-p\boldsymbol{n} + \boldsymbol{\tau}\cdot\boldsymbol{n})\,\mathrm{d}s + \boldsymbol{f}_b, \quad \boldsymbol{T} = \int\limits_{\partial P} (\boldsymbol{x}-\boldsymbol{x}_b)\times(-p\boldsymbol{n} + \boldsymbol{\tau}\cdot\boldsymbol{n})\,\mathrm{d}s + \boldsymbol{t}_b, \quad (4.12)$$

where $\boldsymbol{n}$ is the unit normal vector to the body surface, and $\boldsymbol{f}_b$ and $\boldsymbol{t}_b$ are external body force and torque, respectively.

We treat the viscoplastic Stokes problem exactly, i.e. without regularisation of the plastic dissipation term, by utilising a standard augmented Lagrangian formulation. Following Olshanskii (2009); Muravleva (2015) first, the viscoplastic Stokes equations are posed as a variational inequality, then, with the introduction of the following convex set

$$\boldsymbol{V} = \{\boldsymbol{v} \in H^1(\Omega)^2 | \boldsymbol{\nabla}\cdot\boldsymbol{v} = 0\}, \quad (4.13)$$

and the functional $\mathcal{J} : \boldsymbol{V} \to \mathbb{R}$, we have the following minimisation problem

$$\mathcal{J}(\mathbf{v}) = \frac{\eta}{2}\int\limits_{\Omega} |\dot{\boldsymbol{\gamma}}(\mathbf{v})|^2\,\mathrm{d}\boldsymbol{x} + \tau_y \int\limits_{\Omega} |\dot{\boldsymbol{\gamma}}(\mathbf{v})|\,\mathrm{d}\boldsymbol{x} - \int\limits_{\Omega} \boldsymbol{f}\cdot\boldsymbol{v}\,\mathrm{d}\boldsymbol{x}, \quad (4.14)$$

where $L^2(\Omega)$ denotes the space of square integrable functions on Ω and the Sobolev space $H^1(\Omega)$ is defined as:

$$H^1(\Omega) = \{v | v \in L^2(\Omega),\ \frac{\partial v}{\partial x_i} \in L^2(\Omega),\ \forall i = 1, \dots, d\} \quad (4.15)$$

The velocity solution $\mathbf{u}$ of the viscoplastic Stokes problem (4.9)–(4.10) minimises $\mathcal{J}$ on the convex set $\boldsymbol{V}$:

$$\mathbf{u} = \arg\min_{\mathbf{v}\in\boldsymbol{V}} \mathcal{J}(\mathbf{v}). \quad (4.16)$$

We introduce the following functional space $\boldsymbol{Q} = \{\boldsymbol{q} | \boldsymbol{q} \in L^2(\Omega)^{2\times 2}; \boldsymbol{q}^\intercal = \boldsymbol{q}\}$ and auxiliary tensor $\boldsymbol{q} = \dot{\boldsymbol{\gamma}}(\mathbf{v}) \in \Omega$, and a Lagrange multiplier field $\lambda \in L^2(\Omega)^{2\times 2}$, homogeneous to a plastic stress, that relaxes the constraint on the auxiliary tensor $\boldsymbol{q}$. This leads us to the augmented Lagrangian $\mathcal{L}_r : \boldsymbol{U} \times \boldsymbol{Q} \times \boldsymbol{Q} \to \mathbb{R}$ given by

$$\mathcal{L}(\mathbf{v}; \boldsymbol{q}; \boldsymbol{\tau}) = \frac{\eta}{2} \int_\Omega |\boldsymbol{q}|^2 \, \mathrm{d}\boldsymbol{x} + \tau_y \int_\Omega |\boldsymbol{q}| \, \mathrm{d}\boldsymbol{x} + \frac{1}{2} \int_\Omega (\dot{\boldsymbol{\gamma}}(\mathbf{u}) - \boldsymbol{q}) : \lambda \, \mathrm{d}\boldsymbol{x} + \frac{r}{2} \int_\Omega |\dot{\boldsymbol{\gamma}}(\mathbf{u}) - \boldsymbol{q}|^2 \, \mathrm{d}\boldsymbol{x}, \quad (4.17)$$

where $r > 0$ is a penalty parameter. Through the augmented Lagrangian formulation we have now posed the initial boundary value problem to a saddle point problem. We solve this using a standard Uzawa type algorithm:

Step 1 Given $\boldsymbol{q}^n \in \boldsymbol{Q}$ and $\lambda^n \in \boldsymbol{Q}$ find the solution $\mathbf{u}^{n+1}, p^{n+1}$ of the discrete Stokes problem:

$$r\Delta \mathbf{u}^{n+1} + \nabla p^{n+1} = \boldsymbol{\nabla} \cdot (\lambda^n - r\boldsymbol{q}^n), \quad (4.18)$$

$$\boldsymbol{\nabla} \cdot \mathbf{u}^{n+1} + \delta p^{n+1} = 0, \quad (4.19)$$

$$\mathbf{u}|_{\partial\Omega} = \mathbf{u}^b, \quad (4.20)$$

where $\delta \ll 1$ is a stabilisation term and $\mathbf{u}^b$ are the problem dependent boundary conditions.

Step 2 Compute the auxiliary tensor $\boldsymbol{q}^{n+1} \in \Omega$ via the fully explicit computation:

$$\boldsymbol{q}^{n+1} := \begin{cases} 0, & \text{if } |\lambda + r\dot{\boldsymbol{\gamma}}(\mathbf{u}^{n+1})| < \tau_y, \\ \left(1 - \frac{\tau_y}{|\lambda^n + r\dot{\boldsymbol{\gamma}}(\mathbf{u}^{n+1})|}\right) \frac{\lambda^n + r\dot{\boldsymbol{\gamma}}(\mathbf{u}^{n+1})}{\eta + r}, & \text{otherwise.} \end{cases} \quad (4.21)$$

Step 3 Explicitly update the Lagrange multiplier λ^{n+1}:

$$\lambda^{n+1} := \lambda^n + r(\dot{\boldsymbol{\gamma}}(\mathbf{u}^n) - \boldsymbol{q}^n). \quad (4.22)$$

Step 4 If $|\lambda^{n+1} - \lambda^n| > \epsilon$ for $\epsilon > 0$, go to *step 1*, else *end*.

If working in the mobility sense, we have an additional outer iteration loop:

Step 1 Given $\mathbf{u}_p^n, \boldsymbol{\omega}_p^n, \boldsymbol{q}^n, \lambda^n$, find the solution to the discrete Stokes problem.

Step 2 Compute the auxiliary tensor $\boldsymbol{q}^{n+1}$.

Step 3 If $|\lambda + r\dot{\boldsymbol{\gamma}}(\mathbf{u}^{n+1})| < \tau_y$ update the Lagrange multiplier λ^{n+1}.

Step 4 Compute the hydrodynamic force $\boldsymbol{F}_p^{n+1}$ and torque $\boldsymbol{T}_p^{n+1}$ on the particle and set the particle velocity $\mathbf{u}_p^{n+1}$ and angular velocity $\boldsymbol{\omega}_p^{n+1}$. If $|F^{n+1}-F^n| > \epsilon$ or $|T^{n+1} - T^n| > \epsilon$, go to *step 1*, else *end*.

Because the viscoplastic computations are steady, we do not require a collision model as in the Newtonian case.

In recent years, there have been several attempts at accelerating both genuinely non-smooth and regularised solution methods. Aposporidis *et al.* (2011) replaced the optimisation techniques of the classic ALM type methods with Picard iterations, while Saramito (2016) proposed a damped Newton method. In both methods the difficulties posed by non-differentiability and a non-unique stress field are transferred from the 'outer' loop to the 'inner' Stokes problem loop. Accordingly, these methods show faster convergence in the outer loop than ALM methods, however, suffer from slow convergence in the 'inner' loop due to singular linear systems (Treskatis *et al.*, 2018). Treskatis *et al.* (2016) proposed an accelerated ALM approach based on Nesterov (1983) predictor-corrector scheme and the fast iterative shrinkage-thresholding algorithm (FISTA) of Beck & Teboulle (2009). There, instead of the velocity (primal) based formulation, the stress (dual) based formulation is solved using the accelerated first-order optimisation algorithm FISTA, belonging to the class of proximal gradient methods. FISTA was shown to outperform classical ALM by up to two orders of magnitude, with the provably worst case convergence rate increased from $O(1/\sqrt{k})$ to $O(1/k^2)$, where k is the iteration counter.

Very recently, Bleyer (2018) applied an interior-point optimisation method to the primal dual formulation of the viscoplastic flow problem, showing even better performance than FISTA. Although regularised, the regularisation is, in a sense, adaptive such that a much smaller regularisation parameter is achieved than with traditional regularisation schemes (Treskatis *et al.*, 2018). Bleyer (2018) note that in practice, many pitfalls of regularisation do not appear to affect this interior-point method.

4.5 Conclusions

In this chapter we have given an overview of the computational strategies for the meshing—allowing for discrete particle representation—and the viscoplastic fluid solver—allowing for exact yield surface computation.

In the following chapter, we will first evaluate the overset grid method for particulate flow simulation using a Newtonian carrier fluid, making use of existing benchmark cases, before exploring viscoplastic particulate flows in the remaining results chapters.

5 Newtonian particulate flows with overset grids

Approximate solution methods have been applied to both high and low particle Reynolds number flow regimes, where by neglecting viscous or inertial contributions, respectively, the equations of motion can be linearised and solved with powerful mathematical tools; see Sangani & Didwania (1993); Kushch *et al.* (2002); Brady (1988) for examples in both flow regimes. It is the intermediate flow regime, where such approximations are not valid, that the full incompressible Navier–Stokes equations must be solved.

A wide range of numerical techniques have been developed for simulating particulate flows through solution of the full Navier-Stokes equations. These include arbitrary Lagrangian–Eulerian (ALE) methods (Takashi & Hughes, 1992; Hu *et al.*, 2001; Vierendeels *et al.*, 2005), methods based on level-sets (Coquerelle & Cottet, 2008; Gibou & Min, 2012), fictitious domain methods (Glowinski *et al.*, 1999, 2000, 2001), embedded boundary methods (Costarelli *et al.*, 2016) and immersed boundary methods (IBM) (Kajishima & Takiguchi, 2002; Uhlmann, 2005; Kim & Choi, 2006; Lee *et al.*, 2008; Borazjani *et al.*, 2008; Breugem, 2012; Kempe & Fröhlich, 2012*b*; Yang & Stern, 2012; Bhalla *et al.*, 2013; Yang & Stern, 2015; Wang & Eldredge, 2015; Kim & Peskin, 2016; Lācis *et al.*, 2016). An extensive overview may be found in Koblitz *et al.* (2017*a*).

In this chapter we will evaluate the overset grid, or Chimera grid, method for viscous particulate flow. As described in chapter chapter 4, overset grid methods have been widely used for problems with moving geometries. They were recognised early on to be a useful technique for treating rigid moving bodies, such as aircraft store separation (Dougherty & Kuan, 1989), and have subsequently been applied to many other moving-grid aerodynamic applications, see for example Meakin (1993); Henshaw & Schwendeman (2006); Zahle *et al.* (2007); Chan (2009); Chandar & Damodaran (2010); Lani *et al.* (2012). English *et al.* (2013) present a novel overset grid approach using a Voronoi grid to link Cartesian overset grids. This differs to the method used here, where interpolation stencils are directly substituted into the coefficient matrix and solid boundaries are represented using curvilinear grids. The basic approach of moving overset grids used in this chapter was developed for high-speed compressible and reactive flows by Henshaw & Schwendeman (2006) and included the support for adaptive grid refinement. The deforming composite grid (DCG) approach was developed in Banks *et al.* (2012) for treating deforming bodies with overset grids, and a partitioned scheme was developed for light deforming bodies that was stable without sub-iterations. A method to overcome the added-mass instability with compressible flows and rigid bodies was developed in Banks *et al.* (2013). More recently, stable partitioned schemes for incompressible flows and deforming solids have been developed (Banks *et al.*, 2014*a*,*b*; Li *et al.*, 2016) and extended to non-linear solids (Banks *et al.*, 2016).

The overset grid method described in chapter 4 retains much of the efficiency of static structured grid methods whilst still allowing for sharp representation of solid boundaries. The overset grid method can be seen as a bridge between the static grid methods such as IBM and boundary conformal grid methods; the curvilinear particle grids allow for higher than first-order accuracy and boundary conditions to be implemented strongly, while grid connectivity with the static Cartesian background grid is only locally updated. Since the grid connectivity is only updated locally, the regridding procedure is less costly and complex than for unstructured body conformal methods, such as ALE. Local grid refinement allows boundary layers to be fully resolved without appreciably affecting the total grid point count. This is in contrast with general static grid methods where the solver efficiency is offset by the unfavourable scaling associated with uniform grids, making large fully resolved simulations very costly (Wachs *et al.*, 2015). For these reasons, we evaluate the suitability of the method for fully resolved simulations of incompressible fluid flow with rigid particles. Note that the scheme described here is implemented in the Cgins solver that is available as part of the Overture framework of codes (`overtureFramework.org`). Although past works have described the use of Cgins for bodies undergoing specified motions (e.g. Broering *et al.* (2012)), the discussion here of the algorithm involving freely-moving rigid-bodies is new.

In section 2 the overset grid method is summarised, before stating the mathematical formulation in section 3. These equations are discretised in space and time in section 4 and 5, respectively, while section 6 presents the fluid–solid coupling methodology. A grid convergence study is performed in section 7.1 using a representative test case to determine appropriate spatial resolutions for the wake structures captured by the background grid, and boundary layer captured by the particle grid. Following this, validation cases in both two and three space dimensions are presented, comparing against published experimental and numerical results. The results of our evaluation are summarised in section 8, along with an outlook towards future work.

5.1 Numerical results

5.1.1 Convergence study

To accurately simulate viscous flows the grid resolution must be fine enough to fully capture boundary layers adjacent to solid surfaces. These can be very thin, depending on the Reynolds number of the problem as the boundary layer depth scales approximately as $1/\sqrt{\mathrm{Re}}$, see Batchelor (1967). A major advantage of boundary-conformal over static grid methods is the ability to selectively refine the grid near solid boundaries. In a detailed grid independence study of viscous flow past a static cylinder, Nicolle (2010) investigated how refinement of different areas of the grid affected the behaviour of the cylinder. Predictably, the surface resolution was found to most affect the cylinder behaviour, but the downstream wake resolution was found to affect the vortex shedding frequency of the upstream cylinder. Nonetheless, large ratios between surface and wake resolution were found to give very accurate results.

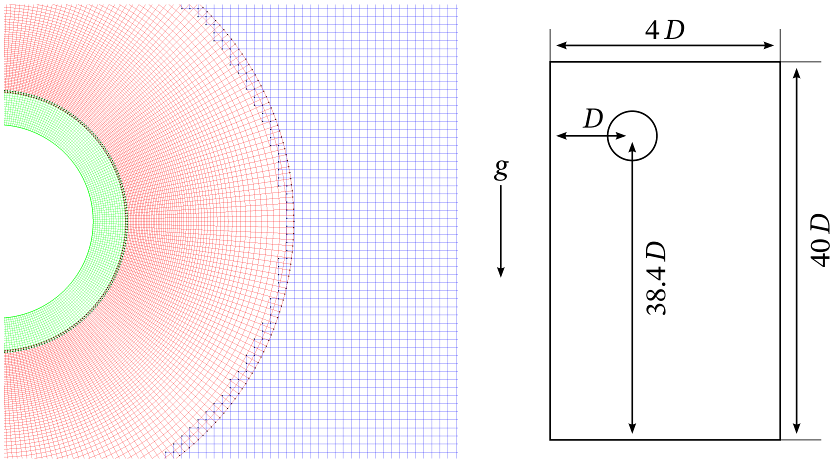

FIGURE 5.1: Left: Cropped view of *GR4*, showing the boundary layer grid (green), transition grid (red) and background grid (blue) with interpolation points. Right: Geometry of the convergence study problem.

In the present work, emphasis is placed on the grid characteristic length scales to optimise run time. Following Nicolle & Eames (2011) we use two grid length scales to quantify the quality of the computational grid: the domain length scale (*DLS*) is the background grid element size while the surface length scale (*SLS*) is the grid element size on the surface of the particle.

The grid independence study is first performed using a grid with nearly uniform grid spacings and is then repeated using grid refinement near the particle boundary. Descriptions of the grids used are provided in table 5.1. Because curvilinear grids are used to represent the particles, the cells are slightly distorted in physical space. Thus, table 5.1 provides minimum, average and maximum cell volumes (areas).

The test used in both convergence studies is as follows: the domain is a rectangular channel of dimensions $(W^*, H^*) = (4\,D, 40\,D)$ filled with an a priori quiescent fluid of density $\rho_f = 1\,\mathrm{g/cm^3}$ and kinematic viscosity of $0.05\,\mathrm{cm^2/s}$. The particle $(D, \rho_p) = (0.25\,\mathrm{cm}, 1.5\,\mathrm{kg/cm^3})$ is released from rest at $(x_0^*, y_0^*) = (D, 38.4\,D)$ with the gravitational constant set to $\boldsymbol{g} = 981\,\mathrm{cm/s^2}$ in the negative y-direction. The problem geometry can be seen in Fig. 5.1. The results are

TABLE 5.1: Description of the uniform and refined grids used in the convergence study.

Grid	Node count	Cell volume			*DLS*	*SLS*
		min	ave	max		
GU1	1497931	0.66	0.678	0.678	$D/96$	$D/96$
GU2	670984	1.47	1.53	1.53	$D/64$	$D/64$
GU3	380394	2.58	2.71	2.71	$D/48$	$D/48$
GU4	171724	5.65	6.10	6.10	$D/32$	$D/32$
GU5	98102	9.90	10.8	10.9	$D/24$	$D/24$
GU6	44967	21.3	24.4	24.4	$D/16$	$D/16$
GR1	679685	0.67	1.52	1.53	$D/64$	$D/96$
GR2	390285	0.78	2.68	2.71	$D/48$	$D/96$
GR3	191265	0.78	5.68	6.10	$D/32$	$D/96$
GR4	123095	0.71	9.09	10.9	$D/24$	$D/96$
GR5	63935	0.78	18.2	24.4	$D/16$	$D/96$
GR6	31455	0.78	39.5	97.7	$D/8$	$D/96$

non-dimensionalised as follows:

$$u^* = \frac{u}{U_T}, \quad v^* = \frac{v}{U_T}, \quad x^* = \frac{x}{D}, \quad y^* = \frac{y}{D}, \quad \omega^* = \frac{\omega D}{U_T}, \quad t^* = \frac{tU_T}{D} \tag{5.1}$$

where $U_T = 8.60\,\mathrm{cm\,s^{-1}}$ is the measured terminal settling velocity.

Under the action of gravity the particle rotates in a counterclockwise sense, as if rolling up the wall—this is known as the 'anomalous rolling' effect and is well-known in the literature (Luo *et al.*, 2007; Goldman *et al.*, 1967; Liu *et al.*, 1993; Tatum *et al.*, 2005). Luo *et al.* (2007) studied the flow field around particles released near vertical walls in inertial Newtonian fluids and found that the 'anomalous rolling' is due, in part, to the presence of the near wall. Post release, two attached vortices form behind the particle (at finite Reynolds number). The presence of the near wall suppresses the growth of the closer of the two vortices, leading to a torque on the particle that rotates it in a counterclockwise sense, i.e. the so-called 'anomalous rolling'. Immediately after release it moves a short distance towards the near wall before migrating towards its equilibrium position along the channel centreline.

The wake remains attached but is unsteady. This is reflected in the oscillatory u^* and ω^* velocity time histories, shown in figures 5.3 and 5.2. The angular velocity

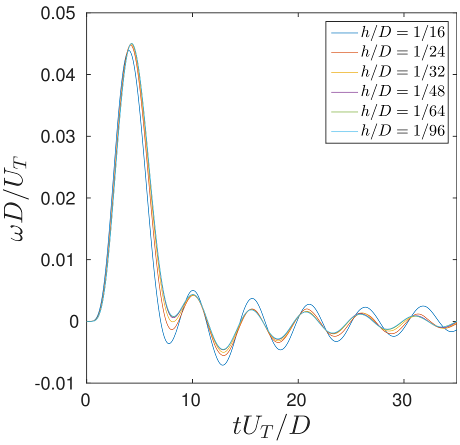

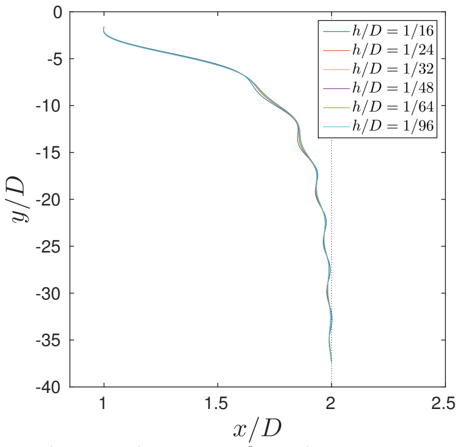

FIGURE 5.2: Left: Normalised angular velocity history for the convergence study at increasing grid resolutions. Right: Position of the disk in the channel for the convergence study at increasing grid resolutions.

time history exhibits a large initial peak after which it is rapidly damped to low amplitude oscillations about $\omega^* = 0$. After a very small negative peak, the u^* time history exhibits a large positive peak, much like ω^*, with damped successive peaks. However, unlike in ω^*, the following u^* oscillations have a non-zero mean value as the disk drifts towards its equilibrium position. In contrast, the vertical velocity, v^*, shows the particle rapidly reaching a steady settling velocity, unaffected by the attached unsteady wake.

Fig. 5.4 show relative *errors* (meaning differences compared to the reference solution) in v^* and ω^*, which were calculated as $\epsilon_v = (v^* - v^*_{\text{ref}})/v^*_{\text{ref}}$ and $\epsilon_\omega = (\omega - \omega^*_{\text{ref}})/\omega^*_{\text{ref}}$, where data from the *GU1* simulation are used as reference values. Relative errors in v^* and ω^* taken early on in the simulation, at $t = 0.2$ s, and late in the simulation, at $t = 1.0$ s, show greater than second order convergence for both components early on but a decrease in convergence rate for ω^* as the simulation progresses. The gravitational acceleration is impulsively turned on at $t = 0$, and this non-smooth forcing could have a detrimental effect on the convergence rates.

The test was repeated using a series of refined grids. These were constructed using a fine grid immediately surrounding the particle surface, smoothly connected to a coarse background grid using a transition grid. This construction

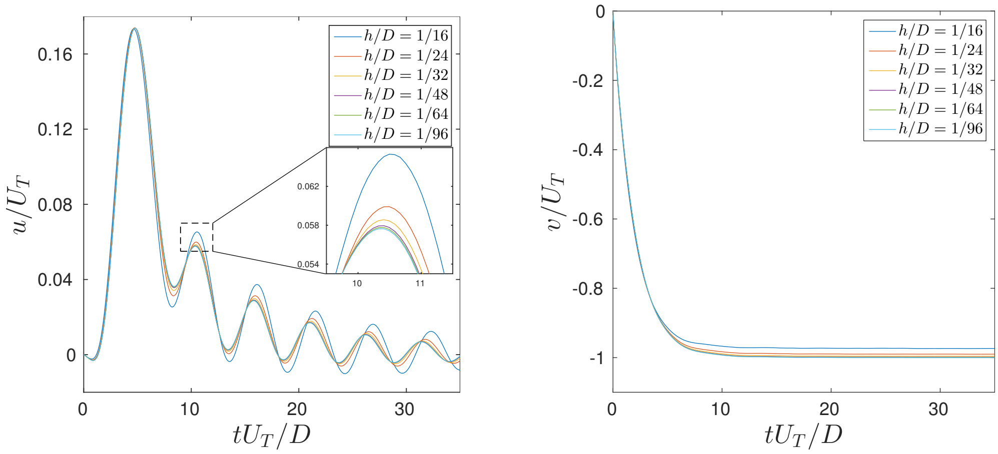

FIGURE 5.3: Left: Normalised horizontal velocity history for the convergence study at increasing grid resolutions. Right: Normalised vertical velocity history for the convergence study at increasing grid resolutions.

can be seen in Fig. 5.1. Detailed descriptions of the grids are provided in table 5.1, where uniform grids are denoted by the prefix *GU* and refinement grids by *GR*.

TABLE 5.2: Absolute values and relative errors for the convergence study taken at $t = 1.0$ s.

Grid	v/U_T	u/U_T	$\omega D/U_T \times 10^{-4}$	$\epsilon_v \times 10^{-4}$	ϵ_u	ϵ_ω
GU1	1.0000	0.0033	6.4761	—	—	—
GU2	0.9994	0.0034	6.1663	5.9299	0.0288	0.0521
GU3	0.9994	0.0034	6.8561	14.000	0.0969	0.2275
GU4	0.9957	0.0041	9.2127	43.000	0.2775	0.4609
GU5	0.9900	0.0046	9.4015	100.00	0.4513	0.6093
GU6	0.9734	0.0052	0.0016	266.00	0.6329	1.7913
GR1	0.9995	0.0034	6.5961	1.1599	0.0292	0.0277
GR2	0.9998	0.0033	6.4250	1.6028	0.0141	0.0069
GR3	1.0000	0.0031	6.4250	0.0755	0.0186	0.0062
GR4	1.0002	0.0031	5.8773	2.3025	0.0161	0.0061
GR5	1.0006	0.0032	6.1766	6.0949	0.0013	0.0573
GR6	1.0043	0.0026	6.9848	43.000	0.1915	0.1956

Table 5.2 shows absolute values of u^*, v^* and ω^* at $t = 1.0$ s as well as relative errors, where data from *GU1* were taken as reference values. As before, it is evident that v^* is fairly insensitive to the grid resolution, while u^* and ω^* show a

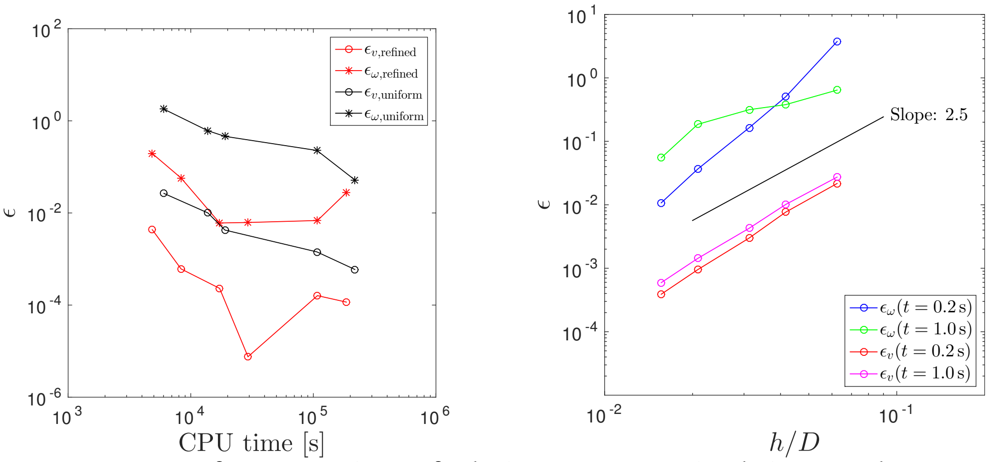

FIGURE 5.4: Left: Comparison of relative error magnitude in v^* and ω^* at $t = 1\,\mathrm{s}$ against required CPU time using uniform and refinement grids. Right: relative vertical and angular velocity errors at early ($t = 0.2\,\mathrm{s}$) and late ($t = 1.0\,\mathrm{s}$) stages of the simulation.

large dependence on the near surface resolution. With a high resolution surface grid capturing the boundary layer, the motion of the disk can be captured quite accurately, even with a large surface to background grid resolution ratio. In fact, the *GR5* grid with a resolution ratio of 6 : 1 reproduced solutions of *GU1* with a maximum error of 5 %, with a more than 23 fold reduction in number of grid points. Fig. 5.4 shows the relative error in v^* and ω^* at $t = 1\,\mathrm{s}$ against the total CPU time of the calculation.

5.1.2 Settling disk impacting a wall

This test simulates the fall of a rigid circular disk in a bounded domain and its impact with the bottom boundary. This test has been performed by other researchers using DLM/FDM (Glowinski *et al.*, 2001), an FEM fictitious boundary method (Wan & Turek, 2006), and an immersed boundary lattice Boltzmann method (Hu *et al.*, 2015). The computational domain has a width of $W = 8\,D$, a height of $H = 24\,D$ and grid characteristic length scales $DLS = D/16$ and $SLS = D/96$, where $D = 0.25\,\mathrm{cm}$ is the disk diameter. The disk is initially placed along the centreline of the domain, $8\,D$ from the top boundary. The disk has density $\rho_d = 1.25\,\mathrm{g/cm^3}$ and the kinematic viscosity of the fluid is $\nu = 0.1\,\mathrm{cm^2/s}$.

The results are non-dimensionalised as in eq. (5.1), where the characteristic velocity scale U_s is an estimated terminal velocity,

$$U_s = \sqrt{\frac{\pi D}{2}\left(\frac{\rho_d - \rho_f}{\rho_f}\right) g}. \tag{5.2}$$

The present results (Fig. 5.5) are in good agreement with the previous studies. The disk reaches the terminal settling velocity at $t^* = 20$, with a terminal particle Reynolds number of $\mathrm{Re_T} = 17.45$, consistent with the literature. As the disk approaches the bottom wall the results differ slightly. The studies compared against in Fig. 5.5 all exhibit a rebound of the disk from the bottom boundary while the present results do not.

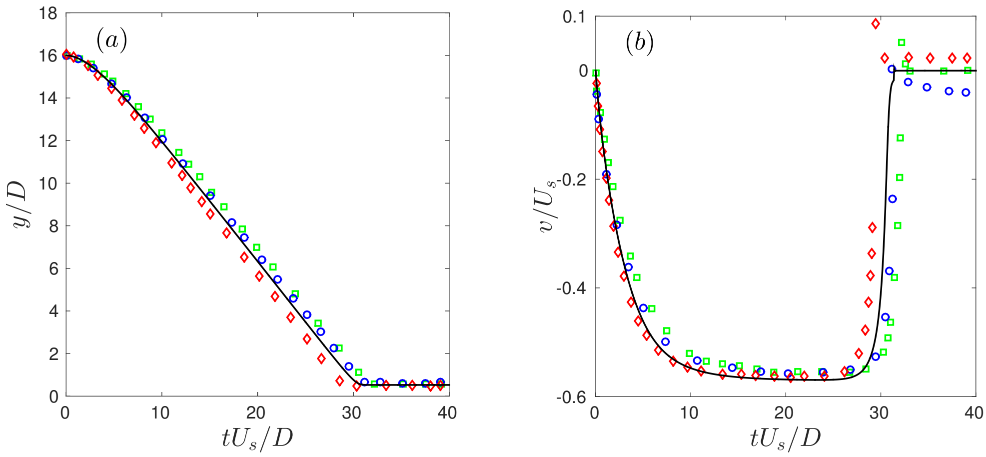

FIGURE 5.5: Histories of the y^*-coordinate and v^* component of the centre of the disk for a low Reynolds number sedimentation of a symmetrically placed disk test case with data from Hu *et al.* Hu *et al.* (2015) (□), Wang *et al.* Wan & Turek (2006) (○), Glowinski *et al.* Glowinski *et al.* (2001) (◊) and the present study (—).

In the present study the grid around the disk and along the bottom of the tank is very fine ($SLS = D/96$ for both the disk and the bottom of the tank), allowing the lubrication forces and flow in the gap to be better resolved. This slows the particle down more before "contact" is made with the wall[1]. Additionally,

[1] In fact an infinitely smooth disk with flow governed by the Navier-Stokes equations should never actually contact the wall but in this settling case only approach the wall algebraically slowly with the gap becoming ever thinner.

the present study used a conservation of linear momentum based hard-sphere collision model approach to model the collision between the disk and the bottom boundary. The previous studies compared against here all used repulsive potential type methods. We can estimate a Stokes number for the particle to comment on the “correctness” of the present results. The Stokes number, Stk, is the ratio between the particle and fluid relaxation times, τ_p and τ_f, respectively. Taking $\tau_f = R/U_T$, where R is the disk radius, $\tau_p = mv/F_d$, and F_d is the drag force on the disk, then $\mathrm{Stk} = mv^2/(RF_d)$. Once the disk reaches its terminal settling velocity the drag force balances with the force due to gravity, so $F_d = \pi R^2 g(\rho_d - \rho_f)$ and thus the Stokes number is $\mathrm{Stk} = v^2/(Rg(1 - \frac{\rho_f}{\rho_d}))$. Here, the Stokes number is approximately 2. It has been demonstrated that for 3D cases particles settling with $\mathrm{Stk} < 10$ there is no rebound after contact is made with the bottom boundary (Ardekani & Rangel, 2008; Joseph *et al.*, 2001). Assuming this holds true for the 2D equivalent, then the above results indicate that the repulsive potential collision model is a poor sub-grid model for low speed impacts. The rebound evident in the study of Glowinski et al. (Glowinski *et al.*, 2001) indicates that a higher grid resolution is required to adequately resolve the lubrication forces than the hydrodynamic interactions during free-fall. While the current approach is adequate here it is clear that in many situations resolving the gap is not practical and prohibitively expensive. Qiu *et al.* (2015) presented a novel solution to computing incompressible flow in thin gaps using pressure degrees of freedom on virtual solid surfaces to provide solid–fluid coupling in the gap region, which when extended to no-slip boundaries could be a good alternative for this sort of problem.

5.1.3 Settling of two offset disks

Two offset cylinders settling in a quiescent fluid are simulated to demonstrate the drafting, kissing, tumbling behaviour observed experimentally by Fortes *et al.* (1987). This is a difficult problem to simulate owing to the non-linear nature of the particle motion and the particle–particle and particle–wall interactions. Results are compared to previous studies of Patankar *et al.* (2000); Patankar (2001), Wan & Turek (2006), Niu *et al.* (2006), Zhang & Prosperetti

(2003) and Feng & Michaelides (2004) for a low Reynolds number case, and Uhlmann (2005) for a moderate Reynolds number case. The low Reynolds number case uses a computational domain of width $10\,D$ and height $40\,D$, with the particles of diameter 0.2 cm placed along the vertical centreline, $4\,D$ and $6\,D$ from the top boundary. The high Reynolds number case uses a computational domain of width $8\,D$ and height $24\,D$, with the particles of diameter 0.25 cm placed $4\,D$ and $6\,D$ from the top boundary, and offset by $D/250$ and $-D/250$ from the vertical centreline. For the low Reynolds number case, the grid characteristic length scales are $DLS = D/19$ and $SLS = D/76$ whilst for the moderate Reynolds number case $DLS = D/24$ and $SLS = D/128$. In each case, both the top and bottom particles have the same density ratio. For the low Reynolds number case, the density ratio is $\rho_r = 1.01$ and the fluid has kinematic viscosity $\nu = 0.1\,\mathrm{cm}^2/\mathrm{s}$. For the moderate Reynolds number case, the density ratio is $\rho_r = 1.5$ and the kinematic viscosity is $\nu = 0.01\,\mathrm{cm}^2/\mathrm{s}$. In both cases the gravitational constant was taken as $\boldsymbol{g} = 981\,\mathrm{cm/s}^2$ and the results are non-dimensionalised as in (5.1), where the characteristic velocity, U_s, is again calculated using (5.2).

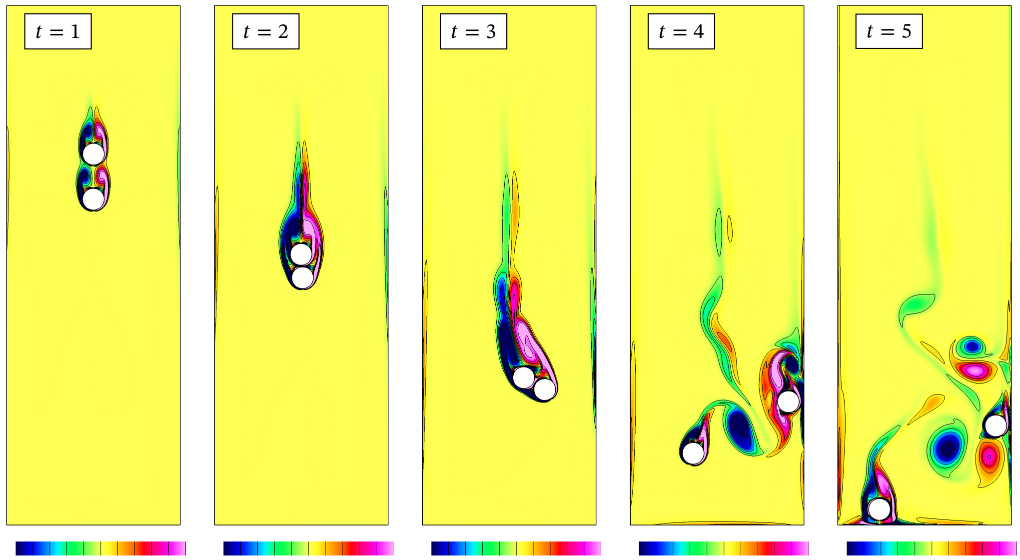

FIGURE 5.6: Settling of two disks in a quiescent fluid. Contours of the vorticity at five different time, with a vorticity scale between $-3.6 \leq \xi D/U_s \leq 3.6$.

Fig. 5.6 shows the positions of the particles as they sediment, interacting with each other and the domain boundary, along with instantaneous vorticity con-

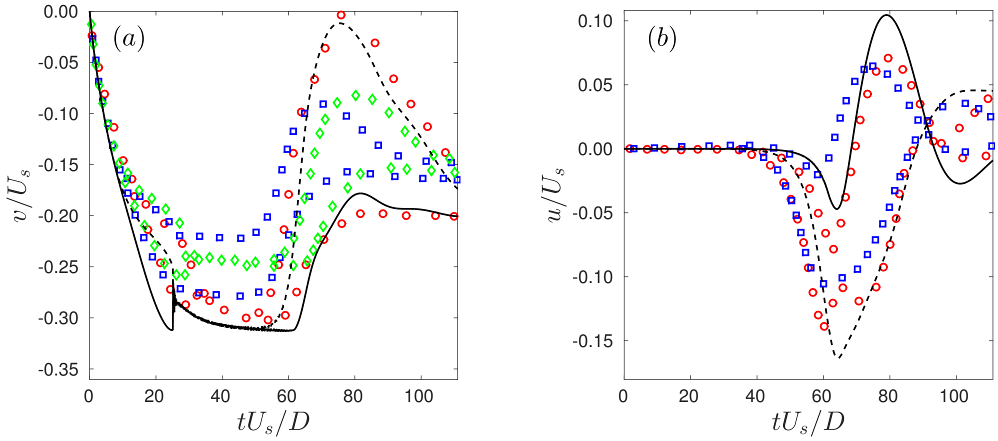

FIGURE 5.7: Histories of the (a) v^* and (b) u^* velocity components of the centre of the disks for the low Reynolds number drafting, kissing, and tumbling test case, with $\rho_d = 1.01$, $\nu = 0.1$ where the solid line denotes the (initially) top disk and the dashed line the bottom disk, with data from: (a) Patankar (2001) (◇), Patankar *et al.* (2000) (□) and Feng & Michaelides (2004) (○); (b) Patankar *et al.* (2000) (□) and Feng & Michaelides (2004) (○) overlayed.

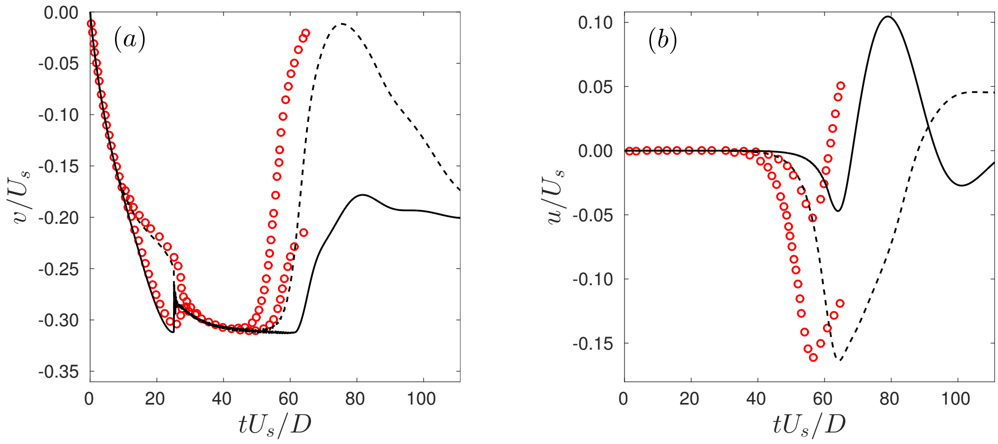

FIGURE 5.8: Time histories of the (a) v^* and (b) u^* velocity components of the centre of the disks for the low Reynolds number drafting, kissing, and tumbling test case with $\rho_d = 1.01$, $\nu = 0.1$, where the solid line denotes the (initially) top disk and the dashed line the bottom disk, and data from Zhang & Prosperetti (2003) overlayed (○).

tours. The observed dynamical interactions are in good agreement with those observed in the quasi two-dimensional experiments in Fortes *et al.* (1987). Initially, the two particles begin moving from rest under the influence of gravity with the same acceleration. As the wake forms behind the lower particle the top particle becomes shielded in the resultant low pressure region. This allows the top particle to draft behind the lower particle, similar to cyclists in a peloton. This is the “drafting” stage. Eventually, the top particle makes near contact with the lower particle (they “kiss”) and effectively form an elongated body with axis parallel to the fall. This configuration is inherently unstable and the elongated body rotates to align its long axis perpendicular to the fall. This is the “tumbling” stage described in Fortes *et al.* (1987). The particles separate and the lower particle is overtaken by the top particle, which continues to sediment with a slightly negative u^* velocity. The other particle impacts the wall, after which it, too, sediments with a slightly negative u^* velocity.

The results for the low Reynolds number case compare well qualitatively with those of Patankar *et al.* (2000); Patankar (2001); Feng & Michaelides (2004) but not quantitatively (see Fig. 5.7). Though quantitative agreement is not necessarily apparent amongst the results of these studies themselves, what is apparent is that their settling velocities are all lower than those found in the present study. Although different methods were used, all three of these simulations used low grid resolutions around the particles, particularly Feng & Michaelides (2004). The study in Zhang & Prosperetti (2003) used a higher resolution grid, with 20 computational nodes per particle diameter. Very good quantitative agreement is found between that study and the present one, as is evident from figure 5.8, though there is a discrepancy in the duration of the “kissing” contact and the onset of “tumbling”. The onset of “tumbling” is caused by the build up of numerical error, so this is expected to be solver specific. In the absence of numerical error, or bias introduced by the grid, the disks would not leave the “kissing” stage, which is why we adopt the approach of Uhlmann (2005) and Zhang & Prosperetti (2003) whereby the particles are initialised slightly offset from the centreline so as to promote an earlier onset of tumbling in a high resolution simulation.

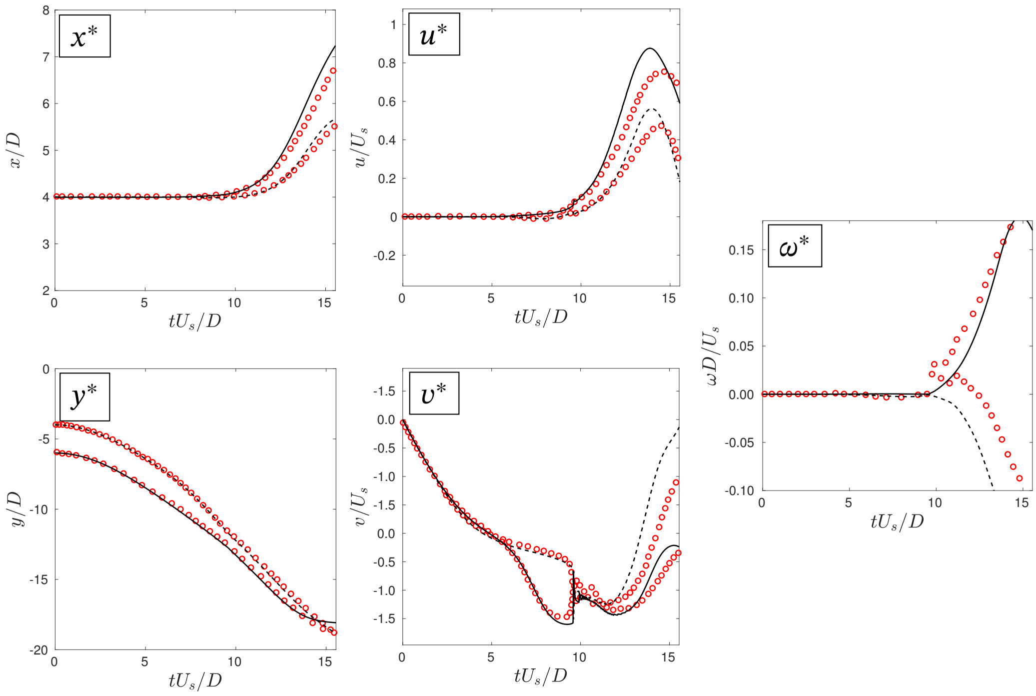

FIGURE 5.9: Time histories of x^*, y^*, v^*, u^* and ω^* for the moderate Reynolds number drafting, kissing, and tumbling test case with $\rho_d = 1.5, \nu = 0.01$, where the solid line denotes the (initially) top disk and the dashed line the bottom, and data from Uhlmann (2005) overlayed (o).

Results for the moderate Reynolds number case are shown in Fig. 5.9. These are compared to results from Uhlmann (2005), who used an immersed boundary method on high resolution grids. Both qualitatively and quantitatively the results are in excellent agreement for the particle positions and u, v velocity components, with the only differences found during the initial contact and subsequent “kissing” stage, due to the different collision models. All of the aforementioned studies used a repulsive force based model, while a conservation of linear momentum model is used here. Fig. 5.9 shows good qualitative but poor quantitative agreement for the angular velocity component. This is a very sensitive metric (Uhlmann, 2005) and it is likely that the differences are due, in large part, to the different collision mechanisms used. The novel approach of Kempe & Fröhlich (2012*b*), which uses a sub-grid lubrication force correction and conserves angular momentum, would probably be a more appropriate collision mechanism for this case.

5.1.4 Two particle wake interaction

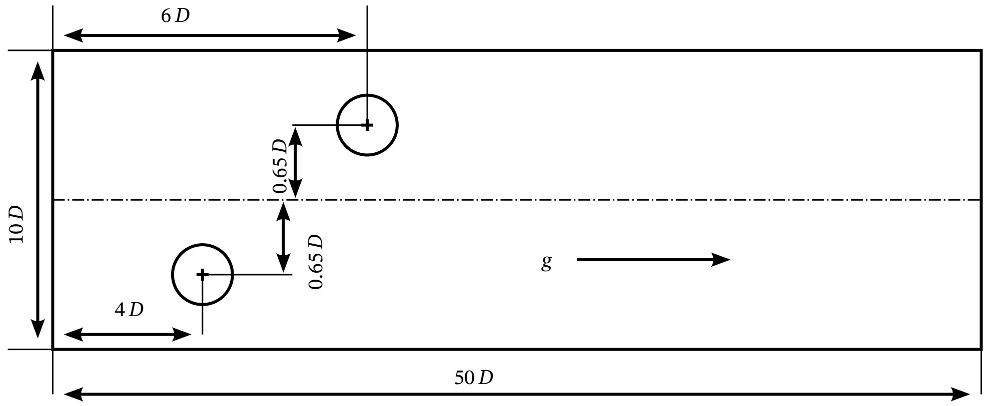

FIGURE 5.10: Problem geometry for the two particle wake interaction test case.

This is a case presented by Uhlmann (2005) to test the fluid–structure interaction, with particular emphasis on examining the effect of wake interactions between the particles on the angular velocity. Two particles of differing densities settle in an otherwise quiescent fluid. The heavier particle passes the lighter particle, subjecting it to perturbations from its wake. The particles do not collide and therefore no collision model is required, making it an attractive benchmark case.

The computational domain, shown in Fig. 5.10, has a width of $10\,D$, a height of $50\,D$ and the grid characteristic length scales are $DLS = D/40$ and $SLS = D/100$, where the particle diameter is $D = 0.2\,\mathrm{m}$. A heavier particle of density ratio $\rho_{r,1} = 1.5$ is initially positioned at $\boldsymbol{x} = (-0.65\,D, 4\,D)$ from the channel centreline and top boundary respectively, while the lighter particle of density ratio $\rho_{r,2} = 1.25$ is positioned at $\boldsymbol{x} = (0.65\,D, 6\,D)$. Both particles are initially at rest and the fluid of kinematic viscosity $\nu = 0.0008\,\mathrm{m}^2/\mathrm{s}$ is quiescent at $t = 0\,\mathrm{s}$. The gravitational constant is set to $\boldsymbol{g} = 9.81\,\mathrm{m}/\mathrm{s}^2$. The results are non-dimensionalised as in (5.1), where the characteristic velocity U_s is calculated

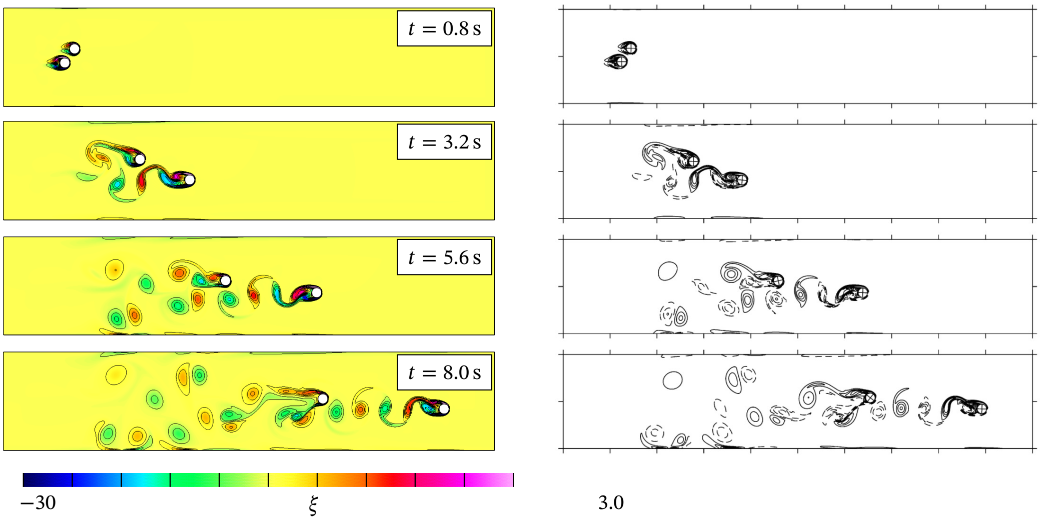

FIGURE 5.11: Contours of vorticity at times $t = 0.8\,\text{s}$, $t = 3.2\,\text{s}$, $t = 5.6\,\text{s}$, $t = 8.0\,\text{s}$ for the pure wake interaction test case compared to plots from Uhlmann (2005) taken at the same times and with the same vorticity extrema. Left: present study using a quasi uniform grid with *DLS=D/40* and *SLS=D/40*. Right: results from Uhlmann (2005) computed on a uniform grid of resolution $D/40$.

using (5.2) and the density ratio of the heavier disk, viz. $\rho_{r,1} = 1.5$.

The maximum particle Reynolds numbers of the heavy and light particle are 280 and 230, respectively (Uhlmann, 2005). Uhlmann (2005) used a uniform grid resolution of $DLS = D/40$, allowing for fewer than three grid points across the estimated boundary layer depth for both the light and heavy particles. Given the findings of the convergence study in section 5.1.1 it is not likely that the solutions at this grid resolution are grid independent. A brief convergence study was performed, shown in table 5.3, and solutions were found to converge at $SLS = D/100$, allowing for 6 points across the boundary layers for both the light and heavy particle.

Fig. 5.11 shows successive snapshots of the instantaneous vorticity field with snapshots from Uhlmann (2005) below. The evolving flow field and particle positions match well. Fig. 5.12 shows the time histories of the particles position, velocity and angular velocity.

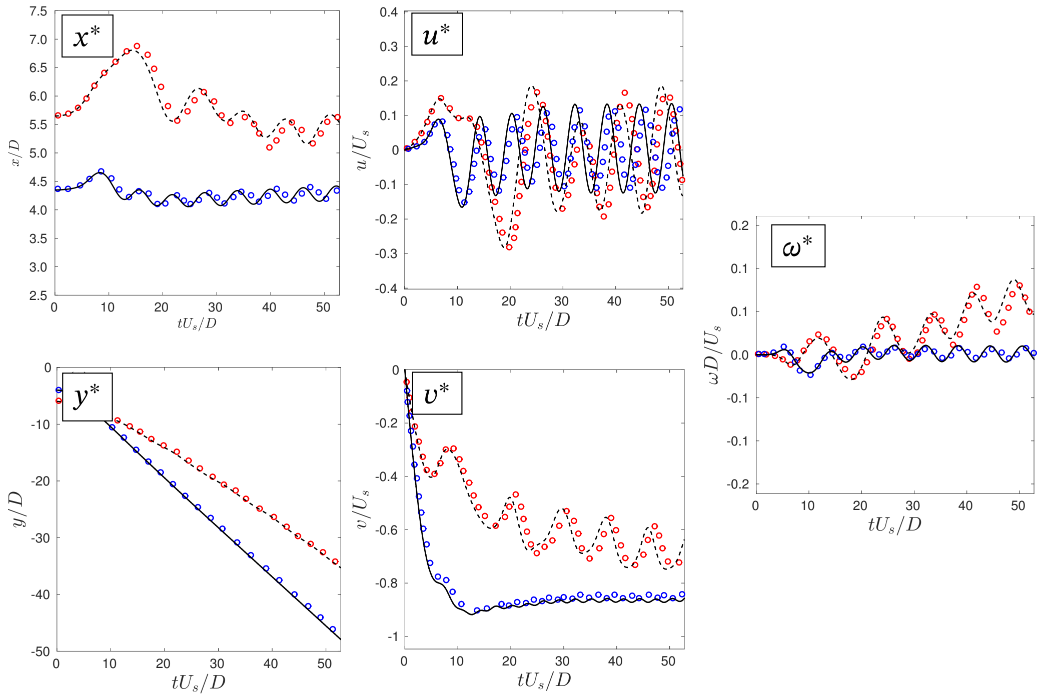

FIGURE 5.12: Time histories of x^*, y^*, v^*, u^* and ω^* for the pure wake interaction test case with $\rho_{r,1} = 1.5$, $\rho_{r,2} = 1.25$, $\nu = 0.0008\,\mathrm{m^2/s}$ and data from Uhlmann (2005) overlayed.

The converged solutions of the present study match well with those in Uhlmann (2005), although a phase shift is apparent in the oscillatory components and the settling velocity is slightly higher in the present study.

The largest differences are found in the horizontal velocity components, particularly for the light particle. These differences are probably due in large part to the differences in the angular velocity components, which will affect vortex shedding and lift on the particles. The amplitudes of the angular velocity component oscillations for the heavier particle match well but a slight phase shift is apparent. This is reflected in the horizontal velocity components for the heavier particle by matching amplitudes but markedly different periods of oscillation. The angular velocity components of the lighter particle differ in both amplitude and period of oscillation, leading to more pronounced differences in the horizontal velocity components of the two studies.

TABLE 5.3: Absolute values and relative errors for disk 2 taken at $t = 1$ s of the wake interaction grid independence study.

SLS	u/U_s	v/U_s	$\omega D/U_s$	ϵ_u	ϵ_v	ϵ_ω
D/200	0.14550	-0.36470	-0.01123	—	—	—
D/150	0.14554	-0.36483	-0.01225	0.00028	0.00033	0.00181
D/100	0.14567	-0.36518	-0.01132	0.00121	0.00130	0.00831
D/50	0.14680	-0.36705	-0.01205	0.00896	0.00643	0.07353
D/40	0.01479	-0.36847	-0.01293	0.01644	0.01033	0.15205

5.1.5 Settling sphere

As a final validation case we compare experimental (ten Cate *et al.*, 2002) and numerical (Yang & Stern, 2015) results on the motion of a single sphere in a closely confined container to numerical results produced by the current method. The sphere of diameter $D = 15$ mm and density $\rho = 1120\,\mathrm{kg/m^3}$ is positioned centrally with the bottom of the sphere 120 mm from the bottom of the tank, which has *depth* $\times$ *width* $\times$ *height* dimensions of $100 \times 100 \times 160$ mm. Four cases were run, with Reynolds numbers ranging from 1.5 to a moderate 31.9. The material parameters used in each case are detailed in table 5.4, with $\boldsymbol{g} = 9.81\,\mathrm{m/s^2}$ throughout. For each case the grid characteristic length scales are $DLS = D/10$ and $SLS = D/38$, allowing for approximately six points across the estimated boundary layer depth for the highest Reynolds number case.

TABLE 5.4: Parameters used for the four settling sphere cases.

Case number	ρ_f [kg/m^3]	μ_f [N s/m^2]	Re [–]	Stk [–]
1	970	0.373	1.5	0.19
2	965	0.212	4.1	0.53
3	962	0.113	11.6	1.50
4	960	0.058	31.9	4.13

The sphere undergoes three distinct periods of motion after its release from rest: an initial acceleration followed by a period of steady fall at a terminal settling velocity and finally a deceleration as it approaches the wall. As the Reynolds number is increased the three stages become progressively shorter. Similar Yang & Stern (2015) the wall collisions were not considered here and the simulations

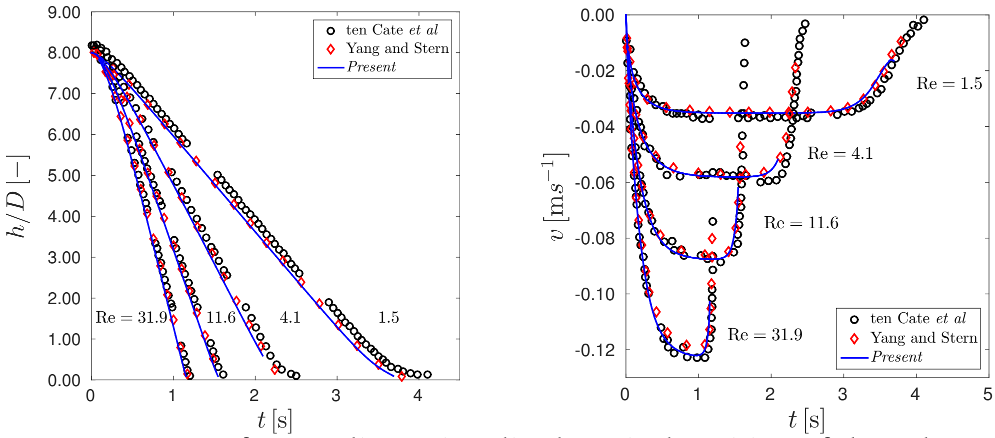

FIGURE 5.13: Left: non-dimensionalised vertical position of the sphere compared to numerical results of Yang & Stern (2015) (◊) and experimental results of ten Cate *et al.* (2002) (∘). Right: dimensional vertical velocity of the sphere compared to numerical results of Yang & Stern (2015) (◊) and experimental results of ten Cate *et al.* (2002) (∘).

stopped before the sphere made contact with the wall.

The present results are shown in Fig. 5.13 and match satisfactorily with the experimental results of ten Cate *et al.* (2002) although some slight differences remain: the terminal settling velocity in case 1 is found to be approximately 4.6 % lower here and in case 2 the sphere begins the wall induced deceleration sooner than in ten Cate *et al.* (2002). This earlier deceleration in case 2 is also present in the results of Yang & Stern (2015), as is the lower terminal settling velocity of case 1. The benefit of using overset grids is again evident; the grid used above consists of 5.18×10^5 grid points while the results are as good as those produced on a uniform grid over three times the size.

5.2 Conclusion

We evaluated the overset grid method for DNS of viscous, incompressible fluid flow with rigid, moving bodies. Several FSI benchmark test cases were carried out for verification and validation purposes. A systematic convergence test was carried out using six uniformly refined grids and six with local refinement near the particle surface. Local refinement was found to produce results deviating no more than five percent from the reference solutions, with a more than 23 fold decrease in grid point count and a subsequent 13 fold decrease in CPU time.

Results compared favourably with those from the literature for the symmetrically placed disk settling in a tank. Discrepancies in the approach and rebound behaviour are due to the hard-sphere collision model and the selective grid refinement, allowing lubrication forces to be better resolved in the current study. The present method compared well with high resolution studies for the dropping, kissing, tumbling test cases and the pure wake interaction test case. Finally, results for a sphere settling in a small tank at various Reynolds numbers compared well with both experimental results of ten Cate *et al.* (2002) and recent numerical results of Yang & Stern (2015), using only one third the number of grid points as the latter study.

The popular test cases presented in this work are all, to varying degrees, inertially dominated and exhibit viscous boundary layers that must be fully resolved to accurately simulate the behaviour of the rigid bodies in the flow. The second-order accurate boundary fitted method demonstrated here was found to produce reasonably converged results with approximately six grid points across the estimated boundary layer depth. By using a coarse—but fine enough to resolve wake structures—Cartesian background grid and refined, boundary-fitted grids, grid point counts were greatly reduced, even in two-dimensional problems.

The overset grid method has shown promising capabilities for fully-resolved DNS of small numbers of rigid particles. With a more sophisticated collision mechanism, e.g. the multi-scale approach of Kempe & Fröhlich (2012*a*) or the DEM approach of Wachs (2009), fully-resolved DNS of larger numbers of arbitrarily shaped particles could be performed. Without modification to the underlying discretisation technique other types of flow, for example arbitrarily moving bodies in non-Newtonian flows, could be examined.

In this chapter we have applied the overset grid method to particulate flow problems in Newtonian fluids. In subsequent chapters we will extend this to particles in viscoplastic fluids, starting with two particle systems in the next chapter before moving on to larger suspensions.

6 Viscoplastic squeeze flow between infinite circular cylinders

Complex fluids are ubiquitous in natural and industrial processes, from food processing, to lava or debris flows, to oil and gas applications. The mechanical behaviour of these fluids arises from the microstructure of the fluid, for example emulsion droplets and clays in drilling muds, or polymer chains in viscoelastic fluids. When non-colloidal particles much larger than the fluid microstructure are added, the system can be thought of as a particulate suspension in a complex (continuum) fluid. Examples of these types of systems include fresh concrete and debris flows (Ovarlez *et al.*, 2015). The hydrodynamic interaction between particles affects the suspension bulk properties and dynamics and is of great interest. In the case of a Newtonian fluid, analytical solutions exist for slow flow past spheres and cylinders (Stimson & Jeffery, 1926; Umemura, 1982) and the squeeze flow between them using asymptotic analysis. Viscoplastic fluids, of interest to this work, are characterised by a discontinuous nonlinear constitutive equation thereby introducing additional complexities when analytical solutions are sought.

So far, studies on interacting spheres and cylinders in viscoplastic flows have largely focused on drag and pressure drop (in the case of flow past arrays) of collinear arrangements, aligned either parallel or perpendicular to the flow (Liu *et al.*, 2003; Horsley *et al.*, 2004; Jie & Ke-Qin, 2006; Merkak *et al.*, 2006; Yu & Wachs, 2007; Tokpavi *et al.*, 2009; Jossic & Magnin, 2009). Numerical studies using the Bingham constitutive law have been found to be in good agreement

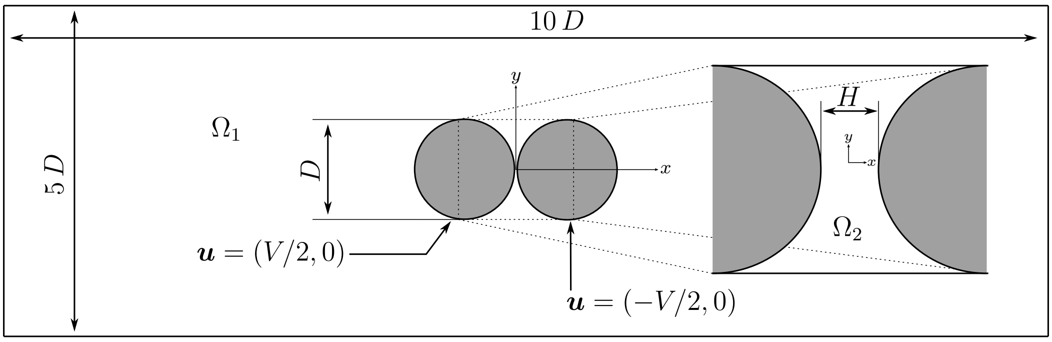

FIGURE 6.1: Schematic showing the problem geometry for the entire flow system (Ω_1) investigated through numerical methods and the reduced system (Ω_2) investigated with both analytical and numerical methods.

with experimental work using Carbopol 940 gels, developing drag correlations and stability criteria (with respect to sedimentation) (Liu *et al.*, 2003; Merkak *et al.*, 2006; Tokpavi *et al.*, 2009; Jossic & Magnin, 2009). Viscoplastic squeeze flow between coaxial cylindrical disks has been studied analytically for both planar (Muravleva, 2015) and axisymmetric (Smyrnaios & Tsamopoulos, 2001; Muravleva, 2017) configurations. The configuration of collinearly approaching bodies in a viscoplastic flow has received only cursory attention in numerical studies, eg Tokpavi *et al.* (2009); Yu & Wachs (2007), with no examination of the interstitial squeeze flow.

This study therefore examines the two-dimensional squeeze flow between two approaching infinite circular cylinders in a Bingham viscoplastic fluid by direct numerical simulation. The configuration studied is such that the gap between the two cylinders is small (1 % of the cylinder radius), as seen in fig. 6.1. We also make use of the asymptotic analysis by Balmforth (2017) to compute leading order lubrication solutions for the squeeze flow between two approaching cylinders in a Bingham fluid. We compare the analytical and numerical solutions and demonstrate that in a quasi-unconfined system the squeeze flow is greatly affected by flow external to the gap, but that the asymptotic solution may be recovered under certain flow conditions in the wider domain. This is contrary to the Newtonian equivalent, and has implications on using the viscoplastic lubrication force approximation as a sub-grid-scale model in coarse simulation techniques.

The chapter is organised as follows. In section 6.1 we present the problem of interest and briefly describe the solution strategy employed for the direct numerical simulations, and the lubrication theory calculations. In section 6.2 we present direct numerical simulations of the quasi-unconfined system. These are compared to simulations of the domain restricted to the gap only, and to the asymptotic solutions from lubrication theory. These comparisons demonstrate the influence of the wider flow field on the lubrication pressure. In section 6.3 we discuss the results and the implications for sub-grid-scale modelling.

6.1 Mathematical formulation and solution

We consider the slow, steady flow of an incompressible viscoplastic fluid around two rigid, infinite circular cylinders. The fluid has velocity $\hat{\mathbf{u}}(\hat{\boldsymbol{x}})$, pressure $\hat{p}(\hat{\boldsymbol{x}})$ and a symmetric total stress tensor $\hat{\boldsymbol{\tau}} - \hat{p}\boldsymbol{\delta}$, where variables with a hat are dimensional. In the absence of inertia, the conservation of mass is

$$\frac{\partial \hat{u}}{\partial \hat{x}} + \frac{\partial \hat{v}}{\partial \hat{y}} = 0, \tag{6.1}$$

and the conservation of momentum is

$$\frac{\partial \hat{\tau}_{xx}}{\partial \hat{x}} + \frac{\partial \hat{\tau}_{xy}}{\partial \hat{y}} - \frac{\partial \hat{p}}{\partial \hat{x}} = 0, \tag{6.2}$$

$$\frac{\partial \hat{\tau}_{yx}}{\partial \hat{x}} + \frac{\partial \hat{\tau}_{yy}}{\partial \hat{y}} - \frac{\partial \hat{p}}{\partial \hat{y}} = 0. \tag{6.3}$$

As a constitutive law we use the Bingham model

$$\begin{cases} \hat{\tau}_{ij} = \left(\hat{\eta} + \frac{\hat{\tau}_Y}{\hat{\dot{\gamma}}}\right)\hat{\dot{\gamma}}_{ij} & \text{if } \hat{\tau} > \hat{\tau}_Y, \\ \hat{\dot{\gamma}}_{ij} = 0 & \text{if } \hat{\tau} \leq \hat{\tau}_Y, \end{cases} \tag{6.4}$$

where $\hat{\tau}_Y$ and $\hat{\eta}$ are the yield stress and the plastic viscosity of the fluid, respectively, $\hat{\dot{\gamma}}_{ij}$ is the rate of strain tensor associated with the velocity field, and

$$\hat{\dot{\gamma}}_{ij} = \frac{\partial \hat{u}_i}{\partial \hat{x}_j} + \frac{\partial \hat{u}_j}{\partial \hat{x}_i}, \quad \hat{\dot{\gamma}} = \sqrt{\frac{1}{2}\hat{\dot{\gamma}}_{ij}\hat{\dot{\gamma}}_{ij}}, \quad \hat{\tau} = \sqrt{\frac{1}{2}\hat{\tau}_{ij}\hat{\tau}_{ij}}. \tag{6.5}$$

The problem geometries are depicted in figure 6.1, where the inset highlights the portion of the system considered in the analytical investigation. Aligning the system mid-plane in a Cartesian coordinate system the two cylinders are placed with their centres located at $(-H/2-D/2, 0)$ and $(H/2+D/2, 0)$, where H is the minimum separation distance and D the cylinder diameter. The computational domain for the whole system has dimensions $10\,D \times 5\,D$, which is sufficiently large for the cylinders to be essentially unconfined: waning stresses away from the moving cylinders lead to the formation of a yield envelope in the immediate vicinity of the cylinders, outside of which the fluid forms a rigid plug attached to the domain walls. Because the fluid in the far field is unyielded for the range of yield stresses explored in this study, we set no-slip boundaries at $y \pm 2.5\,D$ and pressure inlets and outlets at $x \pm 5\,D$. The cylinders have a constant relative approach velocity of V.

6.1.1 Large-scale non-dimensionalisation

Choosing a velocity scale of V, length scale of D, shear rate scale of V/D, and stress scale of $\hat{\eta}V/D$, we obtain the dimensionless equations

$$\frac{\partial u}{\partial x} + \frac{\partial v}{\partial y} = 0, \tag{6.6}$$

$$\frac{\partial \tau_{xx}}{\partial x} + \frac{\partial \tau_{xy}}{\partial y} - \frac{\partial p}{\partial x} = 0, \tag{6.7}$$

$$\frac{\partial \tau_{yx}}{\partial x} + \frac{\partial \tau_{yy}}{\partial y} - \frac{\partial p}{\partial y} = 0, \tag{6.8}$$

$$\begin{cases} \tau_{ij} = \left(1 + \dfrac{Bn}{\dot{\gamma}}\right)\dot{\gamma}_{ij} & \text{if } \tau > Bn, \\ \dot{\gamma}_{ij} = 0 & \text{if } \tau \leq Bn, \end{cases} \tag{6.9}$$

where

$$Bn := \frac{\hat{\tau}_Y D}{\hat{\eta} V} \tag{6.10}$$

is a Bingham number for the macroscopic flow external to the gap.

6.1.2 Computational method

We numerically compute the solution of equations 6.6–6.9 for two approaching cylinders with a small gap size ($H/R = 0.01$ where $R \equiv D/2$ is the cylinder radius), and calculate the resulting forces on the cylinders. To handle the disparate length scales of this problem in a computationally efficient manner we use the method of overset grids (also called overlapping, overlaid or Chimera grids) in a finite difference framework to discretise the domain. This method and grid generation algorithm is discussed in detail in Chesshire & Henshaw (1990), Henshaw (1998), and Koblitz *et al.* (2017*b*) where its efficacy for particulate flow simulations was demonstrated. Briefly, the overset grid method represents a complex domain using multiple body-fitted curvilinear grids that are allowed to overlap whilst being logically rectangular. The overlapping aspect brings flexibility and efficiency to grid generation, which is beneficial for moving body problems. Here, since the cylinders are static, the chief benefit of the overset grid method is that the grids can be locally refined near the gap whilst keeping the grids logically rectangular. The resultant linear systems are solved using the MUMPS library (Amestoy *et al.*, 2001), a massively parallel direct linear solver. We use meshes with a minimum of 15 points across the narrowest part of the gap and cluster grid points near the cylinder surfaces and wider gap region by stretching the constituent grids.

Applying a standard finite difference method to equations (6.6)–(6.9) is not straightforward, due to the non-differentiable plastic dissipation term. A straightforward way of dealing with this numerical difficulty is to regularise equation

(6.9) by removing the singularity at $\dot{\gamma} = 0$. This approach has been used in studies of viscoplastic flows past bluff bodies, see Tokpavi *et al.* (2008); Zisis & Mitsoulis (2002); Mossaz *et al.* (2010). However this can yield inaccurate results, especially for lubrication-type flows or if flow stability or finite-time stoppage are of critical interest Frigaard & Nouar (2005); Putz *et al.* (2009); Wachs & Frigaard (2016). Instead, we use an iterative method based on the variational form of the Bingham problem, established by Duvaut & Lions (1972), which forms the basis for the widely used augmented Lagrangian (AL) first proposed by Glowinski (1984). This formulation is commonly known as ALG2 and is used extensively in the literature, see Yu & Wachs (2007); Chaparian & Frigaard (2017); Muravleva (2015) and references therein, so we do not give details here. For its solution we use the Uzawa type algorithm of Olshanskii (2009) and Muravleva & Olshanskii (2008).

6.1.3 Lubrication flow in the gap

The problem shown in the inset of figure 6.1, i.e. the narrow gap between two symmetric surfaces approaching with relative speed V, has an asymptotic solution due to Balmforth (2017), if the gap H is small compared to the cylinder radius R. In this section we give an overview of this solution; in section 6.2 we will compare this to fully numerical solutions both in the restricted domain (inset of figure 6.1) and the full domain. Note that this section considers a non-dimensionalisation of the governing equations appropriate to the gap scale; the non-dimensionalisation given previously in section 6.1.1 is appropriate for the macroscopic flow. We take x to be the coordinate across the gap and y the coordinate along the gap, consistent with the setup shown in figure 6.1.

We write $\hat{\mathbf{u}} \equiv (\hat{u}, \hat{v})$ and without loss of generality

$$\hat{\boldsymbol{\tau}} \equiv \begin{pmatrix} \hat{\sigma} & \hat{\psi} \\ \hat{\psi} & -\hat{\sigma} \end{pmatrix}. \tag{6.11}$$

Following the approach in Balmforth (2017), variables are scaled as

$$x = \hat{x}/\mathcal{H}, \quad y = \hat{y}/\mathcal{L}, \quad u = \hat{u}/\mathcal{U}, \quad v = \hat{v}/(\mathcal{U}/\epsilon), \quad p = \hat{p}/\mathcal{P}, \tag{6.12}$$

where $\epsilon \equiv \mathcal{H}/\mathcal{L}$ is a small parameter. This implies the scaled continuity equation is

$$\frac{\partial u}{\partial x} + \frac{\partial v}{\partial y} = 0. \tag{6.13}$$

The stress scale is chosen as $\tau = \hat{\tau}/(\epsilon\mathcal{P})$, which implies

$$\frac{\partial p}{\partial x} = \epsilon\frac{\partial \sigma}{\partial x} + \epsilon^2\frac{\partial \psi}{\partial y}, \quad \frac{\partial p}{\partial y} = \frac{\partial \psi}{\partial x} + \epsilon\frac{\partial \sigma}{\partial y}, \tag{6.14}$$

so that the main force balance (to $O(\epsilon)$) is between the axial pressure gradient and transverse shear stress gradient. Strain rates are scaled by $(\mathcal{U}/\epsilon)/\mathcal{H}$, giving

$$\dot{\gamma} = \sqrt{\left(\epsilon^2\frac{\partial u}{\partial y} + \frac{\partial v}{\partial x}\right)^2 + \epsilon^2\left(2\frac{\partial u}{\partial x}\right)^2}. \tag{6.15}$$

The above scaling implies in the yielded regions

$$\tau_{ij} = \left(\frac{\hat{\eta}\mathcal{U}}{\epsilon^2\mathcal{P}\mathcal{H}} + \frac{\hat{\tau}_Y}{\epsilon\mathcal{P}\dot{\gamma}}\right)\dot{\gamma}_{ij}. \tag{6.16}$$

The velocity scale is set by the motion of the cylinders as $\mathcal{U} := V$ and therefore the pressure scale is chosen as

$$\mathcal{P} := \frac{\hat{\eta}V}{\epsilon^2\mathcal{H}}. \tag{6.17}$$

We additionally fix the characteristic length and gap scales as $\mathcal{L} = R$ and $\mathcal{H} = H$, respectively. This gives the scaled constitutive equation as

$$\begin{cases} \tau_{ij} = \left(1 + \frac{B^*}{\dot{\gamma}}\right)\dot{\gamma}_{ij} & \text{if } \tau > B^*, \\ \dot{\gamma}_{ij} = 0 & \text{if } \tau \leq B^*, \end{cases} \tag{6.18}$$

where

$$B^* := \frac{\hat{\tau}_Y}{\epsilon \mathcal{P}} \tag{6.19}$$

is a Bingham number for the squeeze flow in the gap[1]. Note that $B^*/Bn = \epsilon^2/2$; the squeeze flow 'sees' a much lower Bingham number than the macroscopic flow around the cylinders.

Leading-order solution

The components of the shear rate tensor are

$$\psi \equiv \dot{\gamma}_{xy} = \epsilon^2 \frac{\partial u}{\partial y} + \frac{\partial v}{\partial x}, \tag{6.20}$$

$$\sigma \equiv \dot{\gamma}_{xx} = 2\epsilon \frac{\partial u}{\partial x}. \tag{6.21}$$

Therefore, discarding terms of $O(\epsilon)$, the shear rate magnitude is

$$\dot{\gamma} = \left| \frac{\partial v}{\partial x} \right|, \tag{6.22}$$

and in the fully yielded part of the flow $\psi \gg \sigma$. Equation 6.18 is used to write

$$\psi = \frac{\partial v}{\partial x} + B^* \operatorname{sgn}\left(\frac{\partial v}{\partial x} \right), \tag{6.23}$$

and the main force balance reduces to

$$\frac{\partial p}{\partial x} = 0 \Rightarrow p = p(y), \quad \frac{\partial p}{\partial y} = \frac{\partial \psi}{\partial x} \Rightarrow \psi = x \frac{\partial p}{\partial y}, \tag{6.24}$$

the constant vanishing by symmetry, meaning that the pressure gradient is, to leading order, constant across the gap and balanced along the gap by the transverse shear stress. Exploiting the symmetry of the configuration, in the quadrant $x > 0$, $y > 0$ we must then have $v > 0$, $\frac{\partial v}{\partial x} < 0$, and so from the main force bal-

[1] Though the problem is quasi steady state the gap Bingham number is time dependent since it depends on both the approach velocity and the separation distance.

ance and constitutive law we find the velocity profile across the gap

$$\frac{\partial v}{\partial x} = x\frac{\partial p}{\partial y} + B^*, \tag{6.25}$$

which may be integrated to give

$$v = \begin{cases} -\frac{1}{2}\frac{\partial p}{\partial y}\left(\frac{1}{2}h - x\right)\left(\frac{1}{2}h - 2X + x\right), \ X < x \leq \frac{1}{2}h(y) \\ -\frac{1}{2}\frac{\partial p}{\partial y}\left(\frac{1}{2}h - X\right)^2, \ 0 \leq x \leq X, \\ -\frac{1}{2}\frac{\partial p}{\partial y}\left(\frac{1}{2}h - X\right)^2, 0 \geq x \geq -X, \\ -\frac{1}{2}\frac{\partial p}{\partial y}\left(-\frac{1}{2}h - x\right)\left(-\frac{1}{2}h + 2X + x\right), -X \geq x \geq -\frac{1}{2}h(y), \end{cases} \tag{6.26}$$

where $X \equiv B^*/|\frac{\partial p}{\partial y}|$ is the plug boundary location, and we have used a no-slip boundary condition at the cylinder surface, located at $x = \frac{1}{2}h(y)$. The continuity equation and boundary conditions imply a flow rate constraint

$$\frac{\partial}{\partial y}\int_{-\frac{1}{2}h}^{\frac{1}{2}h} v \, \mathrm{d}x = 1 \tag{6.27}$$

which, when evaluated using the velocity solution, gives a cubic equation for the pressure gradient $\frac{\partial p}{\partial y}(y)$:

$$-\frac{1}{12}\frac{\partial p}{\partial y}(h + X)(h - 2X)^2 = y. \tag{6.28}$$

It can be shown that the plug in the region $|x| < X$ undergoes $O(\epsilon)$ plastic flow, which is not present in the above asymptotic solution. This may be recovered by keeping terms $O(\epsilon)$ and is sometimes referred to as a pseudo-plug; it does not change the equation for the pressure gradient to leading order (Balmforth, 2017).

For two converging cylinders the non-dimensional separation distance is

$$h(y) = 1 + \frac{2}{\epsilon}\left(1 - \sqrt{1 - y^2}\right), \ 0 \leq |y| < 1. \tag{6.29}$$

We numerically evaluate equation 6.28 to compute $\frac{\partial p}{\partial y}(y)$ and thence $p(y)$, with an additional ambient pressure constraint outside the disks enforced as $p(1) = 0$. The leading-order lubrication force is then numerically computed as $2\int_0^1 p\,\mathrm{d}y$.

6.1.4 Flow field diagnostics

In order to classify the structure of the numerically-calculated flow fields we make use of an invariant measure of the velocity gradient tensor that gives an indication of the relative strength of the shear rate tensor and vorticity field (Davidson, 2004)

$$Q = -\frac{1}{2}\frac{\partial \hat{u}_i}{\partial \hat{x}_j}\frac{\partial \hat{u}_j}{\partial \hat{x}_i} = -\frac{1}{2}\left(\hat{\dot{\gamma}} - \hat{\omega}\right), \tag{6.30}$$

where $\hat{\omega}$ is the vorticity. We use the normalised form of (6.30)

$$\Lambda = \frac{\hat{\dot{\gamma}} - \hat{\omega}}{\hat{\dot{\gamma}} + \hat{\omega}}, \tag{6.31}$$

such that values of $\Lambda = -1, 0, 1$ correspond to flow dominated by rotation, shear, and strain, respectively (De *et al.*, 2017).

The rate of working the fluid, $\hat{\dot{W}}$, is calculated by integrating the rate of viscous dissipation, $\hat{\Phi} = \hat{\tau}_{ij}\hat{\dot{\gamma}}_{ij}$, over a suitable control volume

$$\hat{\dot{W}}(\Omega) = \int_{\Omega - V_C} \hat{\tau}_{ij}\hat{\dot{\gamma}}_{ij}\,\mathrm{d}V, \tag{6.32}$$

where V_C is the volume occupied by the cylinders. This is scaled by the force on the cylinders and the closing velocity, $\mathcal{W} = FV$, while the viscous dissipation is scaled using a characteristic energy density scale $\mathcal{E} = \eta V^2/\mathcal{H}^2$.

6.2 Results

We investigate the squeeze flow between two infinite circular cylinders in three different cases based on the set-up shown in figure 6.1. Non-dimensionalisation is as described in section 6.1.1. The external Bingham number Bn is varied between 0 and 2000 in all cases, with the minimum separation distance kept constant at 0.01 non-dimensional units (i.e. 1% of the cylinder radius), resulting in a gap Bingham number B^* range of 0 to 0.1.

Two cases use the full computational domain, labelled as Ω_1 in figure 6.1, with differing far field boundary conditions. The quiescent case (meaning here that the flow is zero outside a finite yield envelope) has velocity outlets at the vertical domain boundaries, imposing an ambient pressure of $p = 0$. No-slip and no-penetration conditions are imposed on the horizontal domain boundaries, allowing the cylinders to be surrounded by a bounded yielded region enclosed by a yield envelope.

The shear flow case considers the same geometry as the quiescent case but with the introduction of a macroscopic flow to raise the stress above the material yield stress in the far field, thus removing the yield envelope. This is done by imposing wall velocities $\pm U_w$ on the horizontal domain boundaries, resulting in a macroscopic shear rate of $\dot{\gamma} = 5$.

Finally, we consider the reduced domain labelled as Ω_2 in figure 6.1, only including the gap between the cylinders. No-slip and no-penetration conditions are applied on the cylinder surfaces, and symmetry conditions at $x = \pm 1$ in a similar manner to Frigaard & Ryan (2004) and Muravleva (2015).

We begin in section 6.2.1 with a detailed description of the flow field kinematics for the two cylinder system using the DNS results in the full computational domain. We then investigate the validity of the small gap approximation used to develop a leading order viscoplastic lubrication solution in section 6.2.2. Following this we compare pressure profiles along the the axis of symmetry, and the resultant normal force exerted on the cylinders, to solutions from viscoplastic lubrication theory in section 6.2.3. Finally, we investigate viscous dissipation in the system in section 6.2.4.

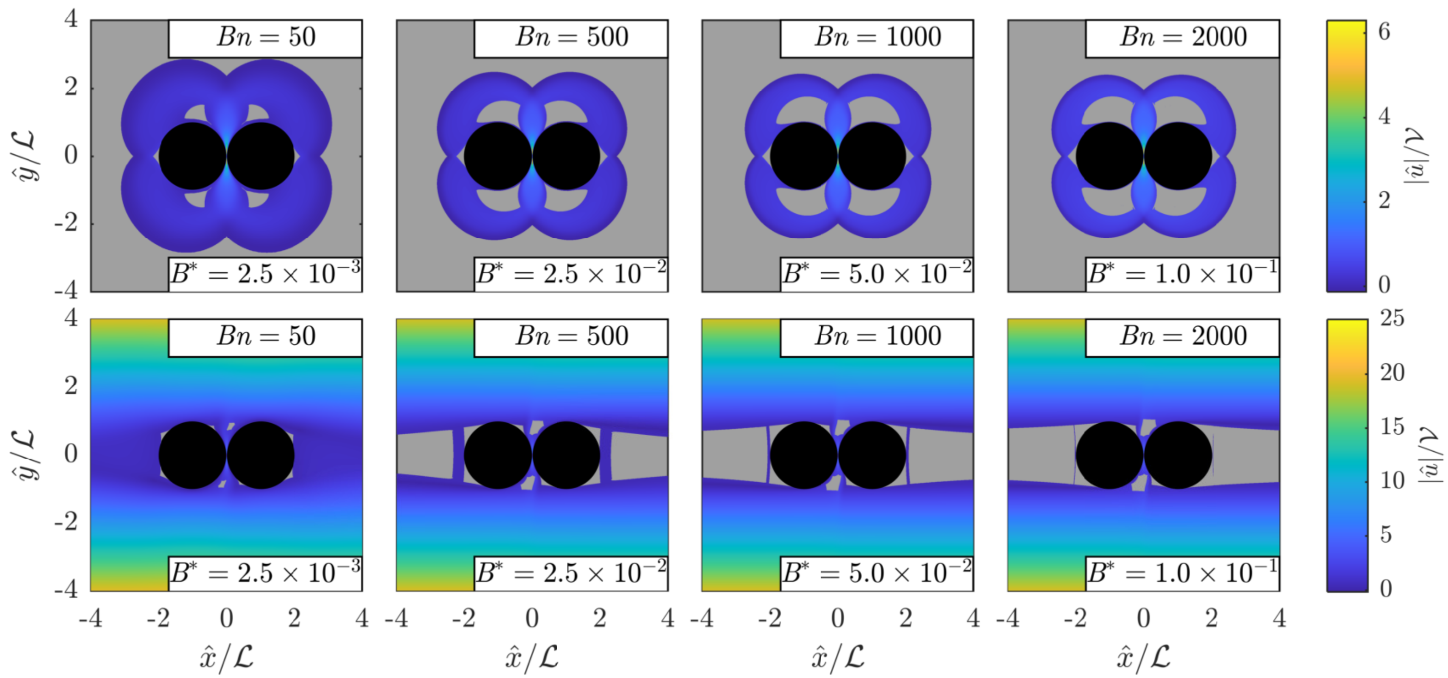

FIGURE 6.2: Velocity magnitude plots for increasing *Bn* (left to right) with quiescent conditions (top row) and macroscopic shear rate $\dot{\gamma} = 5$ (bottom row).

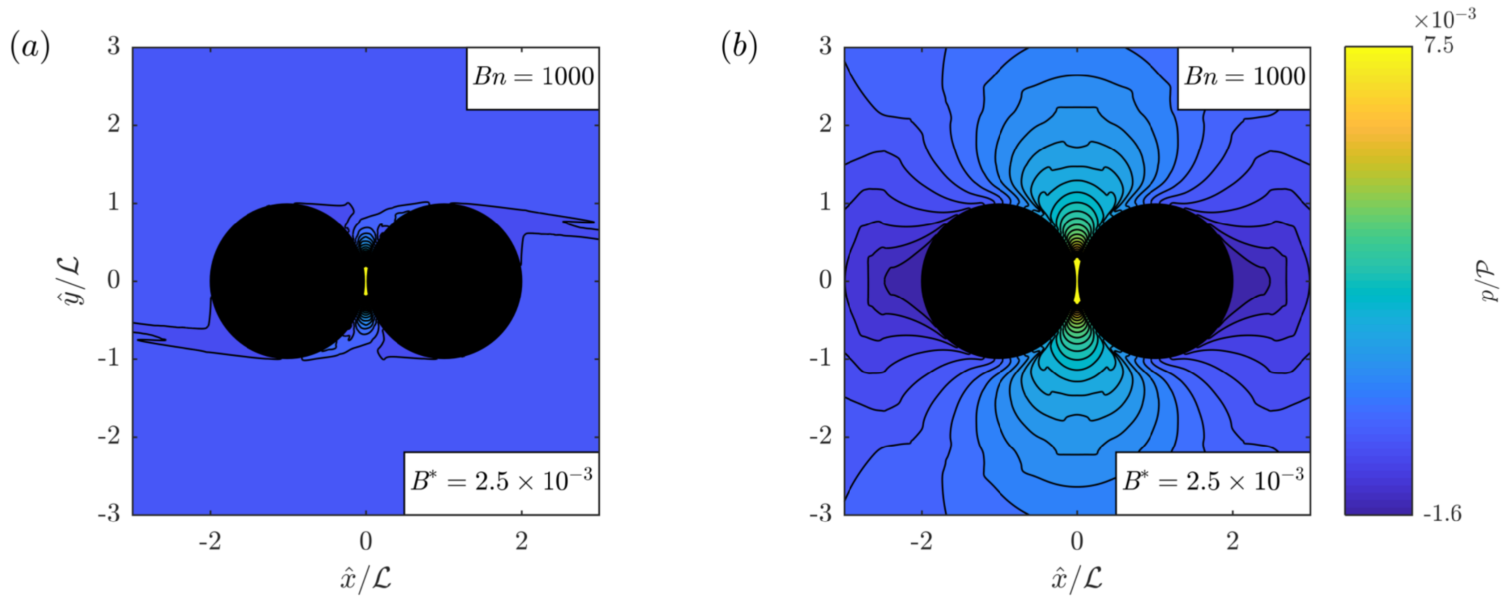

FIGURE 6.3: Pressure contours for the two cylinder system in macroscopic shear flow (left) and quiescent (right) with $Bn = 1000$.

6.2.1 Flow field kinematics

Figure 6.2 shows a binary yielded/unyielded mask in grey overlaid on colour maps of the velocity magnitude for the quiescent and sheared systems, with the Bingham number increasing from left to right. The unyielded regions are identified as areas where the second invariant of the shear stress falls below the yield stress, plus some small constant which we take as 0.1 % of the yield stress.

The top row in figure 6.2 corresponds to the quiescent case, where for $Bn \geq 50$ classical features of moving bodies in yield stress fluids can be seen: unyielded caps on the stagnation points, unyielded plugs in the equatorial planes of the cylinders, and a yield envelope fully surrounding the two cylinder system (Tokpavi *et al.*, 2008; Putz & Frigaard, 2010; Chaparian & Frigaard, 2017; Beris *et al.*, 1985; Ansley & Smith, 1967; Adachi & Yoshioka, 1973). As the Bingham number increases the unyielded stagnation caps and the equatorial plugs grow while the yield envelope shrinks.

The bottom row of figure 6.2 corresponds to the shear flow case, where the background shear flow has noticeably changed the yield surface features: stagnation points have shifted, leading to two caps on the rear of the cylinders, placed symmetrically about the longitudinal axis, and one on the front of each cylinder. The equatorial plugs are no longer present, but two unattached plugs have formed in the gap openings, placed asymmetrically about the longitudinal axis. For $Bn > 50$ central plugs can be seen fore and aft of the two cylinder system.

Figure 6.3 show contour plots of the pressure field for a quiescent (right panel) and shear flow (left panel) case at $Bn = 1000$, with the contours drawn at the same levels in both panels. The quiescent case shows a pressure drop from the gap to the rear stagnation cap, with roughly equally spaced iso-contours along shear layers attached to the cylinder surfaces and along the yield envelope boundary. In contrast, the shear flow case shows a rapid pressure decay along the gap with a more uniform pressure field outside of the gap.

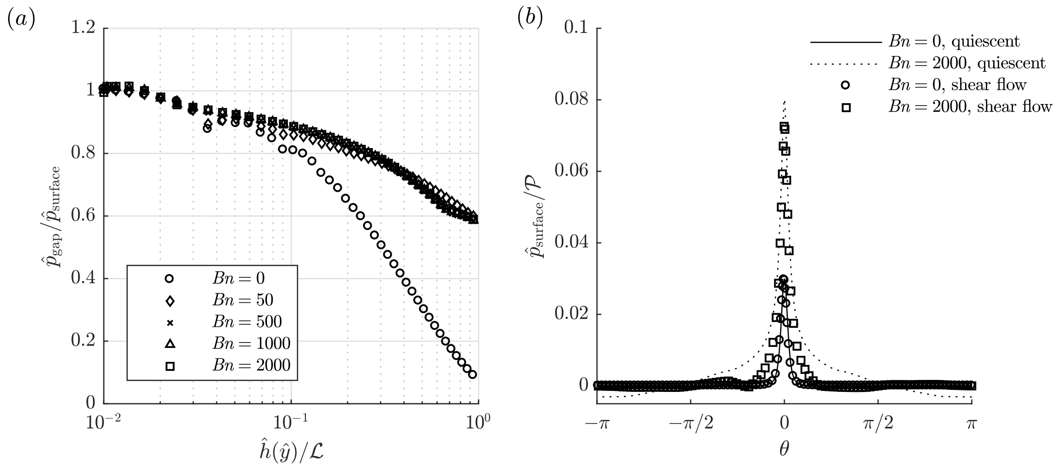

FIGURE 6.4: Left: Ratio of centreline pressure to surface pressure as a function of the local gap width for $Bn = 0$ (circles), 50 (diamonds), 500 (crosses), 1000 (triangles), and 2000 (squares). Right: Pressure distributions over the entire cylinder surface for the limiting $Bn = 0$ and $Bn = 2000$ quiescent flow cases as a function of angle away from the gap centre.

6.2.2 Small gap approximation

In section 6.1.3 a lubrication approximation was constructed which has, to leading order, pressure constant across the gap. This approximation relies on the gap being small, viz. $\epsilon \ll 1$, which is satisfied at the gap centre. However, since the approaching surfaces are elliptic (see equation (6.29)), this condition will be violated towards the gap exit.

We investigate the validity of this constant pressure solution by examining the ratio of the pressure at the gap centre to that at the surface of the cylinder as a function of the local gap width. In the left panel of figure 6.4 we plot this gap-to-surface pressure ratio against the normalised gap width as a function of y as markers for $Bn = 0$–2000 ($B^* = 0$–0.01).

For all cases, the gap-to-surface pressure ratio slowly decreases towards the gap exit, but is above 0.8 until approximately $\hat{h}(\hat{y})/\mathcal{L} > 0.1$. In the Newtonian case, the pressure ratio then rapidly decreases away from the gap centre, becoming negligible at the gap exit. All viscoplastic cases show similar behaviour to one another (as indicated by the marker overlap in the left panel of figure 6.4). The gap-to-surface pressure ratio remains close to unity close to the gap centre before slowly decreasing. Unlike for the Newtonian case, no rapid decrease is found when $\hat{h}(\hat{y})/\mathcal{L} > 0.1$ and as a result the gap-to-surface pressure remains above 0.8 further along the gap for the viscoplastic cases.

The right panel of figure 6.4 shows the pressure distributions over the entire cylinder surface, with the gap centre located at $\theta = 0$ and the gap exits at $\theta = (-\pi/2, \pi/2)$, for the limiting quiescent and shear flow cases. The Newtonian surface pressure distributions of the quiescent and shear flow cases overlap, showing a peak at the gap centre and a rapid decay towards the exits. For the high yield stress cases, the pressure distributions of the quiescent and shear flow cases are broadly similar, both showing a pressure peak in the gap centre. However, towards the gap exit the pressure decays more slowly for the quiescent case than for the shear flow case.

In isolation, the left panel of figure 6.4 shows that the leading-order solution with constant pressure across the gap, presented in section 6.1.3, is valid for only a small portion of the gap between the approaching cylinders, particularly in the absence of a yield stress. However, from the surface pressure distributions in the right panel of figure 6.4 it is clear that the overwhelming contribution to the lubrication force comes from a narrow band in the gap, where the gap-to-surface pressure ratio is above 0.9 for all cases. Therefore we expect the leading-order solution to capture the lubrication force to a good approximation.

6.2.3 Pressure profiles in the gap

Figure 6.5 presents pressure profiles through the centre of the gap, i.e. along the axis of symmetry. The direct numerical simulation (DNS) in the reduced domain gives a pressure profile in excellent agreement with the DNS of the full system in the macroscopic shear flow. Both these cases are in good agreement with the asymptotic solution from lubrication theory: peak pressures in the centre of the gap match well for the full *Bn* range explored. At higher *Bn*, the DNS pressures of the shear flow and reduced domain cases remain in agreement but decay more slowly than the asymptotic solution as the gap widens up; this is where the lubrication approximation no longer holds.

The pressure profiles for the DNS of the full system in the quiescent case are markedly different to the asymptotic solution for $Bn > 50$: higher peak pressures and slower pressure decay are evident, as is an exit pressure significantly higher than the ambient pressure (which is 0).

The relative change in peak pressure and pressure decay for increasing Bn discussed above is evident in the surface pressure distribution shown in figure 6.4. Moreover, it is evident that the pressure contribution outside of the nominal gap region is negligible. Note that for $Bn = 2000$ the pressure profiles look somewhat similar in magnitude between the quiescent and sheared cases. In fact their integrals differ by about a factor of two, implying a factor of two difference in the repulsive force; this is discussed next.

Figure 6.6 presents stacked area plots of the total drag force exerted on a cylinder, decomposed into pressure and viscous contributions. From the left panel it is clear that the force on the cylinders in quiescent fluid is dramatically underestimated when the lubrication flow in the gap is considered in isolation. Both viscous and pressure contributions increase with Bn, but the viscous contribution remains small compared to that of the pressure. Discounting the viscous friction, the pressure alone—which remains localised to the gap—causes a more than two-fold increase in the drag force over the predictions from lubrication theory. However when a macroscopic shear flow is added (the right panel in figure 6.6), the total drag force is close to the asymptotic solution. This mirrors the trend found in the pressure profiles in figure 6.5.

Figure 6.7 shows local shear rates, $\dot{\gamma}_{\mathrm{local}}$, for both the sheared and quiescent cases for the full range of Bn. We define the local shear rate as an average over a $H \times 2H$ area in the centre of the gap. The dramatic increase in pressure and drag force is not reflected in the local shear rate: the local shear rates in the quiescent and sheared cases remain in close agreement throughout the Bn range explored. From this we can conclude that the macroscopic flow does not affect the velocity field in the gap. The above computations were also performed with a macroscopic shear rate one order of magnitude higher, showing no appreciable

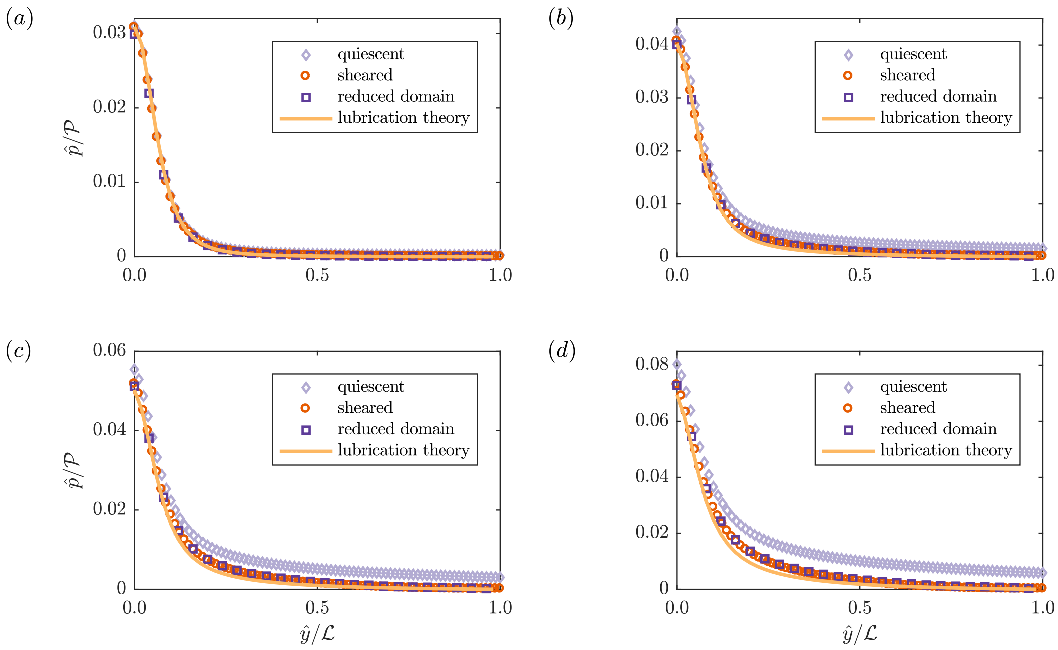

FIGURE 6.5: Pressure profile along the gap centreline for quiescent (diamonds), sheared (circles), and reduced domain (square) systems with viscoplastic lubrication solution overlayed (solid line) with $Bn = 50, 500, 1000, 2000$ in plots (a) through (d), respectively.

differences in the pressure and force results discussed above.

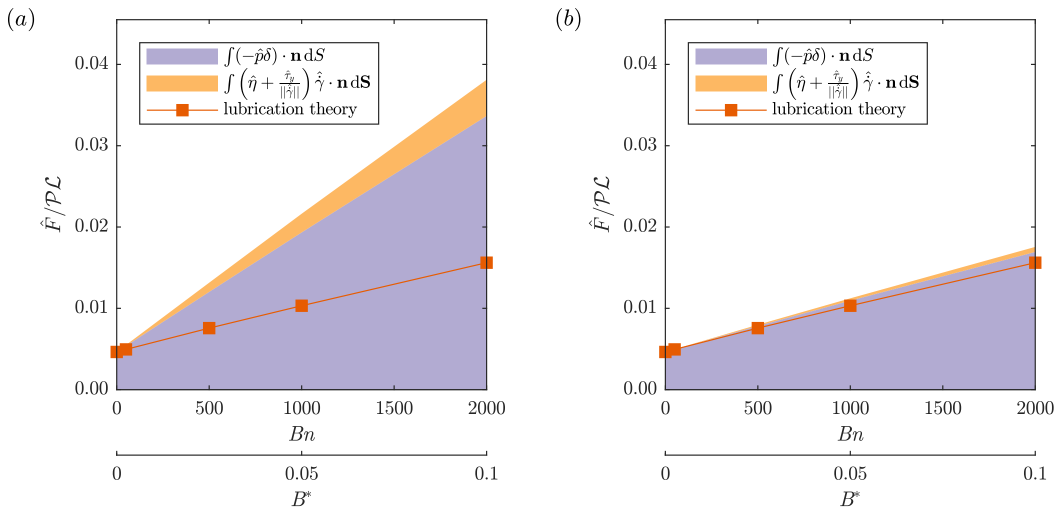

FIGURE 6.6: Stacked area plots of the total drag force on a cylinder as a function of Bn for (a) quiescent and (b) shear flow background conditions. Overlaid are the predictions from viscoplastic lubrication theory (squares).

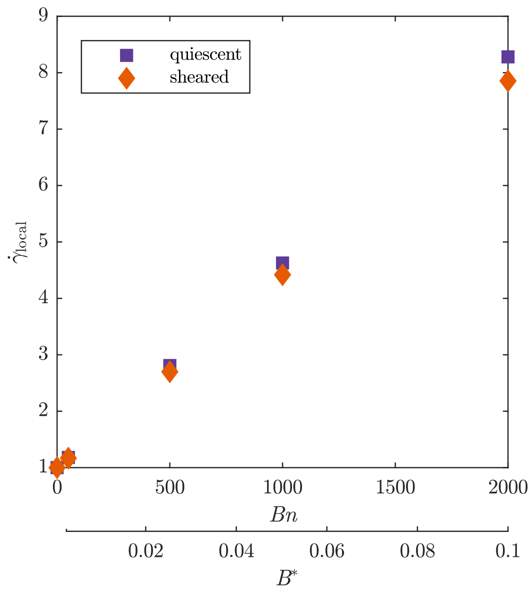

FIGURE 6.7: Local shear rates in the gap centre for quiescent (squares) and sheared (diamonds) systems for $Bn = 0, 50, 500, 1000, 2000$.

6.2.4 Viscous dissipation

The left panel of fig. 6.8 shows a colour map of $\log_{10}(\dot{\gamma})$ in a quiescent case, while the right panel shows a contour plot of the normalised second invariant of the velocity gradient tensor, indicating where the fluid is irrotational (red), rotational (blue) and being sheared (white), with the yield surface overlaid. Strain rates are highest in the thin shear layers along the cylinder surface, along the yield envelope wall, and surrounding the jet of fluid squeezed out of the gap. Strain dominated regions are found in the core of the fluid jet squeezed out of the gap, and in the regions between the rotating plugs and the yield envelope. The strain rate in these plastic flow regions is orders of magnitude lower than in the adjacent shear layers.

The left panel of fig. 6.9 shows a colourmap of $\log_{10}(|\hat{\boldsymbol{u}}|/\mathcal{V})$ in a quiescent case, while the right panel shows a contour plot of the streamfunction Ψ with yield surface locations marked out. The equidistant streamfunction contours in the vicinity of the unyielded plugs show that the plugs are undergoing rigid body rotation. These are likely to be artefacts of the Bingham model, as it involves instantaneous unyielding as fluid parcels enter the plug zone, and yielding as they leave the plug zone.

We turn now to the energy dissipation in the fluid. The left panel of figure 6.10 shows the rate of mechanical dissipation as a function of the topology parameter Λ. As would be expected, no dissipation occurs in the regions undergoing rigid body rotation ($\Lambda = -1$). Some dissipation is evident in the irrotational regions ($\Lambda = 1$) at high Bingham numbers, this is attributed to pseudo-plug regions where the flow is held close to the yield stress (Walton & Bittleston, 1991).

In all cases the dissipation is highest in regions of shear, peaking at $\Lambda = 0$. While the rate of mechanical dissipation decreases monotonically as the flow becomes rotationally dominated, for $Bn > 0$ as the flow becomes dominated by strain there exists a second, small peak in dissipation which decays slowly as Λ approaches 1.

The right panel of figure 6.10 shows the rate of work done on the fluid in different regions and flow structures for the full and reduced systems, as well as the power

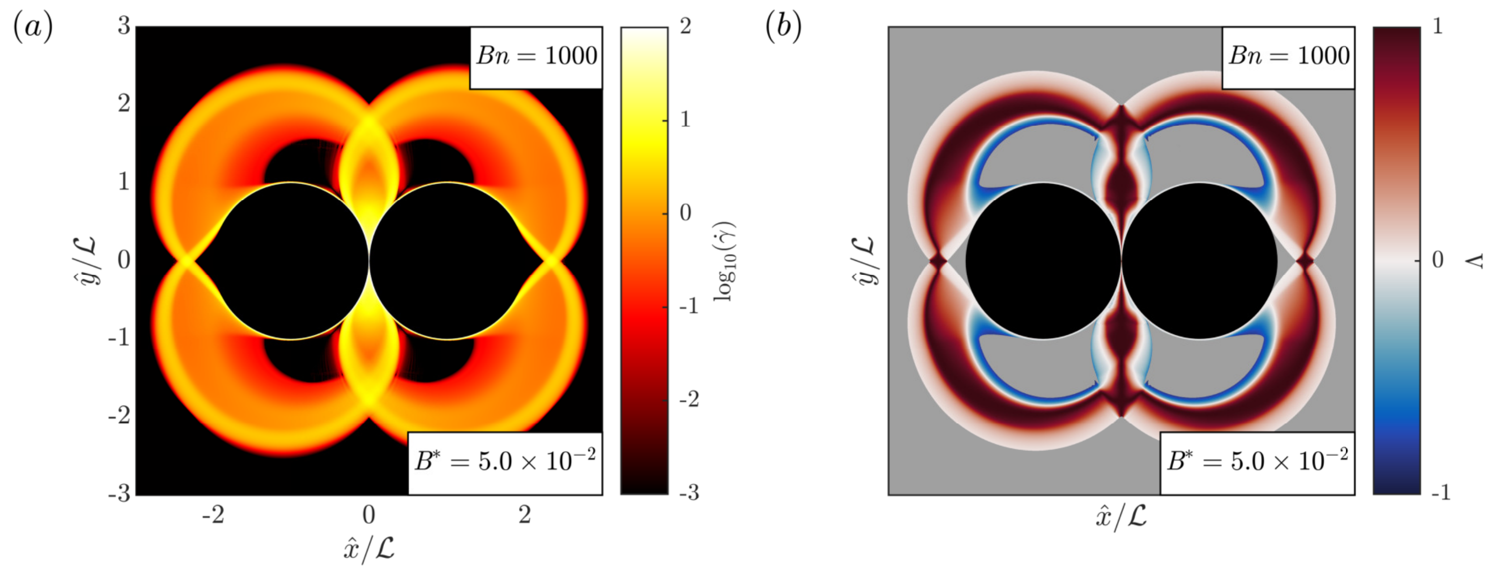

FIGURE 6.8: (a) Colour map of $\log_{10}(\dot{\gamma})$ and (b) normalised second invariants of the velocity gradient tensor with unyielded areas masked in grey with $Bn = 1000$ (quiescent case).

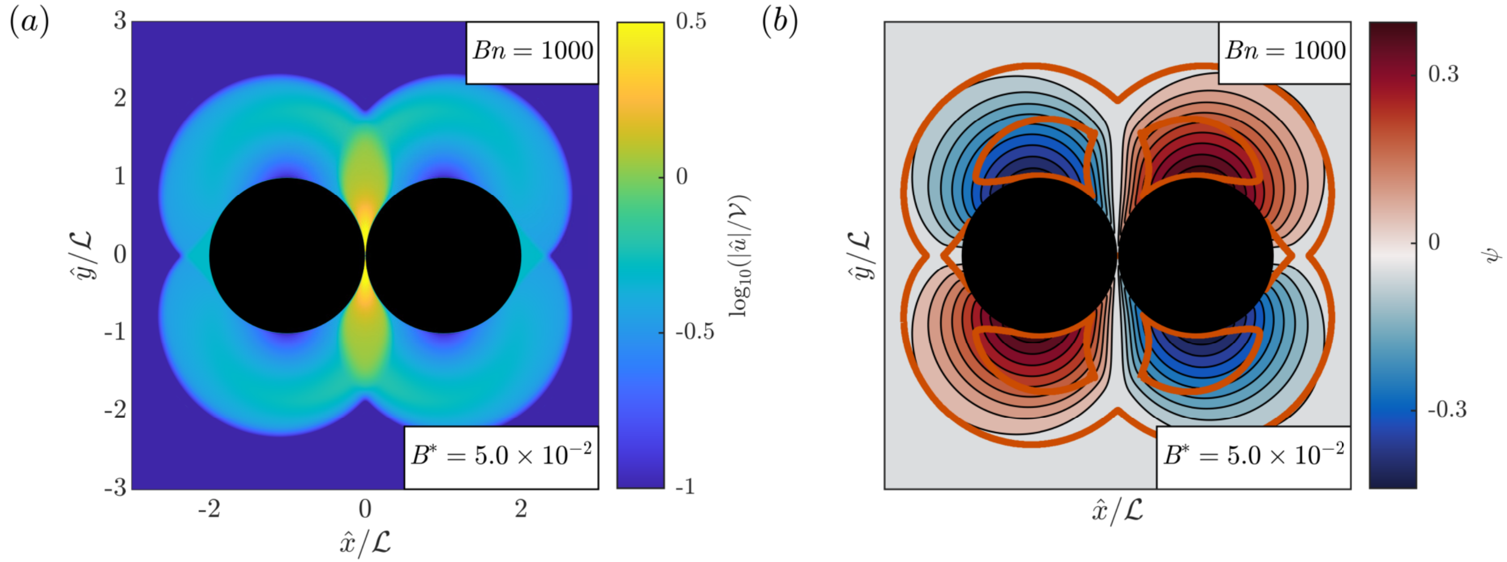

FIGURE 6.9: (a) Colour map of $\log_{10}(|\hat{\boldsymbol{u}}|/\mathcal{V})$ and (b) streamfunction with yield surface borders marked in brown, where for both cases $Bn = 1000$ (quiescent case).

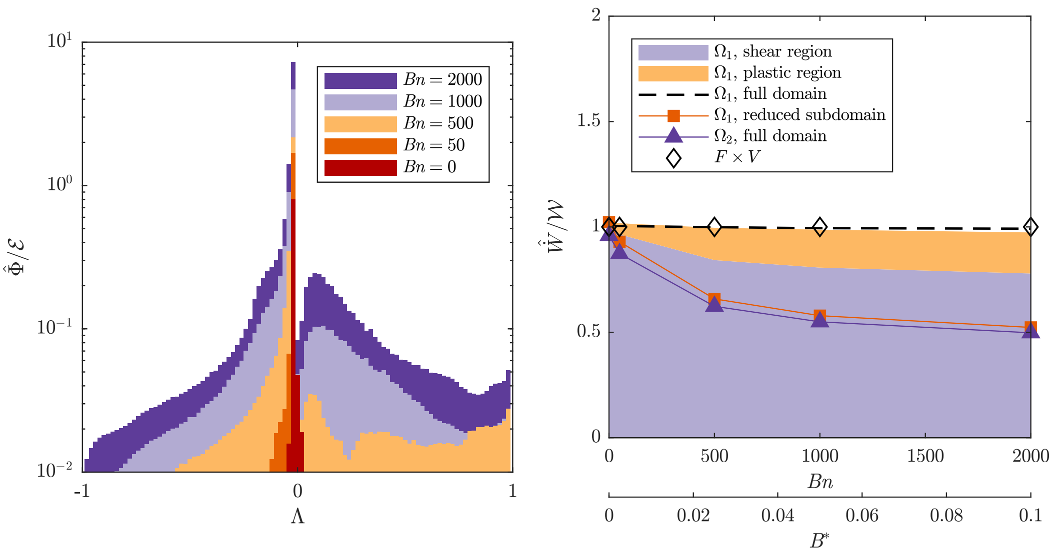

FIGURE 6.10: Left: rate of mechanical dissipation per unit Λ. Right: stacked area plot showing the rate of work done by viscous dissipation in the shear and plastic regions, scaled by $\mathcal{W} = FV$, with markers indicating the power required to move the cylinders with the approach velocity (diamonds), the total viscous dissipation in the system (dashed line), the viscous dissipation in the gap region of the full system (squares) and the total viscous dissipation in the reduced system (triangles).

required to move the cylinders with the set approach velocity. Shear regions and plastic regions have been defined as areas where $-1/3 \leq \Lambda \leq 1/3$ and $\Lambda > 1/3$, respectively (De *et al.*, 2017). While the dissipation in plastic flow is small compared to that in shear flow, it still forms a significant source of viscous dissipation outside of the gap area due to the size of the plastic flow regions (see figure 6.8). Finally, the rate of work done in the gap region is very similar for both the full (Ω_1) and reduced (Ω_2) domains. This shows that the excess drag force on the cylinders in the full domain compared to lubrication theory (figure 6.6(a)) arises from energy dissipation external to the gap.

6.3 Conclusions

In this chapter we have presented results on the squeeze flow between two infinite circular cylinders in a Bingham fluid, which we use as a simple model for the flow of non-colloidal particles in a viscoplastic fluid. Understanding this flow is essential to building models of the large-scale flow of such suspensions. Although the calculations presented here have been two-dimensional, we expect similar phenomena will occur in three dimensions (where the particles would be spheres).

In section section 6.2 we presented results from three numerical experiments: two modelling the approaching cylinders within a quiescent and a sheared fluid, and one modelling just the gap between the approaching cylinders, removing any external influence. We showed that unlike for a Newtonian fluid, the macroscopic flow external to the gap has a large effect on the lubrication forces felt by two cylinders in near-contact. In a quiescent Bingham fluid, the lubrication forces were approximately double those predicted by viscoplastic lubrication theory, but were still caused primarily by the localised high lubrication pressure in the gap, as for a Newtonian fluid. The high lubrication pressure compared to theory is due to the enclosing yield envelope which forms around the two particle system and causes a recirculating flow, introducing significant viscous dissipation into the system. Most of the extra viscous dissipation occurs in shear layers along the cylinder surface and yield envelope walls, although at high Bingham numbers the contribution from plastic flow regions near the yield envelope becomes appreciable.

Introducing a macroscopic shear flow or modelling just the gap area between the cylinders gave nearly identical results, and agreed closely with the predictions from lubrication theory. We conclude that the background shear flow acts to eliminate the yield envelope in the macroscopic flow around the particles. This in turn removes the recirculating flow and complex flow structures, where large sources of viscous dissipation in the quiescent case appear, and hence lowers the lubrication pressure and resulting lubrication force. The resulting pressure profiles in the gap are well-described by lubrication theory local to the gap. The results indicate that the macroscopic shear rate does not appreciably affect the velocity field in the narrow gap region. This conclusion is insensitive to the exact macroscopic shear rate used, provided the yield envelope is removed.

The above implies that lubrication force models using an effective viscosity based on the local shear rate (such as the approach used for shear-thinning fluids in Vázquez-Quesada *et al.* (2016)) may not be accurate for viscoplastic fluids. Instead, we suggest the use of sub-grid-scale lubrication force models based on viscoplastic lubrication theory, with the understanding that they may become invalid in regions without a macroscopic stress above the yield stress, i.e. where particles become confined by their own yield envelopes. This will allow for a large range of validity, for example in simulations of the type considered in Vázquez-Quesada *et al.* (2016); Bian & Ellero (2014) among others, where a dense suspension is subject to shear, and a sub-grid-scale lubrication force model is needed due to the close particle-particle approaches. However in other cases, for example dilute particulate suspensions sedimenting in a quiescent fluid, we have shown in this chapter that a sub-grid-scale lubrication force model based solely on lubrication theory in the gap may not be appropriate. Until a more sophisticated sub-grid-scale model is developed, the only current option is DNS computations with sufficiently high resolution in the inter-particle gaps.

In this chapter we have examined the viscoplastic squeeze flow between two infinite circular cylinders using an overset grid discretisation method and ALG2 solution approach. In the next chapter we extend this approach to larger suspensions, investigating the settling of particle suspensions in viscoplastic fluids.

7 Sedimentation of particle suspensions in a Bingham fluid

The dispersion of coarse particles in complex (shear dependent) fluids is an important aspect of both natural and industrial flows, for example, pyroclastic gravity currents (Dufek, 2016), proppant transport in hydraulic fracturing (Osiptsov, 2017), and fresh cement slurries. Often the suspended phase is (negatively) buoyant and its stability with respect to sedimentation during transport, or after flow cessation (Santos *et al.*, 2018), is of fundamental interest. Viscoplastic fluids, by virtue of a material yield stress, may support such a coarse particle phase indefinitely. This is governed by a balance between the stress exerted on the fluid by the particle and the fluid yield stress (Beris *et al.*, 1985), described by the non-dimensional yield number $Y = \hat{\tau}_y/(\hat{\rho}_p - \hat{\rho}_f)\hat{\boldsymbol{g}}\hat{l}'$, where $\hat{\boldsymbol{g}}$ is gravitational acceleration, $\hat{\rho}_p$ is the particle density, $\hat{\rho}_f$ the fluid density, $\hat{l}'$ a characteristic length scale, and $\hat{\tau}_y$ the material yield stress. Two aspects of buoyant particle transport in viscoplastic fluids stand out: the conditions for suspension stability, and the sedimentation behaviour. Both of these have been well characterised for single particles but not yet for suspensions, particularly under quiescent flow conditions.

With regards to stability, it has been shown that for an isolated particle there exists a critical yield number $Y = Y_0^*$ at which the buoyancy force exerted by the particle is balanced by the fluid yield stress. This has been the subject of many numerical and theoretical works (Tokpavi *et al.*, 2008; Beris *et al.*, 1985; Jossic & Magnin, 2001) and while there is great variability amongst experimental studies (Emady *et al.*, 2013; Chhabra, 2007), the theoretical Y_0^* for a spherical particle has been corroborated by Tabuteau *et al.* (2007). Given the non-linear rheology of the suspending fluid a key question is whether Y_0^* is applicable to suspensions. There has been some work, predominantly numerical and experimental, investigating model systems of two or more particles posed in the resistance sense—where flow is driven by a prescribed velocity—rather than the more applicable mobility sense—where flow is driven by applied force—due to the intrinsic numerical and practical difficulties of the latter. It was found that particles near each other, particularly in the inline configuration, experience a decreased drag force, from which it may be inferred that the same configuration would exhibit a higher critical yield number than an isolated particle (Tokpavi *et al.*, 2009; Liu *et al.*, 2003; Jie & Ke-Qin, 2006). The theoretical work of Frigaard *et al.* (2017) investigated this critical yield number for suspensions more directly through the out-of-plane flow of uniformly distributed particle suspensions with prescribed uniform suspension velocity. They inferred a volume fraction, ϕ, dependent critical yield number, Y_ϕ^*. However, the resistance formulation has clear drawbacks in that individual particle velocities are prescribed *a priori*. Recently, Chaparian *et al.* (2018) investigated inline particle configurations for up to 5 particles in the mobility sense, finding not only that their stability criterion is strongly influenced by separation distance but that particle chains are unlikely to be stable sedimentation configurations.

Settling of suspensions in viscoplastic fluids can be categorised as static settling or dynamic settling, depending on the background flow conditions (quiescent in the former). It is well known in the oil industry that background shear enhances settling (Childs *et al.*, 2016) in shear-thinning fluids. For viscoplastic fluids, Merkak *et al.* (2009) and Ovarlez *et al.* (2012) demonstrated shear-induced settling in fluids regardless of the yield number, showing that particles settle as soon as the fluid yield stress is overcome by macroscopic shear. The latter advocated a suspension settling function, in conjunction with a Newtonian hindering function, incorporating an effective viscosity based on the (applied) macroscopic shear rate. This framework has recently been adopted in a model for solids dispersion in hydraulic fracturing flows (Hormozi & Frigaard, 2017).

In quiescent background conditions, i.e. in the absence of applied macroscopic shear, a different approach is needed. Single particles settling in viscoplastic fluids under quiescent conditions have been investigated extensively in viscous and inertial regimes, both experimentally and numerically (Atapattu *et al.*, 1990; Yu & Wachs, 2007; Wilson *et al.*, 2003; Arabi & Sanders, 2016). Empirical terminal velocity models have been developed (Wilson *et al.*, 2003; Arabi & Sanders, 2016) and it has been suggested that these may be combined with Newtonian hindering functions in dispersion models such as Kaushal & Tomita (2013). However, studies on suspensions settling in viscoplastic fluids under quiescent conditions are very sparse (Khabazi *et al.*, 2016) so whether this is a viable approach is not clear.

In this chapter we present direct numerical simulations of non-colloidal particle suspensions, in the dilute limit, settling in quiescent viscoplastic fluids. Building on the out of plane investigation of (Frigaard *et al.*, 2017), we investigate the stability criterion as a function of solid volume fraction for the in plane flow and comment on the transition to settling—which, as far as we are aware, has not been investigated previously.

7.1 Mathematical formulation and solution

In contrast to Newtonian fluids, very little numerical work has been done on suspension sedimentation in viscoplastic fluids. Many successful strategies for large scale suspension simulation in Newtonian fluids (Brady, 1988) rely on superposition principles to make large scale computations tractable, which are not applicable to the non-linear viscoplastic system. Coarse-grain approaches for Newtonian fluids use lubrication force models as sub-grid-scale models for the under-resolved particle interactions. However, the authors recently found that such lubrication models cannot be straightforwardly applied in cases where particles are strongly confined in their yield envelopes such as may occur in sedimentation without imposed shear (Koblitz *et al.*, 2018*a*). This necessitates direct numerical simulation. We reduce the computational complexity by considering a quasi-static approximation, justified in the following dimensional analysis.

7.1.1 Dimensional analysis

Generally, the motion of a solid particle in a fluid is governed by

$$\left.\begin{aligned} &\hat{\rho}\left(\frac{\partial \hat{\boldsymbol{u}}}{\partial \hat{t}} + \hat{\boldsymbol{u}}\cdot\hat{\boldsymbol{\nabla}}\hat{\boldsymbol{u}}\right) = -\hat{\boldsymbol{\nabla}}\hat{p} + \hat{\boldsymbol{\nabla}}\cdot\hat{\boldsymbol{\tau}},\\ &\hat{\boldsymbol{\nabla}}\cdot\hat{\boldsymbol{u}} = 0,\\ &\hat{m}\frac{\mathrm{d}\hat{V}}{\mathrm{d}\hat{t}} = \hat{\boldsymbol{F}}, \end{aligned}\right\} \tag{7.1}$$

where $\hat{\rho}$ is the fluid density, $\hat{\boldsymbol{u}}$ the fluid velocity, $\hat{p}$ the pressure, $\hat{\boldsymbol{\tau}}$ the deviatoric stress tensor, $\hat{m}$ the particle mass (or moment of inertia), $\hat{V}$ the particle velocity (or angular velocity), and $\hat{\boldsymbol{F}}$ the total force (or torque) on the particle. For a generalised Newtonian fluid, the shear stress is linked to strain via

$$\hat{\boldsymbol{\tau}} = \hat{\eta}(\hat{\dot{\gamma}})\hat{\dot{\boldsymbol{\gamma}}}, \tag{7.2}$$

where $\hat{\eta}$ is an apparent viscosity. We limit ourselves to a fully yielded Bingham fluid for this dimensional analysis, such that

$$\hat{\boldsymbol{\tau}} = \left(\hat{\mu} + \frac{\hat{\tau}_y}{\hat{\dot{\gamma}}}\right)\hat{\dot{\boldsymbol{\gamma}}}, \tag{7.3}$$

where $\hat{\mu}$ is the plastic viscosity and $\hat{\tau}_y$ the yield stress. We choose the diameter of the particle, $\mathcal{L}$, as a characteristic length scale, along with a suitable velocity scale $\mathcal{U}$. Scaling time by $\mathcal{L}/\mathcal{U}$ and force by $\hat{\eta}\mathcal{U}\mathcal{L}$ eq. (7.1) can be made dimensionless

$$\left.\begin{aligned} &\mathrm{Re}\left(\frac{\partial \boldsymbol{u}}{\partial t} + \boldsymbol{u}\cdot\boldsymbol{\nabla}\boldsymbol{u}\right) = -\boldsymbol{\nabla}p + \boldsymbol{\nabla}\cdot\left(1 + \frac{\mathrm{Bn}}{\dot{\gamma}}\right)\dot{\boldsymbol{\gamma}},\\ &\boldsymbol{\nabla}\cdot\boldsymbol{u} = 0,\\ &\mathrm{Re}\left(\frac{\hat{m}}{\hat{\rho}\mathcal{L}^3\left(1+\frac{\mathrm{Bn}}{\dot{\gamma}}\right)}\right)\frac{\mathrm{d}V}{\mathrm{d}t} = \boldsymbol{F}, \end{aligned}\right\} \tag{7.4}$$

where the Reynolds number is $\mathrm{Re} = \hat{\rho}\mathcal{U}\mathcal{L}/\hat{\mu}$ and the Bingham number $\mathrm{Bn} = \hat{\tau}_y\mathcal{L}/\mathcal{U}\hat{\mu}$. If $\mathrm{Re} \to 0$ then we retrieve the viscoplastic Stokes equations

$$\boldsymbol{\nabla} p = \boldsymbol{\nabla}\cdot\left(1 + \frac{\mathrm{Bn}}{\dot{\gamma}}\right), \quad \boldsymbol{\nabla}\cdot\boldsymbol{u} = 0, \quad \boldsymbol{F} = 0, \tag{7.5}$$

which is the basis for the quasi-static approach (Feng & Joseph, 1995). However, This assumes that the unsteadiness is characterised by a time scale $\mathcal{T} \sim \mathcal{L}/\mathcal{U}$, which is not necessarily the case in particle suspensions. Here, unsteadiness arrises from particle–particle and particle–wall interactions. A common feature in such flows is the movement of solid bodies across undisturbed streamlines (Feng & Joseph, 1995). Following Feng & Joseph (1995), we assume that the lateral driving force on a particle is proportional to some characteristic velocity $\mathcal{U}$

$$\hat{f} \sim \hat{\eta}\mathcal{U}\mathcal{L}, \tag{7.6}$$

then the lateral acceleration is

$$\hat{f}/\hat{m} \sim \hat{\eta}\mathcal{U}\mathcal{L}/\hat{m}, \tag{7.7}$$

where $\hat{m}$ is the sum of mass and virtual mass of the particle. The time needed for a particle to move a lateral distance of $\mathcal{L}$ is

$$\mathcal{T} \sim \left(\frac{\mathcal{L}}{\hat{f}/\hat{m}}\right)^{\frac{1}{2}} = \left(\frac{\hat{m}}{\hat{\eta}\mathcal{U}}\right)^{\frac{1}{2}}. \tag{7.8}$$

Using this time scale in eq. (7.1) we find that the unsteady term is

$$\frac{\partial\hat{\boldsymbol{u}}}{\partial\hat{t}} = \frac{\mathcal{U}}{\mathcal{T}}\frac{\partial\boldsymbol{u}}{\partial t} = \mathcal{U}\left(\frac{\hat{\eta}\mathcal{U}}{\hat{m}}\right)^{\frac{1}{2}}\frac{\partial\boldsymbol{u}}{\partial t}, \tag{7.9}$$

such that the dimensionless governing equations are

$$\left.\begin{aligned}
&\left(\frac{\hat{\rho}\mathcal{L}^3}{\hat{m}}\right)^{1/2}\left(1+\frac{\mathrm{Bn}}{\dot{\gamma}}\right)^{1/2}\mathrm{Re}^{1/2}\,\frac{\partial \boldsymbol{u}}{\partial t} = -\boldsymbol{\nabla} p + \boldsymbol{\nabla}\cdot\left(1+\frac{\mathrm{Bn}}{\dot{\gamma}}\right)\dot{\boldsymbol{\gamma}}\\
&\boldsymbol{\nabla}\cdot\boldsymbol{u} = 0\\
&\mathrm{Re}^{1/2}\left(\frac{\hat{m}}{\hat{\mu}\left(1+\frac{\mathrm{Bn}}{\dot{\gamma}}\right)\mathcal{L}^3\hat{\rho}}\right)^{1/2}\frac{\mathrm{d}V}{\mathrm{d}t} = \boldsymbol{F},
\end{aligned}\right\} \tag{7.10}$$

where, as before, as $\mathrm{Re} \to 0$ both inertial terms are negligible. However, since the unsteady inertial term is $\mathrm{Re}^{-1/2}$ larger than the convective term, then for a particular Stokes approximation at a small but finite Reynolds number, the unsteady inertial term may be required (Feng & Joseph, 1995).

7.1.2 Problem statement and solution

We consider the steady approximation of inertia-less, rigid circular particles suspended in incompressible viscoplastic fluid from a mobility perspective. The particles are denoted by P; the particle boundaries by ∂P; and the entire domain (fluid and particle) by Ω; and the far field domain walls by $\partial\Omega$. The fluid has velocity $\hat{\mathbf{u}}(\hat{\boldsymbol{x}})$, pressure $\hat{p}(\hat{\boldsymbol{x}})$, plastic viscosity $\hat{\eta}$, and a total stress tensor $\hat{\boldsymbol{\tau}} - \hat{p}\boldsymbol{\delta}$, where variables with a hat are dimensional. In the absence of both fluid and particle inertia, and taking the particle buoyancy, $(\hat{\rho}_p - \hat{\rho}_f)\hat{g}\hat{l}'$, as a characteristic stress scale $\mathcal{T}$—where $\hat{\rho}_p$ and $\hat{\rho}_f$ are the particle and fluid densities, respectively, and $\hat{l}'$ is a characteristic length scale governed by the particle volume to frontal area ratio (Tokpavi *et al.*, 2009)—we solve the non-dimensional steady Stokes equations

$$\boldsymbol{\nabla}\cdot\boldsymbol{\tau} - \boldsymbol{\nabla} p = \frac{\rho_r}{1-\rho_r}\boldsymbol{e}_g,\ \text{in}\ \Omega\setminus P, \quad \boldsymbol{\nabla}\cdot\boldsymbol{u} = 0,\ \text{in}\ \Omega\setminus P \tag{7.11}$$

where $\boldsymbol{e}_g$ denotes the unit vector in the direction of gravity, $\rho_r = \hat{\rho}_f/\hat{\rho}_p$ and the particles are negatively buoyant, such that $\rho_r < 1$. We impose no-slip and no-penetration boundary conditions on the domain walls, such that

$$\boldsymbol{u} = 0 \text{ on } \partial\Omega, \tag{7.12}$$

and the fluid velocity is continuous with that of each particle, such that

$$\boldsymbol{u} \to \boldsymbol{U} + \boldsymbol{\omega} \times (\boldsymbol{x} - \boldsymbol{x}_b) \text{ on } \partial P, \tag{7.13}$$

where $\boldsymbol{U}$ and $\boldsymbol{\omega}$ are the *a priori* unknown linear and angular particle velocities, $\boldsymbol{x}$ is a point on ∂P, and $\boldsymbol{x}_b$ are the coordinates of the centre of mass of the particle. The particle translational and rotational velocities are determined by satisfying zero force and torque constraints on each particle, $\boldsymbol{F} = 0, \boldsymbol{T} = 0$. Here, $\boldsymbol{F}$ and $\boldsymbol{T}$ are defined for any given particle by

$$\boldsymbol{F} = \int_{\partial P} (-p\boldsymbol{n} + \boldsymbol{\tau}\cdot\boldsymbol{n})\,\mathrm{d}s + \boldsymbol{f}_b, \quad \boldsymbol{T} = \int_{\partial P} (\boldsymbol{x} - \boldsymbol{x}_b)\times(-p\boldsymbol{n} + \boldsymbol{\tau}\cdot\boldsymbol{n})\,\mathrm{d}s + \boldsymbol{t}_b, \tag{7.14}$$

where $\boldsymbol{n}$ is the unit normal vector to the body surface, and $\boldsymbol{f}_b$ and $\boldsymbol{t}_b$ are external body force and torque, respectively.

We close the system using the ideal Bingham constitutive law

$$\begin{cases} \tau = \left(1 + \dfrac{Y}{||\dot{\gamma}||}\right)\dot{\gamma} & \text{if } ||\tau|| > Y, \\ \dot{\gamma} = 0 & \text{if } ||\tau|| \leq Y, \end{cases} \tag{7.15}$$

where the rate of strain tensor is defined as $\dot{\boldsymbol{\gamma}} := (\nabla\boldsymbol{u} + \nabla\boldsymbol{u}^\intercal)$, and $||\cdot||$ is the induced norm of the Frobenius inner product:

$$\boldsymbol{a} : \boldsymbol{b} := \frac{1}{2}\sum_{ij} A_{ij}B_{ij}, \tag{7.16}$$

such that $||\dot{\gamma}|| = \sqrt{\dot{\boldsymbol{\gamma}} : \dot{\boldsymbol{\gamma}}}$. The force-free and torque-free conditions imply that the particles adjust their velocities and angular velocities instantaneously (Feng & Joseph, 1995).

Unless otherwise stated, we use $\mathcal{T}/\hat{\eta}\hat{\rho}_f$, $\mathcal{T}\hat{l}'/\hat{\eta}\hat{\rho}_f$, and $\hat{R}$ as characteristic strain $\mathcal{G}$, velocity $\mathcal{V}$, and length $\mathcal{L}$ scales, respectively, where $\hat{R}$ is the particle radius and $\hat{l}' = \pi\hat{R}/2$.

Lastly, we define the critical yield number at which motion for a suspension of volume fraction ϕ stops as Y^*_ϕ, where for a single particle we find $Y^*_0 = 0.084$, in agreement with the literature (Tokpavi *et al.*, 2008; Randolph & Houlsby, 1984; Chaparian *et al.*, 2018) (note that Chaparian *et al.* (2018) use a different length scale in their definition of Y).

We solve (7.11)–(7.15) using the widely adopted alternating direction multiplier method—also known as ALG2—developed by Glowinski (1984). It is extensively used in the literature, see Yu & Wachs (2007); Chaparian & Frigaard (2017); Muravleva (2015) and references therein, so we do not give details here. We follow the implementation of Olshanskii (2009); Muravleva & Olshanskii (2008).

Wachs & Frigaard (2016) studied the problem numerically for a single sedimenting particle in a Bingham fluid, with a particular focus on the critical yield stress required for cessation of motion. Even with a single particle in two dimensions with a relatively small mesh (61440 cells), their computations took around 12 hours (wall-time). The limiting problem is the high computational expense of the ALG2 algorithm typically used for viscoplastic flow problems; discussion of ALG2 and related algorithms can be found in Glowinski (2014). In order to make the larger problem sizes considered in this study tractable we adopt a steady approximation, as in (Chaparian *et al.*, 2018), and employ an overset grid discretisation strategy. Briefly, the overset grid method represents a complex domain using multiple body-fitted curvilinear grids that are allowed to overlap whilst being logically rectangular, see figure 7.1. The overlapping aspect brings flexibility and efficiency to grid generation, which is beneficial for complex domains and moving grid problems. Here, since the cylinders are static, the chief benefit of the overset grid methods is that the grids may be locally refined near the cylinder surfaces whilst keeping the grids logically rectangular. The grid generation procedure is discussed at length in (Chesshire & Henshaw, 1990; Henshaw, 1998), and has been used for Newtonian and viscoplastic particulate flow problems by the authors in (Koblitz *et al.*, 2017*b*, 2018*a*). The resultant linear system is inverted using the MUMPS massively parallel direct linear solver library (Amestoy *et al.*, 2001). Recently some significantly faster algorithms have been developed (Saramito, 2016; Treskatis *et al.*, 2016; Bleyer, 2018; Dimakopolous *et al.*, 2018), and so we expect a rapid expansion in the near future of the size of problem which can be attempted.

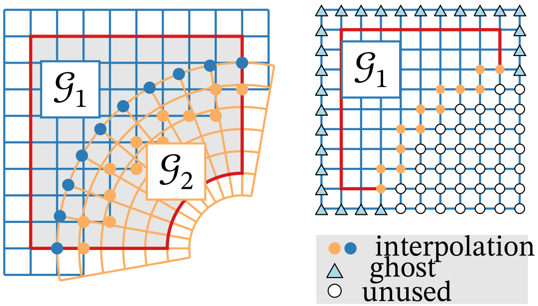

FIGURE 7.1: Left: an overlapping grid consisting of two structured curvilinear component grids, $\boldsymbol{x} = \mathcal{G}_1(\boldsymbol{r})$ and $\boldsymbol{x} = \mathcal{G}_2(\boldsymbol{r})$. Middle and right: component grids for the square and annular grids in the unit square parameter space $\boldsymbol{r}$. Grid points are classified as discretisation points, interpolation points or unused points. Ghost points are used to apply boundary conditions. The physical boundary is represented by the solid red line.

7.2 Results and discussion

We compute the instantaneous velocity field for pseudo-random configurations of infinite circular cylinders, of diameter D, in a confined domain with dimensions $(20\,D, 120\,D)$, for solid volume fractions $\phi = (0.01, 0.05)$ over a yield number range of $Y = (0, 0.173)$. Five pseudo-random configurations are used for each volume fraction.

Figure 7.2 shows the mean settling velocity of the suspension $\langle \hat{V}_{\phi,Y} \rangle$—normalised by the Stokes velocity of a single particle in a Newtonian fluid $\hat{V}_{0,0}$—averaged over all configurations, for increasing yield number. Here, the yield number is normalised using the critical yield number required to hold a single particle at rest, Y_0^*.

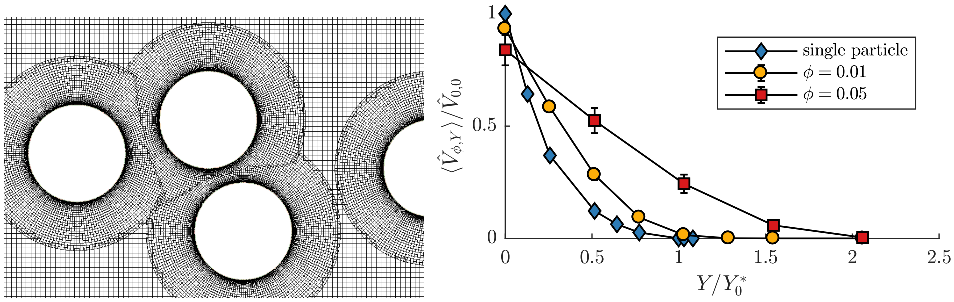

FIGURE 7.2: Left: Close-up view of a representative computational grid used, showing the overlapping particle and background grids and near-surface grid refinement. Right: Mean sedimentation velocity at increasing yield numbers for $\phi = (0, 0.01, 0.05)$, with error bars indicating the standard error of the mean particle sedimentation velocity.

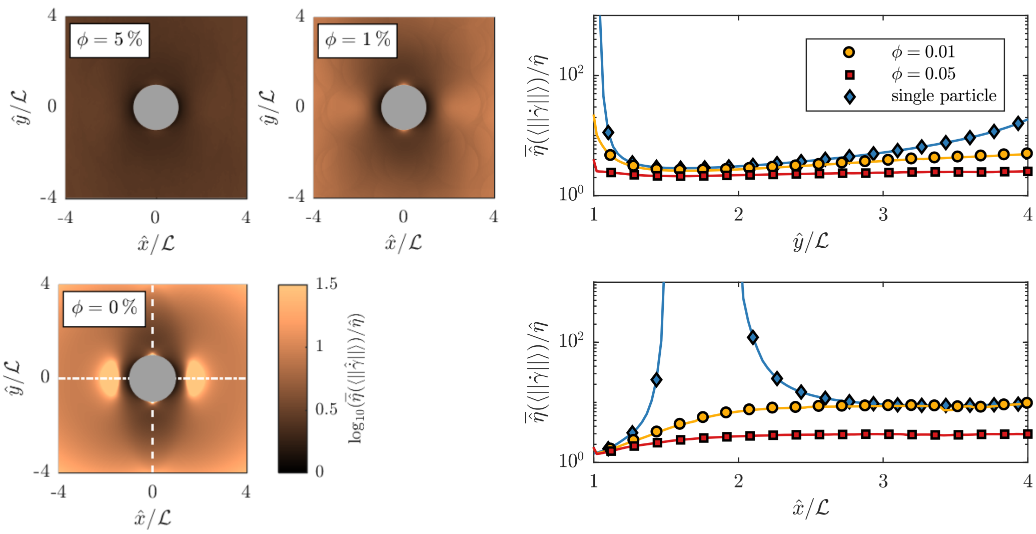

FIGURE 7.3: Left: Average effective viscosity near the particle surface for $Y = 0.043$, with longitudinal (dashed line) and lateral (dash-dot line) axes of symmetries indicated in the $\phi = 0$ panel. Right: average effective viscosity along the longitudinal (top) and lateral (bottom) axes of symmetry for $Y = 0.043$.

All volume fractions show a decrease in settling velocity as the yield number increases. This is expected from equation 7.15 where we can see that for any finite strain rate, a non-zero yield number leads to an increase in the effective viscosity. Looking at the limiting high yield number behaviour, we can see that the critical yield number required to hold the suspension at rest, Y^*_ϕ increases with the solid volume fraction, as was found in Frigaard *et al.* (2017) for out-of-plane settling. We find an approximately two-fold increase in the critical yield number for $\phi = 0.05$.

As $Y \to 0$ the medium mirrors a Newtonian fluid with viscosity $\hat{\eta}$, showing hindered settling with increased ϕ (Richardson & Zaki, 1954). However, for Y sufficiently large, we find higher settling efficiency with increasing solid volume fraction, indicated by the increased mean settling velocity. This is similar to what has been observed in experimental studies of settling suspensions in shear-thinning fluids (Moreira *et al.*, 2017). There, settling particles shear fluid, causing a local decrease in viscosity and thereby allowing nearby particles to settle more easily.

We investigate possible shear thinning by examining the average local viscosity in the vicinity of a particle at a given volume fraction at the same yield number, $Y = 0.043$, where all particles for all volume fractions are mobile. A rectangular grid is placed around each particle in the suspension on which $||\hat{\dot{\gamma}}||$ is found by means of bilinear interpolation. This is then averaged over all particles in the suspension, and used to find the average local effective viscosity, $\overline{\hat{\eta}}(\langle||\hat{\dot{\gamma}}||\rangle)$, where $\langle\cdot\rangle$ denotes an average over all particles. This is plotted as colourmaps in the left panel of figure 7.3. The viscosity field for the single particle is as expected: arbitrarily high viscosity peaks (truncated in the plot) at the unyielded equatorial plugs and the unyielded end-caps. As the volume fraction increases the viscosity field becomes more uniform and is found to decrease in magnitude. The viscosity along the two axes of symmetry shown in the $\phi = 0$ plot of figure 7.3 is further examined in the right panel of figure 7.3. The average viscosity decrease with increased solids volume fraction is evident, and the viscosity field is found to be, on average, uniform $\mathcal{L}$ away from the particle surface. Near the surface, the viscosity is high in the longitudinal direction due to the attached unyielded end-caps; however, in the lateral direction the viscosity is low near the surface due to the viscoplastic boundary layer.

It has been shown experimentally that static suspensions in yield stress fluids will settle when a macroscopic stress, for example by shearing the system, is introduced (Ovarlez *et al.*, 2012; Merkak *et al.*, 2009). In the absence of a macroscopic flow, only the buoyancy stress of the individual particles acts on the fluid to drive the flow. Studies of small systems of particles in the resistance formulation demonstrated a drag reduction for inline particle arrangements (Liu *et al.*, 2003; Yu & Wachs, 2007; Tokpavi *et al.*, 2009). Equivalently, the recent study of Chaparian *et al.* (2018) demonstrated higher velocities for inline configurations in the mobility formulation. The current simulations corroborate this in so far as structures of vertically clustered particles can clearly be visually identified to be settling fastest, for example, see the velocity magnitude colourmaps in figure 7.4. By examining the velocity field Chaparian *et al.* (2018) demonstrated that nearby particles had little effect on one another beyond a relatively small separation distance $\hat{d}_{\mathrm{sep}}/\mathcal{L} < 20$, suggesting that the stress decay in a viscoplastic fluid is appreciably faster than in a Newtonian fluid where $||\tau|| \sim r^{-1}$ as $r \to \infty$ (Tanner, 1993). As the yield number increases the rapid stress decay becomes more relevant. In the left panel of figure 7.5 the logarithmically-scaled colourmaps of the strain rate magnitude is shown for a configuration of $\phi = 0.01$, with the yield number increasing from left to right. As expected, unyielded material emerges as the yield number increases. For $Y \gtrsim 0.065$ discrete yield envelopes surround particles, coalescing into larger pockets when particles are close together. As the yield number increases further we find clusters of particles inside yield envelopes with comparatively isolated particles held static. For $\phi = 0.05$ we see a similar trend in the $\log_{10}(\dot{\gamma})$ colourmaps shown in the right panel of figure 7.5. However, there are fewer distinct groups of particles in individual yield envelopes. It is likely that the computational domain is not sufficiently large for a suspension this dense.

We take a closer look at the suspension morphology near Y_0^* in figure 7.4, where colourmaps of the velocity magnitude with yield surface overlays are shown for all five configurations for $\phi = 0.01$ (left panel) and $\phi = 0.05$ (right panel)

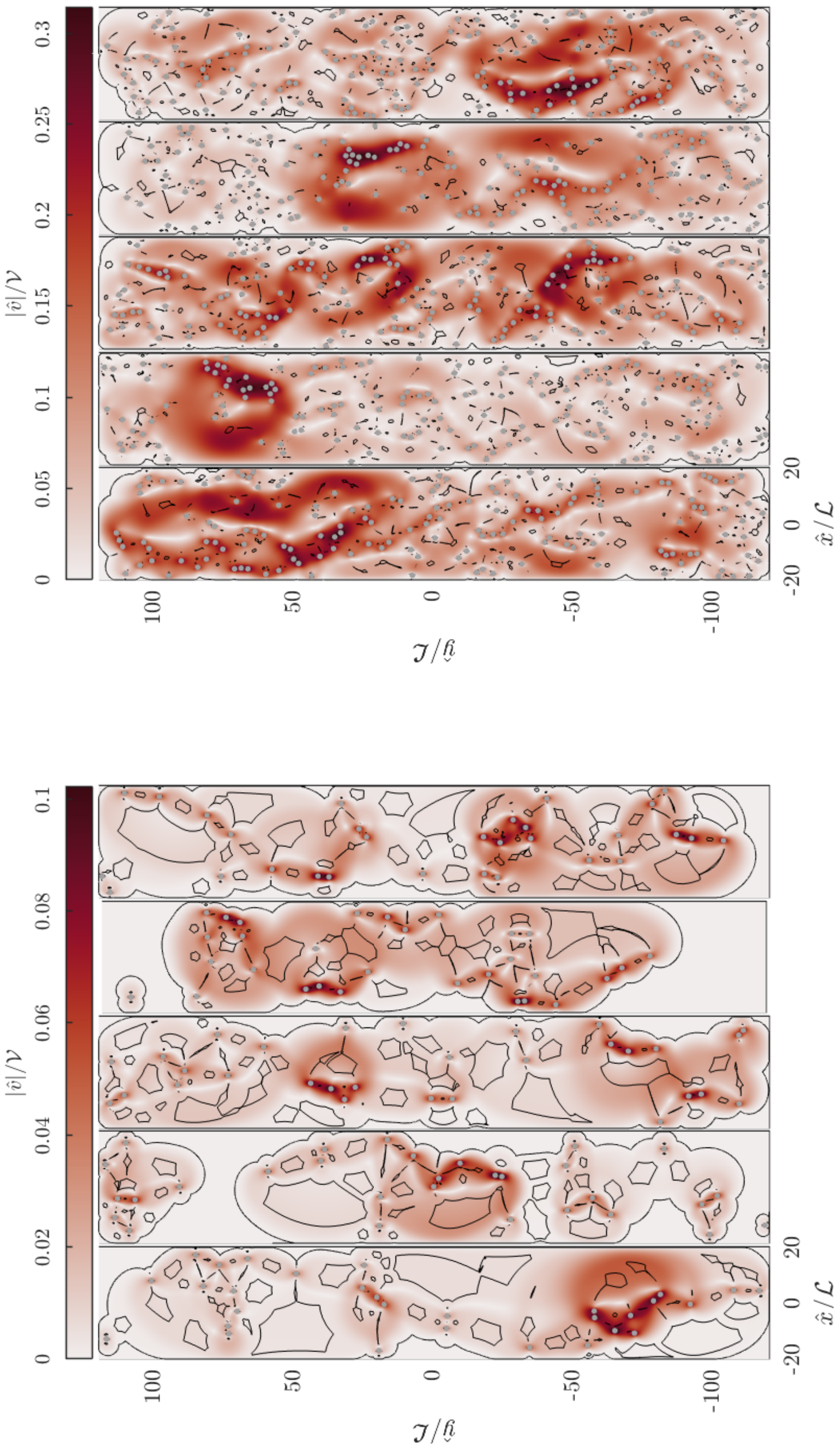

FIGURE 7.4: Colourmaps of the fluid velocity magnitude with particles overlaid in grey and yield surface indicated by the solid black lines for $Y = 0.087$ with $\phi = 0.01$ (left) and $\phi = 0.05$ (right) for five different configurations.

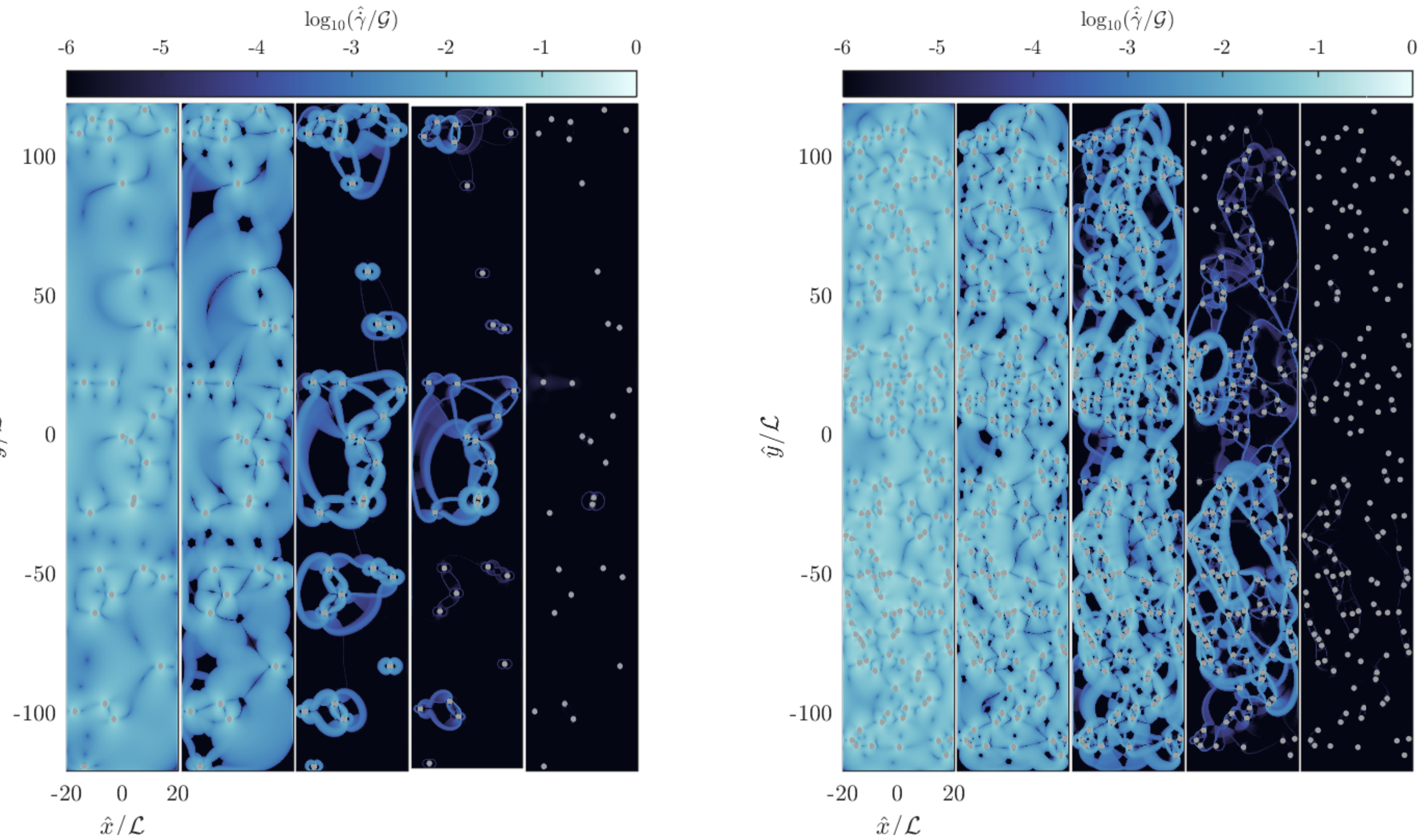

FIGURE 7.5: Colourmaps of $\log_{10}(\dot\gamma/\mathcal{G})$ for $\phi = 0.01$ at $Y = (0, 0.022, 0.065, 0.087, 0.13)$ (left panel) and $\phi = 0.05$ at $Y = (0, 0.043, 0.087, 0.13, 0.17)$ (right panel).

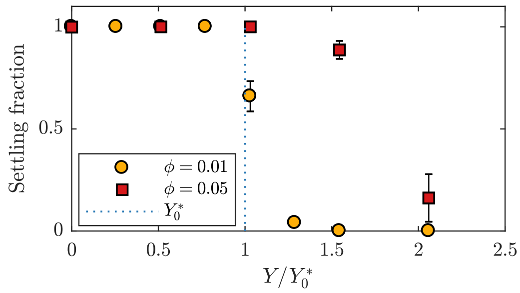

FIGURE 7.6: Proportion of settling particles in the suspension at increasing yield strengths with the critical yield number for a single particle indicated by the dashed line.

at $Y = 0.087$. All configurations for $\phi = 0.01$ show both static particles and yield pockets with sedimentation clusters, while for $\phi = 0.05$ no static particles are present in any configuration, and velocity peaks are found near vertically arranged clusters.

This formation of settling pockets of particle-dense regions and isolated static particles is not evident from the mean suspension velocity. In figure 7.6 we show the proportion of settling particles for both volume fractions as the yield number increases, averaged over all configurations. In both cases, for $Y/Y_0^* < 1$ the entire suspension settles as the yield number is below the threshold required to hold even a single particle static. At $Y/Y_0^* \approx 1$ the vast majority of the suspension settles for both cases, with a fraction of static particles evident for $\phi = 0.01$. As the yield number increases beyond $Y/Y_0^* = 1$ more isolated particles are held static, leading to a decrease in the settling fraction for both volume fractions considered. For $\phi = 0.01$ we find that the entire suspension is held static at $Y/Y_0^* \approx 1.5$. The critical yield number required to hold the entire $\phi = 0.05$ suspension static was not reached in this study due to convergence time requirements.

Concentrating on $\phi = 0.01$, for which we have found the critical yield number, we can see three distinct flow regimes: Regime (I) for $0 \leq Y < Y_0^*$ where the entire suspension is settling; Regime (II) for $Y_0^* \leq Y < Y_\phi^*$ where the proportion of static particles increases as $Y \rightarrow Y_\phi^*$; Regime (III) for $Y \geq Y_\phi^*$, for which the entire suspension is held stationary. While Y_ϕ^* was not reached for $\phi = 0.05$

in this study we have no reason to believe that the suspension will not be held static with a sufficiently high yield number. Experimental studies have worked with statically held suspensions as dense as $\phi = 0.4$ (Ovarlez *et al.*, 2012).

In regime (I) the fluid could be considered as weakly shear-thinning and regime (III) is trivial, while in regime (II) the strong competition between the yield stress and buoyancy of groups of particles leads to complex flow features, which the larger error bars above $Y/Y_0^* > 1$ in figure 7.6 indicate. Two examples of the complex flow features found in this regime are shown in figure 7.7. For each of the two features the left plots show colourmaps of the fluid velocity magnitude, while the right plots show colourmaps of the normalised second invariant of the velocity gradient tensor, Λ—a metric used to describe the character of the flow. Negative and positive values of Λ show where flow is dominated by enstrophy and strain, where for $\Lambda = -1$ flow is purely rotational, $\Lambda = 0$ flow undergoes simple shear, and $\Lambda = +1$ flow is purely extensional (Hemingway *et al.*, 2018). The left panel shows a sedimentation cluster in a $\phi = 0.01$ suspension mobilising a lone particle as it moves past. The right panel is from a $\phi = 0.05$ suspension showing a collection of particles settling together, generating a strong recirculating flow within the yield envelope. Lone particles are swept up by this recirculating flow, and two large unyielded plugs can be seen, one of which has embedded particles that would have otherwise been held static. It is flow features such as these that lead to the larger error bars in figure 7.6 but also complicate the identification of spatial correlation lengths, for example, critical separation distances between particles that encourage settling at yield numbers beyond Y_0^*.

Following the analysis of Putz & Frigaard (2010); Chaparian & Frigaard (2017); Roustaei *et al.* (2016) we examine global flow properties through the viscous dissipation, plastic dissipation and buoyancy work functionals, respectively:

$$a(\boldsymbol{v}, \boldsymbol{w}) = \int_{\Omega \backslash P} \dot{\boldsymbol{\gamma}}(\boldsymbol{v}) : \dot{\boldsymbol{\gamma}}(\boldsymbol{w}) \, \mathrm{d}A, \quad j(\boldsymbol{v}) = \int_{\Omega \backslash P} ||\dot{\boldsymbol{\gamma}}(\boldsymbol{v})|| \, \mathrm{d}A, \quad L(\boldsymbol{v}) = \pi \boldsymbol{V} \cdot \boldsymbol{e}_y, \tag{7.17}$$

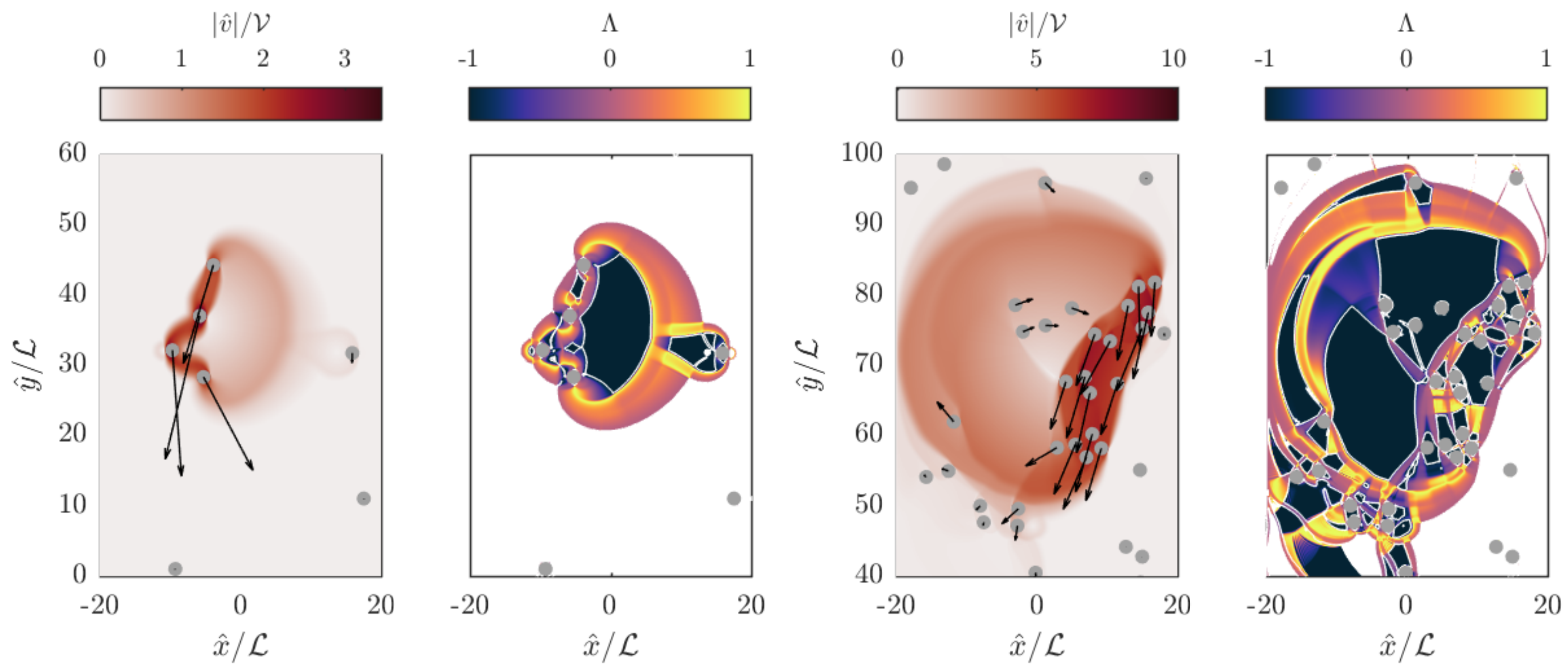

FIGURE 7.7: Examples of the complex flow features found in regime (II). Left: Close-up view from a $\phi = 0.01$ suspension with $Y = 0.087$ showing the mobilisation of an isolated particle by a passing sedimentation cluster. Right: Close-up view from a $\phi = 0.05$ suspension with $Y = 0.173$ showing lone particles swept up in the strong recirculating flow generated by a sedimentation cluster. A large unyielded region undergoing rigid body motion with embedded particles is visible. For each panel, the left plots show colourmaps of the fluid velocity magnitude, with particles overlaid in grey and their individual velocity vectors indicated by arrows. The right plots show colourmaps of the normalised second invariant of the velocity gradient tensor, with static unyielded regions masked off, yield surfaces indicated by the solid white lines, and particles overlaid in grey.

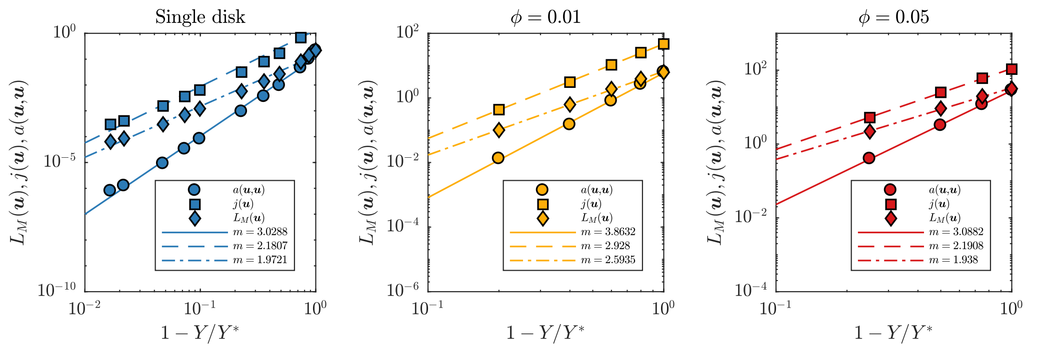

FIGURE 7.8: Convergence behaviour of the functionals $a(\boldsymbol{u},\boldsymbol{u})$ (circles), $j(\boldsymbol{u})$ (squares), and $L(\boldsymbol{u})$ (diamonds), for a single particle (blue), $\phi = 0.01$ (yellow), and $\phi = 0.05$ (red). Symbols are computed and lines are power-law fits with exponent m.

where $\boldsymbol{v}, \boldsymbol{w}$ are divergence free vector fields satisfying the boundary conditions (7.12) and (7.13), and $\boldsymbol{V}$ is a particle velocity vector. Exploring the static stability limit Putz & Frigaard (2010) observed that as $Y \to Y^{*-}$:

$$a(\boldsymbol{u},\boldsymbol{u}) \sim O([Y^* - Y]^2), \tag{7.18}$$

$$Y j(\boldsymbol{u}) \sim L(\boldsymbol{u}) \sim O(Y^* - Y), \tag{7.19}$$

where $O([Y^* - Y]^2)$ is a lower bound on the decay rate of the viscous dissipation (Roustaei *et al.*, 2016), but it always decays faster than the plastic dissipation (Putz & Frigaard, 2010). In the following analysis, we approximate the critical yield numbers for the suspensions as $Y^*_{0.01} \approx 1.5Y^*_0$ and $Y^*_{0.05} \approx 2Y^*_0$, respectively.

The panels of figure 7.8 show the convergence of the functionals for $\phi \in [0, 0.01, 0.05]$. For all volume fractions explored here, the viscous dissipation decays faster than $O([Y^* - Y]^2)$, the plastic dissipation approximately one order of magnitude slower and at a similar rate to the buoyancy work functional.

Defining the particle Bingham number as $B = \hat{\tau}_y \hat{L}/\hat{\mu}\hat{U}_p$, where $\hat{U}_p$ is a particle settling velocity, Chaparian & Frigaard (2017) linked the mobility and resistance formulation by rescaling variables by Y/B, showing that $Y \to Y^{*-}$ and $B \to \infty$ are the same limit and are coupled by

$$B \sim (1 - Y/Y^*)^{-\nu}, \tag{7.20}$$

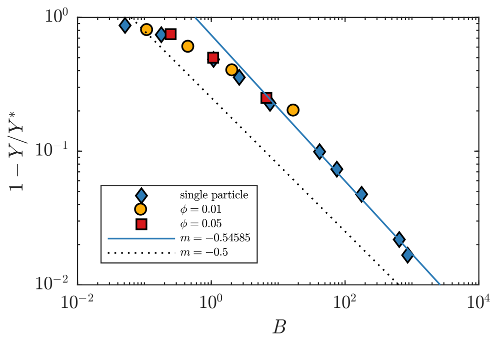

FIGURE 7.9: Convergence at large B for three volume fractions. Symbols are computed and lines are power-law fits with exponent m.

where ν is some positive exponent.

Using the mean suspension velocity (at a given volume fraction) to compute a $B(\phi)$ we show the convergence at large B in figure 7.9, along with a power-law fit to the single disk data. For the single disk, fitting the power-law to the markers for $1 - Y/Y^* < 0.5$ to limit ourselves to the behaviour near the yield limit Putz & Frigaard (2010), we recover $\nu \approx 2$, in line with previous results of Tokpavi *et al.* (2008) and Chaparian & Frigaard (2017). For the suspensions it is evident that we lack data sufficiently close to Y^*_ϕ to explore the behaviour near the yield limit. More computations near the yield limit are required for the suspensions. However, this is a far more computational demanding task than for single disks, as for single disks the resistance problem—which is significantly cheaper—may be evaluated at arbitrary velocities (see Chaparian & Frigaard (2017)) while for the suspensions we must evaluate the mobility problem. This, coupled with the necessarily increased problem size for the suspensions, makes further exploration of the near yield limit behaviour a computationally arduous task.

We can take a closer look at the energy dissipation in our system by examining the local viscous dissipation, Φ, in various flow structures by utilising the second invariant of the velocity gradient tensor, Λ, discussed previously. In figure 7.10 we show the viscous dissipation per unit volume as a function of the flow parameter Λ for a single disk and the suspensions. Defining a shear flow as $-1/3 \leq \Lambda \leq 1/3$ (De *et al.*, 2017), we can see that for a single disk most viscous

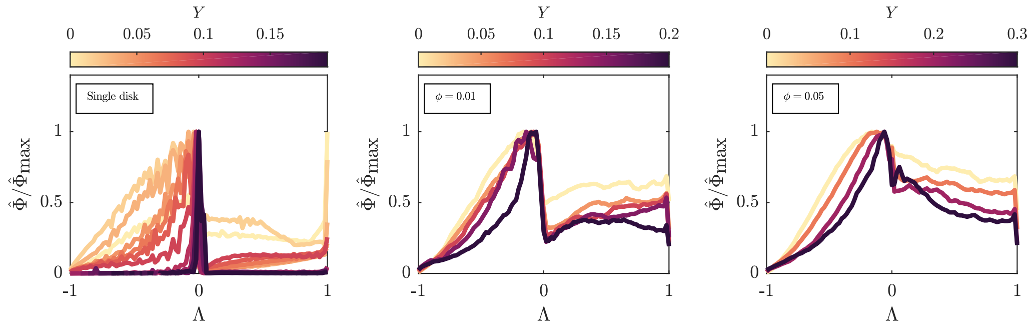

FIGURE 7.10: Normalised energy density per unit volume per unit Λ for a single disk (left), $\phi = 0.01$ (middle) and $\phi = 0.05$ (right).

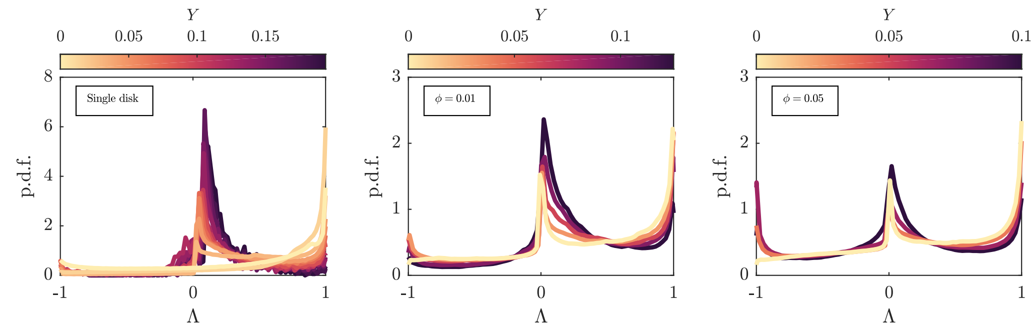

FIGURE 7.11: Probability density functions of Λ with increasing Y for a single disk (left), $\phi = 0.01$ (middle) and $\phi = 0.05$ (right).

dissipation is confined to shear layers, at all Y. For a single disk at low Y there is some contribution from extensional flow regions. However, as Y increases, the viscous dissipation becomes confined to shear layers, as is evidenced by the steepening in the left-hand side of the Φ peak near $\Lambda = 0$. For the two suspensions the viscous dissipation peaks in the shear layers, and the Φ peak steepens up as Y increases. However, unlike for the single disk, contributions to the viscous dissipation from extensional flow regions remain significant, particularly for $\phi = 0.05$.

In figure 7.11 we plot probability density functions of Λ. For the single disk, the flow is initially dominated by extensional flow. As Y increases, the particle becomes enclosed by a yield envelope, with shear layers developing on the envelope interface. This is reflected as a decrease in the extensional component, and the development of a peak near $\Lambda = 0$. Increasing the yield number further results in the growth of unyielded plugs on either side of the particle, with additional shear layers between the particle and plug, and plug and yield envelope wall, leading to a rapid decrease in extensional flow and a large peak near $\Lambda = 0$. We can see that for a single particle, the limiting flow, as $Y \to Y^{*-}$, is dominated by shear layers.

For the suspensions the trend is similar, with shear layers increasing while extensional flow decreases as Y increases. While we do not have enough data close enough to Y^*_ϕ to determine the limiting flow characteristics, the trend is certainly indicative of a shear dominated flow near Y^*_ϕ. In light of this, it is possible that with more data near Y^*_ϕ, the power-law behaviour in figure 7.9 should approach that of the single disk, ie $\nu \approx 2$, in line with other flows dominated by simple shear (Chaparian & Frigaard, 2017; Roustaei *et al.*, 2016; Frigaard & Scherzer, 2000).

7.3 Conclusions

In this chapter we investigated settling of two-dimensional non-colloidal particles in viscoplastic fluids under quiescent conditions by means of direct numerical simulation. Three flow regimes were identified, where (I) the entire suspension settles, (II) there exist both static and settling particles in the same suspension, and (III) the entire suspension is arrested.

In regime (I) for sufficiently high yield numbers we observe enhanced settling with increased volume fraction, opposite to a Newtonian fluid, which we attribute to shear-thinning. Regime (II) displays complex flow features such as sedimenting clusters, mobilisation of lone particles, and rigid recirculating zones. For suspension volume fractions greater than zero the transition to regime (III) is delayed, requiring a higher yield number to hold the suspension static than is required to hold a single particle static. This corroborates the theoretical work of Frigaard *et al.* (2017) and the inferences drawn from studies of small-scale model systems (Tokpavi *et al.*, 2009; Chaparian *et al.*, 2018).

Further research is required to explore the dynamics of the settling phases in regimes (I) and (II). Regime (II) is of particular interest since it may lead to heterogeneities in the suspension. Understanding this regime and the transition to regime (III) may play a role in explaining observations in many industrial and natural problems involving the sedimentation of viscoplastic suspensions under quiescent flow conditions. The immense computational requirements of the simulations (up to $10,000$ CPU hours for the most demanding ones) prevented the solutions from being marched forwards in time. We anticipate that new solution methods (Treskatis *et al.*, 2016; Bleyer, 2018; Saramito, 2016; Dimakopolous *et al.*, 2018) will soon enable much larger simulations of such systems, including the ability to investigate time-evolution and inertia, which were neglected in this study. Finally, we encourage researchers to investigate this problem experimentally.

8 Sheared neutrally buoyant particle suspensions in a Bingham fluid

Dense suspensions of solid particles are found in a broad range of applications, both in industrial processes (e.g. food processing) and natural phenomena (e.g. debris flows). Understanding the rheological behaviour of such suspensions is key to predicting how flows will behave in various applications. The rheological behaviour is further complicated by the range of particle sizes: small, colloidal particles may interact to give the bulk fluid a non-Newtonian, often viscoplastic, behaviour such that the larger, non-colloidal particles may be seen as a suspension in a complex fluid.

The theory of suspensions of particles in Newtonian fluids has a rich literature dating back to Einstein (Mueller *et al.*, 2010). However, much less work exists on suspensions of particles in complex fluids, in particular viscoplastic fluids. In recent years, there has been progress on modelling the bulk behaviour of viscoplastic suspensions from a continuum-level closure perspective. Chateau *et al.* (2008) utilised a homogenisation approach to develop a constitutive law for non-inertial, rigid particles suspended in a Herschel-Bulkley fluid, finding that the bulk suspension behaviour follows the interstitial power-law behaviour but with a volume fraction dependent consistency index and yield stress. Agreement with experimental results (Mahaut *et al.*, 2008; Ovarlez *et al.*, 2015) are generally good, however, suffer in the concentrated regime due to large experimental scatters (Dagois-Bohy *et al.*, 2015).

In a similar vein, continuum models of the so-called frictional type have been successful at describing non-colloidal suspensions in Newtonian media (Boyer *et al.*, 2011; Lecampion & Garagash, 2014). Recent experimental work on dense suspensions of particles in viscoplastic fluids has indicated that they may be described in a similar framework (Dagois-Bohy *et al.*, 2015) for solid volume fraction $\phi > 0.45$, showing good agreement with experimental studies in the concentrated regime up to the jamming transition.

Both the homogenisation and frictional approaches relate the imposed macroscopic shear rate, $\dot{\Gamma}$, to an average local shear rate, $\tilde{\dot{\gamma}}$, through some function $\mathcal{F}$ such that $\tilde{\dot{\gamma}} \propto \mathcal{F}\dot{\Gamma}$. Chateau *et al.* (2008) use an energy dissipation argument to derive this relation as a function of the volume fraction, $\mathcal{F}(\phi)$, while Dagois-Bohy *et al.* (2015) leave $\mathcal{F}(\phi)$ as an unknown function to be determined through an empirical fit. Dagois-Bohy *et al.* (2015) find good agreement between their empirical fit and Chateau *et al.* (2008), albeit with a coefficient of 2 that is not justified by the energy dissipation argument (Ovarlez *et al.*, 2015). Dagois-Bohy *et al.* (2015) find the frictional approach particularly suited to the concentrated regime but that as $\phi \to 0$ there is evidence of a more complex variation of $\mathcal{F}$ that needs to be further investigated.

Here, we present a numerical study of two-dimensional, non-colloidal suspensions of rigid particles in a viscoplastic Bingham fluid undergoing simple shear in the volume fraction range $\phi \in [0, 0.3]$. We utilise an overset grid discretisation, enabling sharp representation of surfaces and local grid refinement, allowing for fully resolved simulations with large particle counts. We investigate the homogenisation approach of Chateau *et al.* (2008) at increasing Bingham numbers, paying particular attention to the behaviour of the local shear rate. The simulations benefit the study of this aspect by providing access to the local values of the fluid velocity. We aim to improve the approximation of the average local shear rate by mapping the Bingham fluid to a Newtonian one via purely geometric effects to remain consistent with Dagois-Bohy *et al.* (2015). Inspired by the so-called shadow regions found in inertial suspensions in Newtonian fluids that lead to an excluded volume effect (Picano *et al.*, 2013), we find that unyielded material in the Bingham flows may be similarly interpreted as changes to the effective solid volume fraction, thereby allowing us to refine the homogenisation approach for such fluids.

8.1 Mathematical formulation and solution

We consider the steady approximation of inertia-less, neutrally buoyant, rigid circular particles suspended in incompressible viscoplastic fluid from a mobility perspective. The particles are denoted by P; the particle boundaries by ∂P; and the entire fluid domain (fluid and particle) by Ω; and the far field domain walls by $\partial\Omega$. The fluid has velocity $\mathbf{u}(\boldsymbol{x})$, the pressure $p(\boldsymbol{x})$, consistency index η, and a total stress tensor $\boldsymbol{\tau} - p\boldsymbol{\delta}$. We solve the non-dimensional steady Stokes equations

$$\boldsymbol{\nabla} \cdot \boldsymbol{\tau} - \boldsymbol{\nabla} p = \mathbf{0}, \quad \boldsymbol{\nabla} \cdot \boldsymbol{u} = 0 \text{ in } \Omega \setminus P. \tag{8.1}$$

We impose no-slip and no-penetration boundary conditions on the domain walls, such that

$$\boldsymbol{u} = 0 \text{ on } \partial\Omega, \tag{8.2}$$

and the fluid velocity is continuous with that of each particle, such that

$$\boldsymbol{u} \to \boldsymbol{U} + \boldsymbol{\omega} \times (\boldsymbol{x} - \boldsymbol{x}_b) \text{ on } \partial P, \tag{8.3}$$

where $\boldsymbol{U}$ and $\boldsymbol{\omega}$ are the *a priori* unknown linear and angular particle velocities, $\boldsymbol{x}$ is a point on ∂P, and $\boldsymbol{x}_b$ are the coordinates of the centre of mass of the particle. The particle translational and rotational velocities are determined by satisfying zero force and torque constraints on each particle, $\boldsymbol{F} = 0, \boldsymbol{T} = 0$. Here, $\boldsymbol{F}$ and $\boldsymbol{T}$ are defined for any given particle by

$$\boldsymbol{F} = \int_{\partial P} (-p\boldsymbol{n} + \boldsymbol{\tau} \cdot \boldsymbol{n})\, \mathrm{d}s + \boldsymbol{f}_b, \quad \boldsymbol{T} = \int_{\partial P} (\boldsymbol{x} - \boldsymbol{x}_b) \times (-p\boldsymbol{n} + \boldsymbol{\tau} \cdot \boldsymbol{n})\, \mathrm{d}s + \boldsymbol{t}_b, \tag{8.4}$$

where $\boldsymbol{n}$ is the unit normal vector to the body surface, and $\boldsymbol{f}_b$ and $\boldsymbol{t}_b$ are external body force and torque, respectively.

We close the system using the ideal Bingham constitutive law

$$\begin{cases} \tau = \left(\eta + \dfrac{\tau_y}{||\dot{\gamma}||}\right)\dot{\boldsymbol{\gamma}} & \text{if } ||\tau|| > Y, \\ \dot{\gamma} = 0 & \text{if } ||\tau|| \leq Y, \end{cases} \tag{8.5}$$

where the rate of strain tensor is defined as $\dot{\boldsymbol{\gamma}} := (\nabla \boldsymbol{u} + \nabla \boldsymbol{u}^{\intercal})$, and $||\cdot||$ is the induced norm of the Frobenius inner product:

$$\boldsymbol{a} : \boldsymbol{b} := \frac{1}{2}\sum_{ij} A_{ij}B_{ij}, \tag{8.6}$$

such that $||\dot{\gamma}|| = \sqrt{\dot{\boldsymbol{\gamma}} : \dot{\boldsymbol{\gamma}}}$. The force-free and torque-free conditions imply that the particles adjust their velocities and angular velocities instantaneously (Feng & Joseph, 1995). Unless stated otherwise, the wall velocity is used as a characteristic velocity scale, such that the Bingham number is a balance between the stress imposed at the walls and the material yield stress:

$$\text{Bn} := \frac{\tau_y}{\dot{\Gamma}}, \tag{8.7}$$

where $\dot{\Gamma}$ is the macroscopic shear rate.

For a suspension of particles in a Newtonian fluid of viscosity $\eta(0)$ in a simple shear flow of shear rate $\dot{\Gamma}$, the suspension is *a priori* characterised by stress components that vary linearly with $\dot{\Gamma}$

$$\tau = \mathrm{g}(\phi)\eta(0)\dot{\Gamma}, \tag{8.8}$$

where $g(\phi)$ is the Newtonian response, *eg* Krieger–Dougherty (Krieger & Dougherty, 1959). Assuming no energy dissipation from particle contacts, the density of energy, e, dissipated at the macroscopic and local scales may be matched. The local energy dissipation is:

$$e_{\text{local}} = (1-\phi)\langle \tau_{ij}^{\text{local}}(\boldsymbol{x})\dot{\gamma}_{ij}^{\text{local}}(\boldsymbol{x})\rangle = (1-\phi)\langle \eta(0)\dot{\gamma}_{\text{local}}^2(\boldsymbol{x})\rangle = (1-\phi)\eta(0)\tilde{\dot{\gamma}}_{\text{local}}^2(\boldsymbol{x}). \tag{8.9}$$

For a simple shear flow (with an isotropic interstitial fluid) the macroscopic energy dissipation is:

$$e_{\mathrm{global}} = \eta(0) g(\phi) \dot{\Gamma}^2. \tag{8.10}$$

Matching the local and macroscopic energy dissipation density we then recover the following estimate for the local strain rate:

$$\tilde{\dot{\gamma}} = \dot{\Gamma}\sqrt{\frac{g(\phi)}{1-\phi}}. \tag{8.11}$$

Under simple shear, the shear stress of our generalised Newtonian fluid is

$$\tau = \tilde{\eta}(\tilde{\dot{\gamma}})\dot{\Gamma}, \tag{8.12}$$

where $\tilde{\eta}$ is the effective viscosity of the interstitial fluid, dependent on the local shear rate:

$$\tilde{\eta}(\tilde{\dot{\gamma}}) = g(\phi)\left[\eta(0) + \frac{\tau_y(0)}{\tilde{\dot{\gamma}}}\right]. \tag{8.13}$$

Substituting (8.11) in to (8.13) we recover an effective viscosity function directly governed by the applied macroscopic shear rate:

$$\tilde{\eta}(\dot{\Gamma}, \phi) = g(\phi)\eta(0) + \frac{\tau_y(0)}{\dot{\Gamma}}\sqrt{(1-\phi)g(\phi)}. \tag{8.14}$$

In order to make the larger problem sizes considered in this study tractable we adopt a steady approximation, as in (Chaparian *et al.*, 2018), and employ an overset grid discretisation strategy. Briefly, the overset grid method represents a complex domain using multiple body-fitted curvilinear grids that are allowed to overlap whilst being logically rectangular, see figure 8.1. The overlapping aspect brings flexibility and efficiency to grid generation, which is beneficial for complex domains and moving grid problems. Here, since the cylinders are static, the chief benefit of the overset grid methods is that the grids may be locally refined near the cylinder surfaces whilst keeping the grids logically rectangular. The grid generation procedure is discussed at length in (Chesshire & Henshaw, 1990; Henshaw, 1998), and has been used for Newtonian and viscoplastic

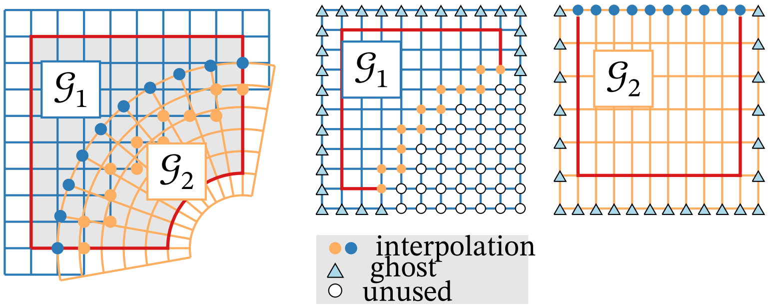

FIGURE 8.1: Left: an overlapping grid consisting of two structured curvilinear component grids, $\boldsymbol{x} = \mathcal{G}_1(\boldsymbol{r})$ and $\boldsymbol{x} = \mathcal{G}_2(\boldsymbol{r})$. Middle and right: component grids for the square and annular grids in the unit square parameter space $\boldsymbol{r}$. Grid points are classified as discretisation points, interpolation points or unused points. Ghost points are used to apply boundary conditions. The physical boundary is represented by the solid red line.

particulate flow problems by the authors in (Koblitz *et al.*, 2017*b*, 2018*a*). The resultant linear system is inverted using the MUMPS massively parallel direct linear solver library (Amestoy *et al.*, 2001). Recently some significantly faster algorithms have been developed (Saramito, 2016; Treskatis *et al.*, 2016; Bleyer, 2018; Dimakopolous *et al.*, 2018), and so we expect a rapid expansion in the near future of the size of problem which can be attempted.

8.2 Results and discussion

The homogenisation theory of Chateau *et al.* (2008); Ovarlez *et al.* (2015) agrees fairly well with experimental data from Mahaut *et al.* (2008), particularly at large solid volume fractions. However, there are gaps/regions where the validity of the theory (due to various assumptions, largely to do with isotropy) is in question. It has been conjectured that the isotropy assumption fails at high volume fractions due to both the non-linearity of the interstitial fluid, and the increasing importance of particle contacts. Ovarlez *et al.* (2015) showed that another assumption used in Chateau *et al.* (2008) and Dagois-Bohy *et al.* (2015), that of a self-similar microstructure at low and high shear rates, is not applicable to yield stress fluids. There is evidence that as $\phi \to 0$ there exists a more complex

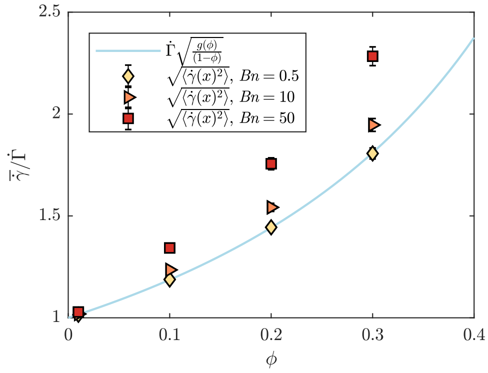

FIGURE 8.2: Comparison of local shear rate approximation (solid line) with computed root mean square values (markers).

variation in the local shear rate than previously taken in to account (Dagois-Bohy *et al.*, 2015).

In the following we use the Krieger-Dougherty equation as our Newtonian response,

$$g(\phi) = \left(1 - \frac{\phi}{\phi_{\max}}\right)^{-\phi_{\max}[\eta]}, \tag{8.15}$$

where $\phi_{\max}[\eta] = 1.82$ was used (Kromkamp *et al.*, 2006; Lee *et al.*, 2014) and the maximum packing fraction, $\phi_{\max} = 0.82$ was found using a least squares fit.

8.2.1 Local shear rate estimates

The local shear rate estimate is recovered for an isotropic fluid under simple shear. The Bingham fluid is non-linear, so how well does this approximation hold?

In figure 8.2 we compare the local shear rate estimate of (8.11) to the computed root mean square shear rates of our simulations. While the general trend is similar, *ie* $\tilde{\dot{\gamma}}$ increases with ϕ, it is clear the Bingham fluid has higher $\tilde{\dot{\gamma}}$ for volume fractions greater than $\phi = 0.01$. We explore this further by looking at the shear rate distributions in our domain. In figure 8.3 we show colour maps of $\log(\dot{\gamma}/\dot{\Gamma})$ (top row) for both a Newtonian (left panel) and Bingham (right panel) fluid. As expected, the Newtonian fluid has a fairly isotropic shear rate distribution. The

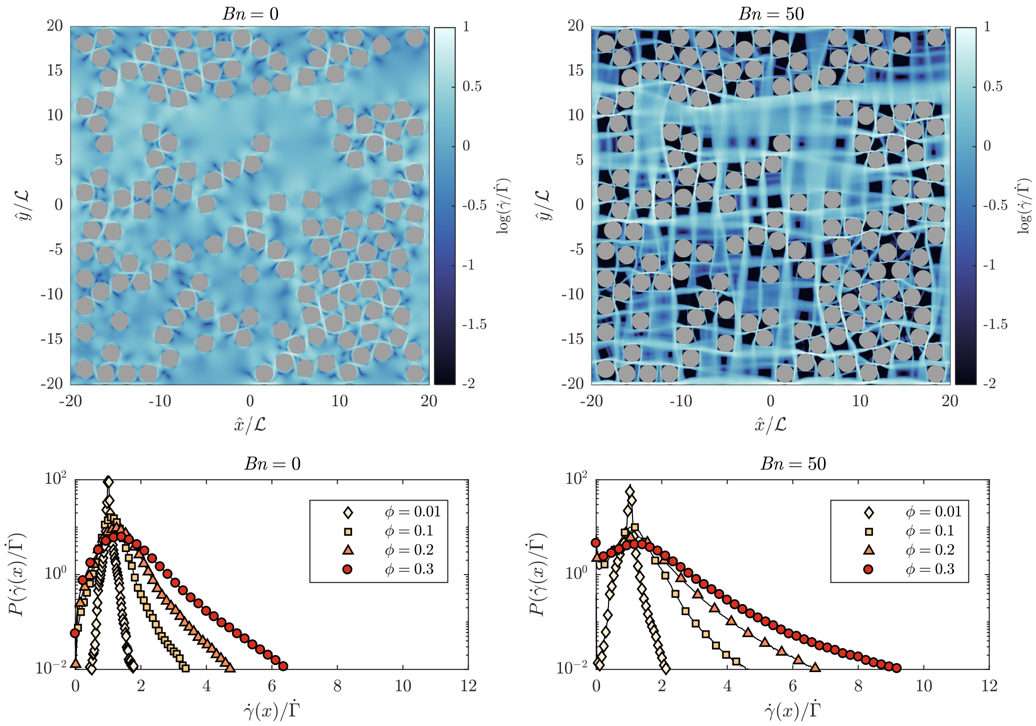

FIGURE 8.3: Top row: Colourmaps of $\log(\dot{\gamma}/\dot{\Gamma})$ for a $\phi = 0.3$ case, with a Newtonian interstitial fluid (left) and Bingham interstitial fluid (right). Bottom row: Probability density functions of the local shear rate for a Newtonian interstitial fluid (left) and Bingham interstitial fluid (right).

Bingham fluid shows significant local variations, with dead zones (pockets of low shear rate) and thin layers of high shear. In the bottom row are probability density function plots of $\dot{\gamma}/\dot{\Gamma}$ for both a Newtonian and Bingham fluid. At low volume fractions, the Newtonian fluid shows a near Gaussian shear rate distribution, peaking at $\dot{\gamma} = \dot{\Gamma}$. As the volume fraction increases, the distribution becomes positively skewed but the peak remains at $\dot{\gamma} = \dot{\Gamma}$ and $\dot{\gamma}(\boldsymbol{x}) > 0$. In contrast, the Bingham fluid shows non-negligible zero shear rate values. As the volume fraction increases, so does the zero shear rate contribution. While at low volume fractions there is a clear shear rate peak around $\dot{\gamma} = \dot{\Gamma}$, the peak quickly diminishes and the distribution becomes heavily positively skewed as the volume fraction increases.

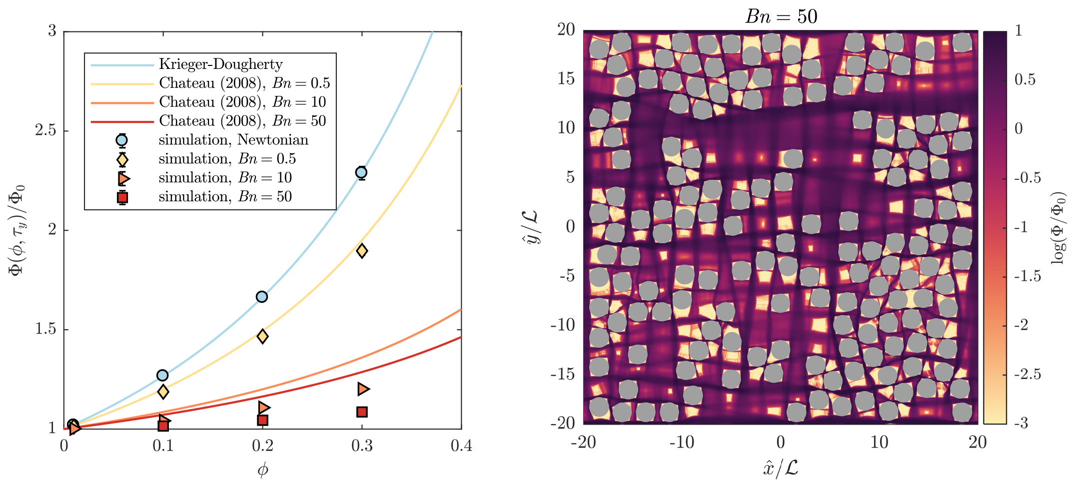

FIGURE 8.4: Left: Comparisons of computed (markers) and predicted viscous dissipation per unit volume (solid lines), showing consistent overestimation for $Bn > 0$. Right: Colourmap of $\log(\Phi/\Phi_0)$ showing the local dissipation density.

8.2.2 Suspension viscosity

In the left panel of figure 8.4 we plot the macroscopic viscous dissipation as predicted by the micromechanical model (solid lines), with overlaid markers showing the computed dissipation from the simulations. We find excellent agreement for the estimated and computed dissipation for the Newtonian fluid, however, for $Bn > 0$ the viscous dissipation is consistently overestimated for all $\phi > 0$. In the right panel we show a colourmap of the local dissipation density for a high volume fraction and yield stress case. It is evident that, much like the shear rate, the viscous dissipation is not isotropic; the dissipation in the dead zones identified earlier is very low, while dissipation is highest in the thin layers surrounding the dead zones and particles.

From the macroscopic viscous dissipation estimates in figure 8.4 it can be expected that the effective viscosity will be similarly overestimated by the micromechanical model and this is in fact the case, as may be seen in the left panel of figure 8.5. In the right panel of figure 8.5 we focus on the viscoplastic cases,

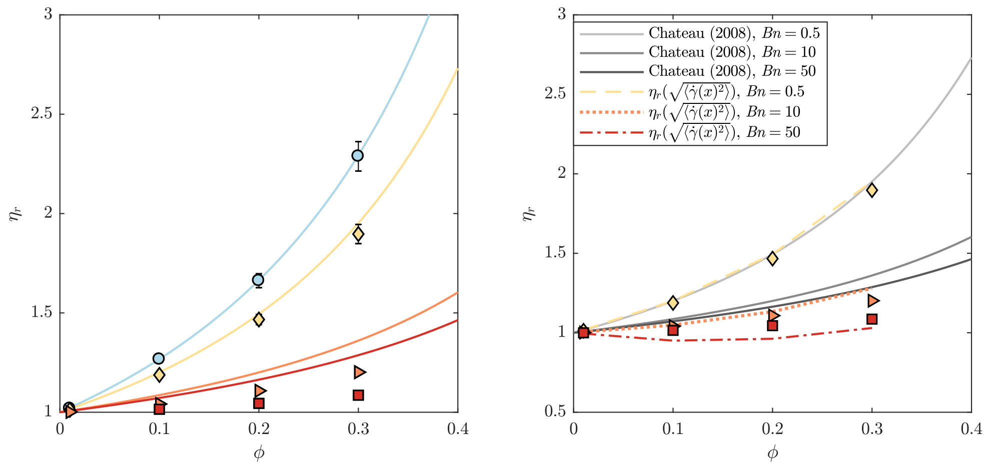

FIGURE 8.5: Left: Effective viscosity ratios predicted by the micromechanical model (solid lines) with simulation results overlaid. Right: Comparison of the effective viscosities computed using the micromechanical model with the computed root mean square shear rates (dotted lines) with the computed viscosities (markers) and the full micromechanical model estimate (solid lines).

again plotting the predictions of the micromechanical model (solid lines) and the computed viscosities (square and triangle markers). Additionally, we plot viscosity estimates computed using the micromechanical model but with computed root mean squared shear rates in lieu of (8.11). Using the computed root mean squared shear rate improves the effective viscosity estimates for all Bingham numbers tested, though agreement generally weakens as the Bingham number increases. This suggests that an accurate average local shear rate estimate may improve the micromechanical predictions, though at high Bingham numbers this may lead to under predictions.

8.2.3 Improved local shear rate estimate

In §8.1 we discussed the derivation of the average local shear rate based on a Newtonian energy balance, where the overriding assumptions are isotropy of the interstitial fluid, and a shear rate independent viscosity. To improve the shear rate estimate for Bingham fluids we wish to take the yield stress in to account, however, cannot explicitly incorporate the constitutive law if we wish to utilise this Newtonian energy balance. This is primarily because for us to find an approximate average local shear rate, the local viscosity and shear rate must be independent, see equation eq. (8.13).

In their work on inertial Newtonian suspension flows Picano *et al.* (2013) were able to demonstrate that shadow regions behind particles could be incorporated as an addition to the solid volume fraction, thereby improving the predictions based on a Stokes type model. Though the mechanisms are different, suspensions in Bingham fluids also display shadow regions, see figure 8.3 where unyielded material is found in the form of attached unyielded caps and rigidly rotating "deadzones", also visible as a peak at $\dot{\gamma}(x)/\dot{\Gamma} = 0$ in the probability density function in the bottom right panel of the same figure. The unyielded caps are common features in viscoplastic flows past blunt bodies, cf. (Koblitz *et al.*, 2018*b*; Tokpavi *et al.*, 2009; Beris *et al.*, 1985) amongst others. These are conceptually quite similar to the exclusion zones in the inertial Newtonian flows, however, whether the deadzones act as exclusion zones too is not immediately obvious.

We find that the deadzones are the result of overlapping Lagrangian blocking regions and vortical lobes. The blocking regions are common to flows past bluff bodies and are found in Newtonian systems as well (Camassa *et al.*, 2011). These blocking regions form fore and aft of the particles (in the shear direction) and have been shown to exist in three dimensional systems (Camassa *et al.*, 2011). The vortical lobes above and below the particles (with respect to the shear direction) are evident in Newtonian flows. However, in a Bingham fluid the vorticity magnitude is significant and their decay is slower than in a Newtonian fluid, leading to the elongated lobes seen in the right panel of figure 8.6. Knowing how these deadzones form we can set up minimal particle configurations to further examine their influence.

The left panel of figure 8.7 shows the basic particle arrangement necessary to create the disturbance velocity, ie the disturbance to the background flow caused by the presence of the particles. The deadzones can be seen to rotate and translate

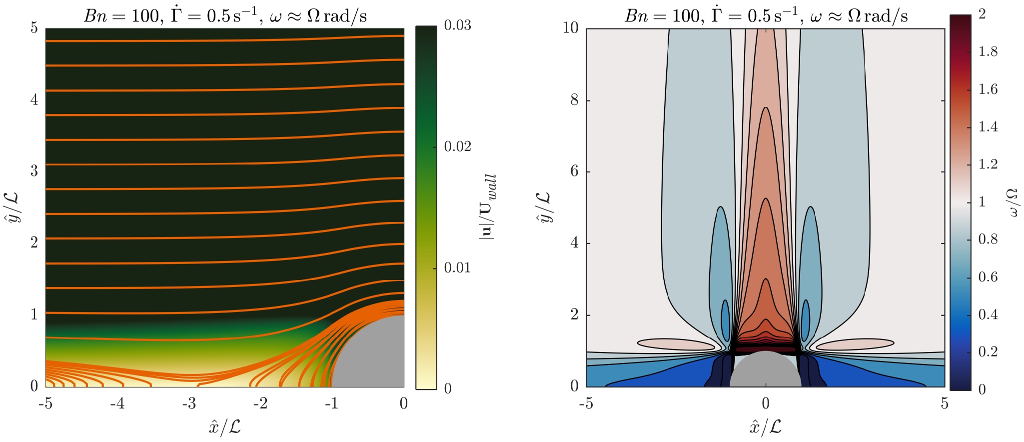

FIGURE 8.6: Left: Streamlines superimposed on a colourmap of the fluid velocity, normalised by the wall velocity, for a freely rotating particle centrally placed in a Couette cell. Right: Contour plot of the local vorticity normalised by the background vorticity, Ω, of the Couette cell.

with the background flow, imparting only a straining flow on the fluid, much like solid particles in non-inertial Newtonian suspension flows (Batchelor, 1967). This suggests that the deadzones may be considered in the same manner as rigid particles. This if further supported in figure 8.7, where the top right panel shows the colour map of the normalised second invariant of the disturbance velocity gradient corresponding to the particle arrangement in the left panel, while the bottom right panel shows the same metric for a four particle system arranged in a regular lattice structure. It is evident how closely the deadzone mimics a solid particle.

We now define an effective solid volume fraction $\tilde{\phi} = \phi + \phi_e$, where ϕ_e is the excluded volume fraction of the unyielded material (deadzones and caps) at a given Bingham number. We plot the computed root mean squared shear rate of our simulations against $\tilde{\phi}$ in the left panel of figure 8.8. The computed values can be seen to collapse reasonably well on to the universal curve provided by the Newtonian energy balance. This implies that we can reasonably accurately map the Bingham plastic flow to a Newtonian one by implicitly taking the yield stress

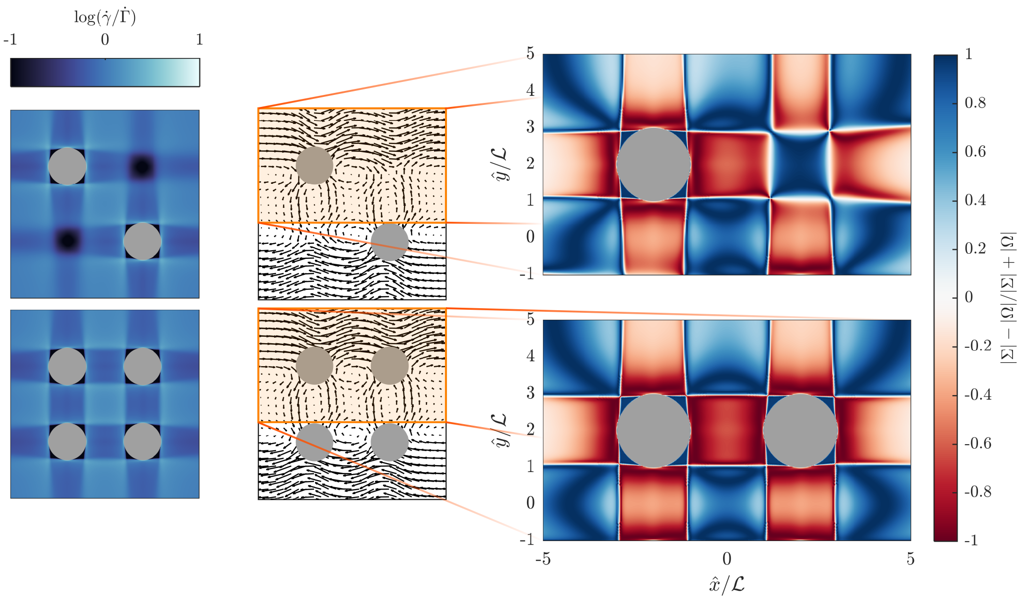

FIGURE 8.7: Left: Colourmaps of $\log(\dot{\gamma}/\dot{\Gamma})$ for the two particle system (top) with deadzones and yield caps visible, and four particle system (bottom) without deadzones, where in each case $Bn = 50$ and $\dot{\Gamma} = 0.1\,\mathrm{s}^{-1}$. Centre: vectors of the disturbance velocity field for the corresponding particle arrangements. Right: Zooms of the highlighted portions showing colour maps of the normalised second invariant of the disturbance velocity gradient tensor for a system displaying a deadzone (top panel) and one with the deadzone volume occupied by a particle (bottom panel).

effects in to account via the unyielded material volume fraction. This effective solid volume fraction may now be used in equation (8.11) such that

$$\tilde{\dot{\gamma}}_e = \dot{\Gamma}\sqrt{\frac{g(\phi_e)}{1-\phi_e}}, \tag{8.16}$$

to return an improved estimate of the average local shear rate, shown as the solid line in the left panel of figure 8.8.

Using this improved shear rate estimate we can now compute the effective viscosity as

$$\tilde{\eta}(\dot{\Gamma},\phi) = g(\phi)\left[\eta(0) + \frac{\tau_y(0)}{\dot{\Gamma}}\sqrt{\frac{1-\phi_e}{g(\phi_e)}}\right]. \tag{8.17}$$

The right panel of figure 8.8 shows the predictions of the homogenisation theory using the old (solid lines) shear rate model and the improved (broken lines) shear rate model, with computed results overlaid. We find that the improved shear rate model allows for a closer fit to the computed data, indicating that the geometric effects taken into account in the new shear rate model go some way towards addressing the mismatch with theory. Figure 8.9 shows how the effective volume fraction scales with the Bingham number. Though data is limited to $\phi < 0.4$, the effective volume fraction may be modelled in a similar fashion to Alghalibi *et al.* (2018)

$$\phi_e = 4.5 \times \mathrm{Bn}^{0.25}\,\phi^3\left(1-\frac{\phi}{\phi_{\max}}\right)^{0.5}. \tag{8.18}$$

However, simulations would have to be performed in three dimensions, spanning a greater volume fraction range in order to construct a model that may be used in practice. The current two dimensional simulations already push the viscoplastic solver to the limit, with simulations demanding up to 10 000 CPU hours (at high volume fraction and yield stress). Investigating such suspensions in three dimensions would require regularisation and coarse graining, where a sub grid scale lubrication force model as investigated in chapter 6 would be necessary.

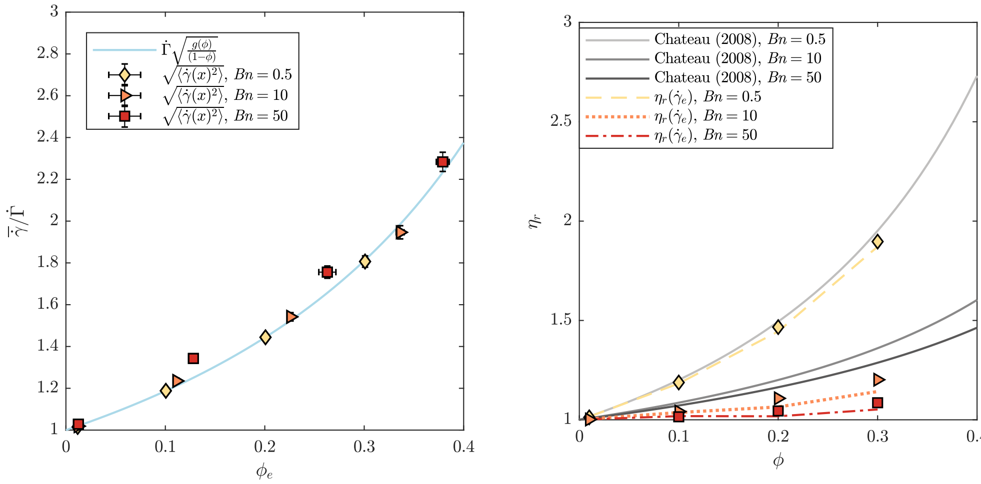

FIGURE 8.8: Left: local shear rate approximation (solid line) and computed root mean square values (markers) plotted against the effective solid volume fraction. Right: effective viscosity computed using the improved local shear rate estimate.

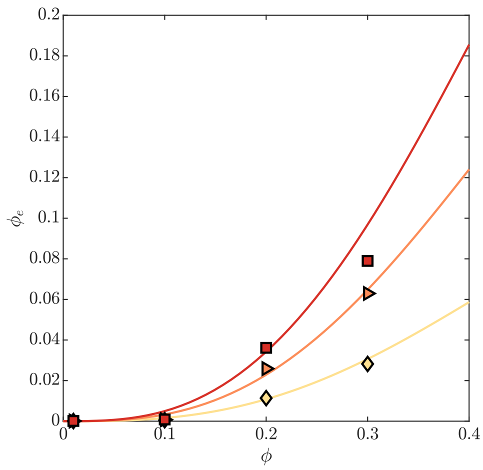

FIGURE 8.9: Effective solid volume fraction plotted against the particle volume fraction, where markers are the computed values and lines are predictions. Colours denote the Bingham number, as before.

8.3 Conclusions

In this chapter we presented direct numerical simulations of neutrally buoyant suspensions of infinite circular cylinders in Bingham fluids under simple shear. We investigated the micromechanical model of Chateau *et al.* (2008), derived from homogenisation theory, and found that at high Bingham number (equivalently, low macroscopic shear rate), the effective viscosity is over predicted owing to significant heterogeneities in the shear rate distribution. A central assumption of the homogenisation theory is that the carrier fluid be isotropic; at high Bingham number large areas remain unyielded, leading to deadzones that severely affect the average local shear rate approximation. By taking the unyielded material in to account, the system may be mapped on to an equivalent one with a solid volume fraction commensurate with the deadzones and particles, allowing for a more representative average local shear rate approximation. This in turn allows for better predictions of the effective viscosity with the otherwise unmodified micromechanical model of Chateau *et al.* (2008). However, two issues need to be addressed for this to be applied to real systems. Firstly, the calculations presented here were limited to two dimensions; though we expect the Lagrangian blocking regions to remain in the three dimensional case, since we know of their existence in the three dimensional Newtonian equivalent (Camassa *et al.*, 2011), the existence—and shape—of the vortical lobes in the three dimensional case is not self-evident. A relatively simple experimental setup of a single sphere placed centrally in a Couette flow of Carbopol may prove illuminating in this regard. Though Carbopol is not an ideal Bingham fluid due to slight elastic behaviour, the effect of this should not extend beyond asymmetries in the flow field for this case. Secondly, we require a function modelling the deadzone volume fraction with respect to Bingham number, similar to the excluded volume model of Alghalibi *et al.* (2018).

9 Conclusions and further work

In this work we aimed to better understand the rheology of particle-laden viscoplastic fluids, primarily motivated by the oil and gas industry but relevant to a host of others, by means of direct numerical simulation. While the non-linear carrier fluid and relatively large particle size make the problems difficult to investigate experimentally, intrinsic numerical issues make the problems difficult to tackle computationally as well. Below, we summarise the main findings of this work, and describe several directions for further work.

Overset grid method for fully resolved particulate flow simulation

To facilitate efficient gridding and accurate near-wall modelling we chose an overset grid methodology for the general fluid structure interaction aspect. In Chapter 5 we evaluated an efficient overset grid method for two-dimensional and three-dimensional particulate flows for small numbers of particles at finite Reynolds number. The rigid particles were discretised using moving curvilinear grids overlaid on a Cartesian background grid. This allowed for strongly-enforced boundary conditions and local grid refinement at particle surfaces, thereby accurately capturing the viscous boundary layer at modest computational cost.

The incompressible Navier–Stokes equations were solved with a fractional-step scheme which is second-order-accurate in space and time, while the fluid–solid coupling was achieved with a partitioned approach including multiple sub-iterations to increase stability for light, rigid bodies. Through a series of benchmark studies we demonstrated the accuracy and efficiency of this approach compared to other boundary conformal and static grid methods in the literature. In particular, we found that fully resolving boundary layers at particle surfaces is crucial to obtain accurate solutions to many common test cases. With this approach we were able to compute accurate solutions using as little as one third the number of grid points as uniform grid computations in the literature. A detailed convergence study showed a 13-fold decrease in CPU time over a uniform grid test case whilst maintaining comparable solution accuracy.

The collision model used here was a simple hard-sphere collision model based on linear conservation of momentum. An immediate improvement would be to incorporate angular conservation of momentum, to allow for frictional contacts. However, this hard-sphere collision model is rather limiting, particularly for multiple simultaneous particle contacts (e.g. in bed formation). The soft-sphere collision model of Kempe & Fröhlich (2012*b*) would be advantageous for future development.

On the applicability of viscoplastic lubrication theory to suspension flows

In Chapter 6 we presented direct numerical simulations of closely interacting infinite circular cylinders in a Bingham fluid, and compared results to asymptotic solutions based on lubrication theory in the gap. Unlike for a Newtonian fluid, the macroscopic flow outside of the gap between the cylinders was shown to have a large effect on the pressure profile within the gap and the resultant lubrication force on the cylinders. The presented results indicate that the asymptotic lubrication solution can be used to predict the lubrication pressure only if the surrounding viscoplastic matrix is yielded by a macroscopic flow. This has implications for the use of subgrid-scale lubrication models in simulations of non-colloidal particulate suspensions in viscoplastic fluids. This lubrication solution could be readily extended to the axisymmetric problem of two approaching spheres.

On the transition to yielding for negatively buoyant particle suspensions in yield stress materials

In Chapter 7 the settling efficiency, and stability with respect to settling, of a dilute suspension of infinite circular cylinders in an *a priori* quiescent viscoplastic fluid was investigated by means of direct numerical simulations with varying solid volume fraction, ϕ, and yield number, Y. For Y sufficiently large we found higher settling efficiency for increasing ϕ, similar to what is found in shear-thinning fluids and opposite to what is found in Newtonian fluids. The critical yield number at which the suspension is held stationary in the carrier fluid was found to increase monotonically with ϕ, while the transition to settling was found to be diffuse: in the same suspension, particle clusters may settle while more isolated particles remain arrested. In this regime, complex flow features are observed in the sedimenting suspension, including the mobilisation of lone particles by nearby sedimentation clusters. Understanding this regime, and the transition to a fully arrested state, is relevant to many industrial and natural problems involving the sedimentation of viscoplastic suspensions under quiescent flow, e.g. the suspension of microbeads in cement slurries, particularly in highly deviated drill pipe sections.

While exploring the coupling of the particle Bingham number B and suspension yield number Y it became evident that we lacked sufficient data for large B to definitively say whether the coupling of the two followed the same behaviour for a suspension as it does for a single body. This coupling is rather useful in that it allows for the estimation of a critical suspension yield number, without having to conduct experiments near the yield limit. Therefore, it would be advantageous to conduct further simulations closer to the yield limit.

An experimental study of this problem would be highly informative. The mixed settling regime, where isolated particles remain fixed but clusters settle, has yet to be investigate experimentally. Preliminary experiments at Schlumberger Cambridge Research using Carbopol-90 in square section cylinders and monodisperse bead suspensions showed similar settling behaviour.

On the rheology of neutrally buoyant particle suspensions in sheared yield stress materials

In Chapter 8 we presented a numerical study of two-dimensional, non-colloidal suspensions of rigid particles in a viscoplastic Bingham fluid undergoing simple shear in the volume fraction range $\phi \in [0, 0.3]$. We investigated the homogenisation approach of Chateau *et al.* (2008) at increasing Bingham numbers, finding that the local shear rate is significantly under estimated unless the Bingham number is small. Inspired by studies of weakly inertial suspensions in Newtonian fluids, we investigated the influence of regions of low deformation (so-called 'deadzones') on the average local shear rate. By taking the unyielded material in to account through a modified volume fraction, we showed that the system may be mapped on to an equivalent one with a volume fraction commensurate with the unyielded zones, thereby largely taking the non-linear effects of the fluid in to account. This allowed for improved average local shear rate estimates, improving the effective viscosity predictions of the otherwise micromechanical model of Chateau *et al.* (2008).

The formation of 'dead-zones' was attributed to the interaction of Lagrangian blocking regions and slowly decaying vortical lobes, both caused by the presence of the particles in the flow field. It is not clear how strongly this phenomenon is affected by the geometry, so a three-dimensional simulation of the two particle configuration would be telling.

Equally, this is something that could be investigated experimentally using a similar setup to Firouznia *et al.* (2018), who used a planar Couette-cell with particle image velocimetry and particle tracking velocimetry to investigate pair particle trajectories in simple-shear flows of yield stress fluids.

References

ABBAS, R., CUNNINGHAM, E., MUNK, T., BJELLAND, B., CHUKWUEKE, V., FERRI, A., GARRISON, G., HOLLIES, D., LABAT, C. & MOUSSA, O. 2002 Solutions for long-term zonal isolation. *Tech. Rep.*. Schlumberger.

ADACHI, K. & YOSHIOKA, N. 1973 On creeping flow of a visco-plastic fluid past a circular cylinder. *Chem. Eng. Sci.* **28**, 215–226.

ALGHALIBI, D., LASHGARI, I., BRANDT, L. & HORMOZI, S. 2018 Interface-resolved simulations of particle suspensions in Newtonian, shear thinning and shear thickening carrier fluids. *J. Fluid Mech.* **852**, 329–357q.

ALMGREN, A. S., BELL, J. B., COLELLA, P., HOWELL, L. H. & WELCOME, M. L. 1998 A conservative adaptive projection method for the variable density incompressible Navier–Stokes equations. *J. Comp. Phys.* **142**, 1–46.

AMESTOY, P. R., DUFF, I. S., L'EXCELLENT, J. & KOSTER, J. 2001 A fully asynchronous multifrontal solver using distributed dynamic scheduling. *SIAM J. Matrix Anal. Appl.* **32** (1), 15–41.

ANSLEY, R. W. & SMITH, T. N. 1967 Motion of spherical particles in a Bingham plastic. *AIChE* **13**, 1193–1196.

APOSPORIDIS, A., HABER, E., OLSHANSKII, M. A. & VENEZIANI, A. 2011 A mixed formulation of the Bingham fluid flow problem: analysis and numerical solution. *Comput. Methods Appl. Engrg.* **200**, 2434–2446.

ARABI, A. S. & SANDERS, R. S. 2016 Particle terminal settling velocities in non-Newtonian viscoplastic fluids. *Can. J. Chem. Eng.* **94**, 1092–1101.

ARDEKANI, A. M. & RANGEL, R. H. 2008 Numerical investigation of particle–particle and particle–wall collisions in a viscous fluid. *J. Fluid Mech.* **596**, 437–466.

ATAPATTU, D. D., CHHABRA, R. P. & UHLHERR, P. H. T. 1990 Wall effects for spheres falling at small Reynolds number in a viscoplastic medium. *J. Non-Newton. Fluid Mech.* **38**, 31–42.

ATAPATTU, D. D., CHHABRA, R. P. & UHLHERR, P. H. T. 1995 Creeping sphere motion in Herschel–Bulkley fluids: flow field and drag. *J. Non-Newton. Fluid* **59**, 245–265.

BAGCHI, P. 2007 Mesoscale simulation of blood flow in small vessels. *Biophys. J.* **92**, 1858–1877.

BALAY, S., BROWN, J., BUSCHELMAN, K., EIJKHOUT, V., GROPP, W. D., KAUSHIK, D., KNEPLEY, M. G., MCINNES, L. C., SMITH, B. F. & ZHANG, H. 2013 PETSc users manual. *Tech. Rep.*. Argonne National Laboratory.

BALMFORTH, N. J. 2017 Viscoplastic asymptotics and other techniques. In *Viscoplastic Fluids: From Theory to Application*. Springer.

BANFILL, P. F. G. 2006 Rheology of fresh cement and concrete. *Rheol. Rev.* pp. 61–130.

BANKS, J. W., HENSHAW, W. D., KAPILA, A. K. & SCHWENDEMAN, D. W. 2016 An added-mass partitioned algorithm for fluid-structure interactions of compressible fluids and nonlinear solids. *J. Comp. Phys.* **305**, 1037–1064.

BANKS, J. W., HENSHAW, W. D. & SCHWENDEMAN, D. W. 2012 Deforming composite grids for solving fluid structure problems. *J. Comp. Phys.* **231** (9), 3518–3547.

BANKS, J. W., HENSHAW, W. D. & SCHWENDEMAN, D. W. 2014*a* An analysis of a new stable partitioned algorithm for FSI problems. Part I: incompressible flow and elastic solids. *J. Comp. Phys.* **269**, 108–137.

BANKS, J. W., HENSHAW, W. D. & SCHWENDEMAN, D. W. 2014*b* An analysis of a new stable partitioned algorithm for FSI problems. Part II: Incompressible flow and structural shells. *J. Comp. Phys.* **268**, 399–416.

BANKS, J. W., HENSHAW, W. D. & SJÖGREEN, B. 2013 A stable FSI algorithm for light rigid bodies in compressible flow. *J. Comp. Phys.* **245**, 399–430.

BARNES, H. A. 1999 Yield stress—a review or '$\pi\alpha\nu\tau\alpha$ $\rho\epsilon\iota$'—everything flows? *J. Non-Newton. Fluid Mech.* **81**, 133–178.

BARNES, H. A. & WALTERS, K. 1985 The yield stress myth? *Rheol. Acta* **24**, 323–326.

BATCHELOR, G. K. 1967 *An introduction to fluid dynamics*. Cambridge University Press.

BECK, A. & TEBOULLE, M. 2009 A fast iterative shrinkage-thresholding algorithm for linear inverse problems. *SIAM J. Imaging Sci.* **2**, 183–202.

BEHR, M. & TEZDUYAR, T. E. 1994 Finite element strategies for large-scale flow simulations. *Comput. Methods Appl. Mech. Engrg.* **112**, 3–24.

BERCOVIER, M. & ENGELMAN, M. 1980 A finite-element method for incompressible non-Newtonian flows. *J. Comp. Phys.* **36**, 313–326.

BERIS, A. N., TSAMOPOULOS, J. H., ARMSTRONG, R. C. & BROWN, R. A. 1985 Creeping motion of a sphere through a Bingham plastic. *J. Fluid Mech.* **158**, 219–244.

BHALLA, A. P. S., BALE, R., GRIFFITH, B. E. & PATANKAR, N. 2013 A unified mathematical framework and an adaptive numerical method for fluid–structure interaction with rigid, deforming and elastic bodies. *J. Comp. Phys.* **250**, 446–476.

BIAN, X. & ELLERO, M. 2014 A splitting integration scheme for the SPH simulation of concentrated particle suspensions. *Comp. Phys. Comm.* **185**, 53–62.

BITTLESTON, S. 1991 Mud removal: Research improves traditional cementing guidelines. Technical report.

BLACKERLY, J. & MITSOULIS, E. 1997 Creeping motion of a sphere in tubes filled with a Bingham plastic material. *J. Non-Newton. Fluid Mech.* **70**, 59–77.

BLEYER, J. 2018 Advances in the simulation of viscoplastic fluid flows using interior-point methods. *Comput. Methods Appl. Mech. Engrg.* **330**, 368–394.

BONN, D., DENN, M. M., BERTHIER, L., DIVOUX, T. & MANNEVILLE, S. 2017 Yield stress materials in soft condensed matter. *Rev. Mod. Phys.* **89**, 035005.

BORAZJANI, I., GE, L. & SOTIROPOULOS, F. 2008 Curvilinear immersed boundary method for simulating fluid structure interaction with complex 3D rigid bodies. *J. Comp. Phys.* **227**, 7587–7620.

BOYER, F., GUAZZELLI, É. & POULIQUEN, O. 2011 Unifying suspension and granular rheology. *Phys. Rev. Lett.* **107**.

BRADY, J. F. 1988 Stokesian dynamics. *Annu. Rev. Fluid Mech.* **20**, 111–157.

BREUGEM, W.-P. 2012 A second-order accurate immersed boundary method for fully resolved simulations of particle-laden flows. *J. Comp. Phys.* **231** (13), 4469–4498.

BROERING, T.M., LIAN, Y & HENSHAW, W.D. 2012 Numerical investigation of energy extraction in a tandem flapping wing configuration. *AIAA Journal* **50** (11), 2295–2307.

BROWN, D. L., HENSHAW, W. D. & QUINLAN, D. J. 1999 Overture: Object-oriented tools for overset grid applications. *AIAA paper No. 99* **9130**, 245–255.

BROWN, E., MILNE, A. & THOMAS, R. 1990 The challenge of completing and stimulating horizontal wells.

CAMASSA, R., MCLAUGHLIN, R. M. & ZHAO, L. 2011 Lagrangian blocking in highly viscous shear flows past a sphere. *J. Fluid Mech.* **669**, 120–166.

TEN CATE, A., NIEUWSTAD, C. H., DERKSEN, J. J. & VAN DEN AKKER, H. E. A. 2002 Particle imaging velocimetry experiments and lattice-Boltzmann simulations on a single sphere settling under gravity. *Phys. Fluids* **11**.

CHAN, W. M. 2009 Overset grid technology development at NASA Ames Research Center. *Comput. Fluids* **38** (3), 496–503.

CHANDAR, D. D. J. & DAMODARAN, M. 2010 Numerical study of the free flight characteristics of a flapping wing in low Reynolds numbers. *J. Aircraft* **47** (1), 141–150.

CHAPARIAN, E. & FRIGAARD, I. A. 2017 Yield limit analysis of particles motion in a yield-stress fluid. *J. Fluid Mech.* **819**, 311–351.

CHAPARIAN, E., WACHS, A. & FRIGAARD, I. A. 2018 Inline motion and hydrodynamic interaction of 2D particles in a viscoplastic fluid. *Phys. Fluids* **30**, 033101–14.

CHATEAU, X., OVARLEZ, G. & TRUNG, K. L. 2008 Homogenization approach to the behavior of suspensions of noncolloidal particles in yield stress fluids. *J. Rheol.* **52**, 489.

CHESSHIRE, G. S. & HENSHAW, W. D. 1990 Composite overlapping meshes for the solution of partial differential equations. *J. Comp. Phys.* **90** (1), 1–64.

CHESSHIRE, G. S. & HENSHAW, W. D. 1994 A scheme for conservative interpolation on overlapping grids. *SIAM J. Sci. Comput.* **15** (4), 819–845.

CHHABRA, R. P. 2007 *Bubbles, drops, and particles in non-Newtonian fluids*, 2nd edn. Taylor & Francis.

CHILDS, L. H., HOGG, A. J. & PRITCHARD, D. 2016 Dynamic settling of particles in shear flows of shear-thinning fluids. *J. Non-Newton. Fluid Mech.* **238**, 158–169.

CODE OF FEDERAL REGULATIONS 2018 Underground injection control program: Criteria and standards. *Title 40, Part 146* .

COQUERELLE, M. & COTTET, G.-H. 2008 A vortex level set method for the two-way coupling of an incompressible fluid with colliding rigid bodies. *J. Comp. Phys.* **227** (21), 9121–9137.

COSTARELLI, S. D., GARELLI, L., CRUCHAGA, M. A., STORTI, M. A., AUSENSI, R. & IDELSOHN, S. R. 2016 An embedded strategy for the analysis of fluid structure interaction problems. *Comput. Method. Appl. M.* **300**, 106–128.

COUSSOT, P. 2014 Yield stress fluid flows: A review of experimental data. *J. Non-Newton. Fluid Mech.* **211**, 31–49.

DAGOIS-BOHY, S., HORMOZI, S., GUAZZELLI, E. & POULIQUEN, O. 2015 Rheology of dense suspensions of non-colloidal spheres in yield-stress fluids. *J. Fluid Mech.* **776**.

DAVIDSON, P. A. 2004 *Turbulence: An Introduction for Scientists and Engineers*. Oxford University Press.

DE, S., KUIPERS, J. A. M., PETERS, E. A. J. F. & PADDING, J. T. 2017 Viscoelastic flow simulations in model porous media. *Phys. Rev. Fluids* **2**.

DIMAKOPOLOUS, Y., MAKRIGIORGOS, G., GEORGIOU, G. C. & TSAMOPOULOS, J. 2018 The PAL (Penalized Augmented Lagrangian) method for computing viscoplastic flows: A new fast converging scheme. *J. Non-Newton. Fluid Mech.* **256**, 23–41.

DOUGHERTY, F. C. & KUAN, J.-H. 1989 Transonic store separation using a three-dimensional Chimera grid scheme. paper 89-0637. AIAA.

DUFEK, J. 2016 The fluid mechanics of pyroclastic density currents. *Annu. Rev. Fluid Mech.* **48**, 459–485.

DUVAUT, G. & LIONS, J. L. 1972 *Les inéquations en mécanique et en physique*. Dunod.

EMADY, H., CAGGIONI, M. & SPICER, P. 2013 Colloidal microstructure effects on particle sedimentation in yield stress fluids. *J. Rheol.* **57**, 1761–1772.

ENGLISH, R. E., QIU, L, YU, Y. & FEDKIW, R. 2013 An adaptive discretization of incompressible flow using a multitude of moving Cartesian grids. *J. Comp. Phys.* **254**, 107–154.

FADLUN, E. A., VERZICCO, R., ORLANDI, P. & MOHD-YUSOF, J. 2000 Combined immersed-boundary finite-difference methods for three-dimensional complex flow simulations. *J. Comp. Phys.* **161**, 35–60.

FALGOUT, R. D. & YANG, U. M. 2002 *hypre: a library of high performance preconditioners*. Springer Berlin Heidelberg.

FENG, J. & JOSEPH, D. D. 1995 The unsteady motion of solid bodies in creeping flows. *J. Fluid Mech.* **303**, 83–102.

FENG, Z.-G. & MICHAELIDES, E. E. 2004 The immersed boundary-lattice Boltzmann method for solving fluid–particles interaction problems. *J. Comp. Phys.* **195**, 602–628.

FERZIGER, J. H. & PERIĆ, M. 2002 *Computational methods for fluid dynamics*, 3rd edn. Springer.

FIROUZNIA, M., METZGER, B., OVARLEZ, G. & HORMOZI, S. 2018 The interaction of two spherical particles in simple-shear flows of yield stress fluids. *J. Non-Newton. Fluid Mech.* **255**, 19–38.

FORTES, A. F., JOSEPH, D. D. & LUNDGREN, T. S. 1987 Nonlinear mechanics of fluidization of beds of spherical particles. *J. Fluid Mech.* **177**, 467–483.

FRIGAARD, I. A., IGLESIAS, J. A., MERCIER, G., POŠCHL, C. & SCHERZER, O. 2017 Critical yield numbers of rigid particles settling in Bingham fluids and Cheeger sets. *SIAM J. Appl. Math.* **77** (2), 638–663.

FRIGAARD, I. A. & NOUAR, C. 2005 On the usage of viscosity regularisation methods for visco-plastic fluid flow computation. *J. Non-Newton. Fluid Mech.* **127**, 1–26.

FRIGAARD, I. A. & RYAN, D. P. 2004 Flow of a visco-plastic fluid in a channel of slowly varying width. *J. Non-Newton. Fluid Mech.* **123**, 67–83.

FRIGAARD, I. A. & SCHERZER, O. 2000 The effects of yield stress variation on uniaxial exchange flows of two Bingham fluids in a pipe. *SIAM J. Appl. Math.* **60**, 1950–1976.

GARTLING, D. K. & PHAN-THIEN, N. 1984 A numerical simulation of a plastic fluid in a parallel-plate plastometer. *J. Non-Newton. Fluid Mech.* **14**, 347–360.

GIBOU, F. & MIN, C. 2012 Efficient symmetric positive definite second-order accurate monolithic solver for fluid/solid interactions. *J. Comp. Phys.* **231** (8), 3246–3263.

GLOWINSKI, R. 1984 *Numerical methods for non-linear variational problems*. Springer Verlag.

GLOWINSKI, R. 2014 On alternating direction methods of multipliers: A historical perspective. *CMAS* **34**, 59–82.

GLOWINSKI, R., PAN, T. W., HESLA, T. I. & JOSEPH, D. D. 1999 A distributed Lagrange multiplier/fictitious domain method for particulate flows. *Int. J. Multiphas. Flow* **25**, 755–794.

GLOWINSKI, R., PAN, T.-W., HESLA, T. I., JOSEPH, D. D. & PÉRIAUX, J. 2000 A distributed Lagrange multiplier/fictitious domain method for the simulation of flow around moving rigid bodies: application to particulate flow. *Comput. Method. Appl. M.* **184** (2), 241–267.

GLOWINSKI, R., PAN, T. W., HESLA, T. I., JOSEPH, D. D. & PÉRIAUX, J. 2001 A fictitious domain approach to the direct numerical simulation of incompressible viscous flow past moving rigid bodies: Application to particulate flow. *J. Comp. Phys.* **169**, 363–426.

GOLDMAN, A. J., COX, R. G. & BRENNER, H. 1967 Slow viscous motion of a sphere parallel to a plane wall—motion through a quiescent fluid. *Chem. Eng. Sci.* **22**, 637–651.

HAERI, S. & SHRIMPTON, J. S. 2012 On the application of immersed boundary, ficticious domain and body-conformal mesh methods to many particle multiphase flows. *Int. J. Multiphas. Flow* **40**, 38–55.

HARLEN, O. G. 2002 The negative wake behind a sphere sedimenting through a viscoelastic fluid. *J. Non-Newton. Fluid Mech.* **108**, 411–430.

HEMINGWAY, E. J., CLARKE, A., PEARSON, J. R. A. & FIELDING, S. M. 2018 Thickening of viscoelastic flow in a model porous medium. *J. Non-Newton. Fluid Mech.* **251**, 56–68.

HENSHAW, W. D. 1994 A fourth-order accurate method for the incompressible Navier–Stokes equations on overlapping grids. *J. Comp. Phys.* **113**, 13–25.

HENSHAW, W. D. 1998 Ogen: an overlapping grid generator for Overture. Research Report UCRL-MA-132237. Lawrence Livermore National Laboratory.

HENSHAW, WILLIAM D. 2005 On multigrid for overlapping grids. *SIAM J. Sci. Comput.* **26** (5), 1547–1572.

HENSHAW, WILLIAM D. 2010 Cgins user guide: An Overture solver for the incompressible Navier-Stokes equations on composite overlapping grids. Software Manual LLNL-SM-455851. Lawrence Livermore National Laboratory.

HENSHAW, W. D. 2017 Private communication.

HENSHAW, WILLIAM D. & PETERSSON, N. ANDERS 2003 A split-step scheme for the incompressible Navier-Stokes equations. In *Numerical Simulation of Incompressible Flows* (ed. M. M. Hafez), pp. 108–125. World Scientific.

HENSHAW, WILLIAM D. & SCHWENDEMAN, DONALD W. 2006 Moving overlapping grids with adaptive mesh refinement for high-speed reactive and non-reactive flow. *J. Comp. Phys.* **216** (2), 744–779.

HORMOZI, S. & FRIGAARD, I. A. 2017 Dispersion of solids in fracturing flows of yield stress fluids. *J. Fluid Mech.* **830**, 93–137.

HORSLEY, M. R., HORSLEY, R. R., WILSON, K. C. & JONES, R. L. 2004 Non-Newtonian effects on fall velocities of pairs of vertically aligned spheres. *J. Non-Newton. Fluid Mech.* **124**, 147–152.

HU, H. H. 1996 Direct simulation of flows of solid–liquid mixtures. *Int. J. Multiphas. Flow* **22** (2), 335–352.

HU, H. H., PATANKAR, N. A. & ZHU, M. Y. 2001 Direct numerical simulations of fluid–solid systems using the arbitrary Lagrangian–Eulerian technique. *J. Comp. Phys.* **169**, 427–462.

HU, Y., LI, D., SHU, S. & NIU, X. 2015 Modified momentum exchange method for fluid–particle interactions in the lattice Boltzmann method. *Phys. Rev. E* **91**.

HUGHES, T. J. R., LIU, W. K. & ZIMMERMANN, T. K. 1981 Lagrangian–Eulerian finite element formulation for incompressible viscous flows. *Comput. Methods Appl. Mech. Engrg.* **29**, 329–349.

HUILGOL, R. R. 2002 Vartiational inequalities in the flows of yield stress fluids including inertia: theory and applications. *Phys. Fluids* **14**.

JIE, P. & KE-QIN, Z. 2006 Drag force of interacting coaxial spheres in viscoplastic fluids. *J. Non-Newton. Fluid Mech.* **135**, 83–91.

JOHNSON, A. & TEZDUYAR, T. 2001 Methods for 3D computation of fluid–object interactions in spatially periodic flows. *Comput. Methods Appl. Engrg.* **190**, 3201–3221.

JOHNSON, A. A. & TEZDUYAR, T. E. 1996 Simulation of multiple spheres falling in a liquid-filled tube. *Comput. Methods Appl. Mech. Engrg.* **134**, 351–373.

JOSEPH, D. D. & FENG, J. 1995 The negative wake in a second-order fluid. *J. Non-Newton. Fluid Mech.* **57**, 313–320.

JOSEPH, G. G., ZENIT, R., HUNT, M. L. & ROSENWINKEL, A. M. 2001 Particle–wall collisions in a viscous fluid. *J. Fluid Mech.* **433**, 329–346.

JOSSIC, L. & MAGNIN, A. 2001 Drag and stability of objects in a yield stress fluid. *AIChE* **47** (12), 2666–2672.

JOSSIC, L. & MAGNIN, A. 2009 Drag of an isolated cylinder and interactions between two cylinders in yield stress fluids. *J. Non-Newton. Fluid Mech.* **164**, 9–16.

KAJISHIMA, T. & TAKIGUCHI, S. 2002 Interaction between particle clusters and particle-induced turbulence. *Int. J. Heat Fluid Flow* **23** (5), 639–646.

KAUSHAL, D. R. & TOMITA, Y. 2013 Prediction of concentration distribution in pipeline flow of highly concentrated slurry. *Part. Sci. Tech.* **31**, 28–34.

KEMPE, T. & FRÖHLICH, J. 2012*a* Colision modelling for the interface-resolved simulation of spherical particles in viscous fluids. *J. Fluid Mech.* **709**, 445–489.

KEMPE, T. & FRÖHLICH, J. 2012*b* An improved immersed boundary method with direct forcing for the simulation of particle laden flows. *J. Comp. Phys.* **231**, 3663–3684.

KHABAZI, N. P., SADEGHY, K. & TAGHAVI, S. M. 2016 Simulating particle sedimentation in yield stress fluids. In *24th International Congress of Theoretical and Applied Mathematics*.

KIM, D. & CHOI, H. 2006 Immersed boundary method for flow around an arbitrarily moving body. *J. Comp. Phys.* **212**, 662–680.

KIM, Y. & PESKIN, C. S. 2016 A penalty immersed boundary method for a rigid body in fluid. *Phys. Fluids* **28** (3), 033603.

KOBLITZ, A.R., LOVETT, S., NIKIFORAKIS, N. & HENSHAW, W.D. 2017*a* Direct numerical simulation of particulate flows with an overset grid method. *ArXiv e-prints* , arXiv: 1702.01021.

KOBLITZ, A. R., LOVETT, S. & NIKIFORAKIS, N. 2018*a* Viscoplastic squeeze flow between two identical infinite circular cylinders. *Phys. Rev. Fluids* **3**, 023301–023315.

KOBLITZ, A. R., LOVETT, S., NIKIFORAKIS, N. & HENSHAW, W. D. 2017*b* Direct numerical simulation of particulate flows with an overset grid method. *J. Comp. Phys.* **343**, 414–431.

KOBLITZ, A. R., LOVETT, S. & NIKIFORAKISQ, N. 2018*b* Direct numerical simulation of particle sedimentation in a Bingham fluid. *Phys. Rev. Fluids* .

KRIEGER, I.M. & DOUGHERTY, T.J. 1959 A mechanism for non-Newtonian flow in suspensions of rigid spheres. *T. Soc. Rheol.* **3**, 137–152.

KROMKAMP, J., VAN DEN ENDE, D., KANDHAI, D., VAN DER SMAN, R. & BOOM, R. 2006 Lattice Boltzmann simulation of 2D and 3D non-Brownian suspensions in Couette flow. *Chem. Eng. Sci.* **61**, 858–873.

KUSHCH, V. I., SANGANI, A. S., SPELT, P. D. M. & KOCH, D. L. 2002 Finite-Weber-number motion of bubbles through a nearly inviscid liquid. *J. Fluid Mech.* **460**, 241–280.

KÜTTLER, ULRICH & WALL, WOLFGANG A. 2008 Fixed-point fluid–structure interaction solvers with dynamic relaxation. *Computational Mechanics* **43** (1), 61–72.

LĀCIS, U.S, TAIRA, K. & BAGHERI, S. 2016 A stable fluid–structure-interaction solver for low-density rigid bodies using the immersed boundary projection method. *J. Comp. Phys.* **305**, 300–318.

LANI, ANDREA, SJÖGREEN, BJÖRN, YEE, H. C. & HENSHAW, WILLIAM D. 2012 Variable high-order multiblock overlapping grid methods for mixed steady and unsteady multiscale viscous flows, part II: hypersonic nonequilibrium flows. *Commun. Comp. Phys.* **13** (2), 583–602.

LECAMPION, B. & GARAGASH, D. I. 2014 Confined flow suspensions modelled by a frictional rheology. *J. Fluid Mech.* **759**, 197–235.

LEE, T.-R., CHANG, Y.-S., CHOI, J.-B., KIM, D. W., LIU, W. K. & KIM, Y.-J. 2008 Immersed finite element method for rigid body motions in the incompressible Navier–Stokes flow. *Comput. Method. Appl. M.* **197** (25), 2305–2316.

LEE, Y. K., AHN, K. H. & LEE, S. J. 2014 Local shear stress and its correlation with local volume fraction in concentrated non-Brownian suspensions: Lattice Boltzmann simulation. *Phys. Rev. E* **90**, 062317.

Li, Longfei, Henshaw, William D., Banks, Jeffrey W., Schwendeman, Donald W. & Main, Geoffrey A. 2016 A stable partitioned FSI algorithm for incompressible flow and deforming beams. *J. Comp. Phys.* **312**, 272–306.

Lipscomb, G. G. & Denn, M. M. 1984 Flow of Bingham fluids in complex geometries. *J. Non-Newton. Fluid Mech.* **14**, 337–346.

Liu, B. T., Muller, S. J. & Denn, M. M. 2003 Interactions of two rigid spheres translating collinearly in creeping flow in a Bingham material. *J. Non-Newton. Fluid Mech.* **113**, 49–67.

Liu, Y. J., Nelson, J., Feng, J. & Joseph, D. D. 1993 Anomalous rolling of spheres down an inclined plane. *J. Non-Newton. Fluid Mech.* **50**, 305–329.

Luo, H., Dai, H., Ferreira de Sousa, P. J. S. A. & Yin, B. 2012 On the numerical oscillation of the direct-forcing immersed-boundary method for moving boundaries. *Comput. Fluids* **56**, 61–76.

Luo, K., Wang, Z., Fan, J. & Cen, K. 2007 Full-scale solutions to particle-laden flows: Multidirect forcing and immersed boundary method. *Phys. Rev. E* **76**.

Mahaut, F., Chateau, X., Coussot, P. & Ovarlez, G. 2008 Yield stress and elastic modulus of suspensions of noncolloidal particles in yield stress fluids. *J. Rheol.* **52**, 287–313.

Malekmohammadi, S., Carrasco-Teja, M., Storey, S., Frigaard, I. A. & Martinez, D. M. 2010 An experimental study of laminar displacement flows in narrow vertical eccentric annuli. *J. Fluid Mech.* **649**, 371–398.

Meakin, R. 1993 Moving body overset grid methods for complete aircraft tiltrotor simulations. paper 93-3350. AIAA.

Merkak, O., Jossic, L. & Magnin, A. 2006 Spheres and interactions between spheres moving at very low velocities in a yield stress fluid. *J. Non-Newton.Fluid.* **133**, 99–108.

MERKAK, O., JOSSIC, L. & MAGNIN, A. 2009 Migration and sedimentation of spherical particles in a yield stress fluid flowing in a horizontal cylindrical pipe. *AIChE* **55** (10), 2515–2525.

MITSOULIS, E. 2004 On creeping drag flow of a viscoplastic fluid past a circular cylinder: wall effects. *Chem. Eng. Sci.* **59**, 789–800.

MITTAL, R. & ICCARINO, G. 2005 Immersed boundary methods. *Annu. Rev. Fluid Mech.* **37**, 239–261.

MOHD-YUSOF, J. 1997 Combined immersed-boundary/B-spline methods for simulations of flow in complex geometries. *Center for Turbulence Research Annual Research Briefs* .

MØLLER, P. C. F., FALL, A. & BONN, D. 2009 Origin of apparent viscosity in yield stress fluids below yielding. *EPL* **87**.

MOREIRA, B. A., DE OLIVEIRA AROUCA, F. & DAMASCENO, J. J. R. 2017 Analysis of suspension sedimentation in fluids with rehological shear-thinning properties and thixotropic effects. *Powder Tech.* **308**, 290–297.

MOSSAZ, S., JAY, P. & MAGNIN, A. 2010 Criteria for the appearance of recirculating and non-stationary regimes behind in a viscoplastic fluid. *J. Non-Newton. Fluid Mech.* **165**, 1525–1535.

MUELLER, S., LLEWELLIN, E. W. & MADER, H. M. 2010 The rheology of suspensions of solid particles. *Proc. R. Soc. A* **466**, 1201–1228.

MURAVLEVA 2017 Axisymmetric squeeze flow of a viscoplastic Bingham medium. *J. Non-Newton. Fluid Mech.* **249**, 97–120.

MURAVLEVA, E. A. & OLSHANSKII, M. A. 2008 Two finite-difference schemes for calculation of Bingham fluid flows in a cavity. *Russ. J. Numer. Anal. Math. Modelling* **23** (6), 615–634.

MURAVLEVA, L. 2015 Squeeze plane flow of viscoplastic Bingham material. *J. Non-Newton. Fluid Mech.* **220**, 148–161.

NELSON, E. B. 1990 *Well cementing*. Elsevier.

NELSON, E. B. & GUILLOT, D. 2006 *Well cementing*, 2nd edn. Schlumberger.

NESTEROV, Y. 1983 A method of solving a convex programming problem with convergence rate $o(1/k^2)$. *Soviet Math. Doklady* **27**, 372–376.

NICOLLE, A. 2010 Flow through and around groups of bodies. PhD thesis, University College London.

NICOLLE, A. & EAMES, I. 2011 Numerical study of flow through and around a circular array of cylinders. *J. Fluid Mech.* **679**, 1–31.

NIRMALKAR, N., CHHABRA, R. P. & POOLE, R. J. 2012 On creeping flow of a Bingham plastic fluid past a square cylinder. *J. Non-Newton. Fluid Mech.* **171–172**, 17–30.

NIU, X. D., SHU, C., CHEW, Y. T. & PENG, Y. 2006 A momentum exchange-based immersed boundary-lattice Boltzmann method for simulating incompressible viscous flows. *Phys. Lett. A* **354**, 173–182.

OLSHANSKII, M A. 2009 Analysis of semi-staggered finite-difference method with application to Bingham flows. *Comput. Methods Appl. Mech. Engrg.* **198**, 975–985.

OSIPTSOV, A. A. 2017 Fluid mechanics of hydraulic fracturing: a review. *J. Petrol. Sci. Eng.* **156**, 513–535.

OVARLEZ, G., BERTRAND, F., COUSSOT, P. & CHATEAU, X. 2012 Shear-induced sedimentation in yield stress fluids. *J. Non-Newton. Fluid Mech.* **177–178**, 19–28.

OVARLEZ, G., MAHAUT, F., DEBOEUF, S., LENOIR, N., HORMOZI, S. & CHATEAU, X. 2015 Flows of suspensions of particles in yield stress fluids. *J. Rheol.* **59**, 1449–1486.

PAPANASTASIOU, T. C. 1987 Flows of materials with yield. *J. Rheol.* **31**, 385–404.

PATANKAR, N. A. 2001 A formulation for fast computations of rigid particulate flows. *Center for Turbulence Research* .

PATANKAR, N. A., SINGH, P., JOSEPH, D. D., GLOWINSKI, R. & PAN, T.-W. 2000 A new formulation of the distributed Lagrange multiplier/fictitious domain method for particulate flows. *Int. J. Multiphas. Flow* **26**, 1509–1524.

PATANKAR, S. V. & SPALDING, D. B. 1972 A calculation procedure for heat, mass and momentum transfer in three-dimensional parabolic flows. *Int. J. Heat Mass Transfer* **15**, 1787–1806.

PESKIN, C. S. 1972 Flow patterns around heart valves: a numerical method. *J. Comp. Phys.* **10**, 252–271.

PETERSSON, N. A. 2001 Stability of pressure boundary conditions for Stokes and Navier–Stokes equations. *J. Comp. Phys.* **172**, 40–70.

PIAU, J.-M. 2002 Viscoplastic boundary layer. *J. Non-Newton. Fluid Mech.* **102**, 193–218.

PIAU, J.-M. & DEBIANE, K. 2004 The adhesive or slipperly flat plate viscoplastic boundary layer for a shear-thinning power-law viscosity. *J. Non-Newton. Fluid Mech.* **117**, 97–107.

PICANO, F., BREUGEM, W.-P., MITRA, D. & BRANDT, L. 2013 Shear thickening in non-Brownian suspensions: an excluded volume effect. *Phys. Rev. Lett.* **111**, 098302–1–098302–5.

PRAGER, W. 1952 On slow visco-plastic flow. *Tech. Rep.*. Brown University.

PRASHANT, J. J. D. 2011 Direct simulations of spherial particle motion in Bingham liquids. *Comput. Chem. Eng.* **35**, 1200–1214.

PUTZ, A. & FRIGAARD, I. A. 2010 Creeping flow around particles in a Bingham fluid. *J. Non-Newton. Fluid Mech.* **165**, 263–280.

PUTZ, A., FRIGAARD, I. A. & MARTINEZ, D. M. 2009 On the lubrication paradox and the use of regularisation methods for lubrication flows. *J. Non-Newton. Fluid Mech.* **163**, 62–77.

PUTZ, A. M. V., BURGHELEA, T. I., FRIGAARD, I. A. & MARTINEZ, D. M. 2008 Settling of an isolated spherical particle in a yield stress shear thinning fluid. *Phys. Fluids* **20**.

QIU, L., YU, Y. & FEDKIW, R. 2015 On thin gaps between rigid bodies two-way coupled to incompressible flow. *J. Comp. Phys.* **292**, 1–29.

RANDOLPH, M. F. & HOULSBY, G. T. 1984 The limiting pressure on a circular pile loaded laterally in cohesive soil. *Geotechnique* **34**, 613–623.

RICHARDSON, J. F. & ZAKI, W. N. 1954 Sedimentation and fluidisation. Part 1. *Trans. Inst. Chem. Eng.* **32**, 35–53.

ROUSTAEI, A., CHEVALIER, T., TALON, L. & FRIGAARD, I. A. 2016 Non-Darcy effects in fracture flows of a yield stress fluid. *J. Fluid Mech.* **805**, 222–261.

ROUSTAEI, A., GOSSELIN, A. & FRIGAARD, I. A. 2015 Residual drilling mud during conditioning of uneven boreholes in primary cementing. part 1: Rheology and geometry effects in non-inertial flows. *J. Non-Newton. Fluid Mech.* **220**, 87–98.

SANGANI, A. S. & DIDWANIA, A. K. 1993 Dynamic simulations of flows of bubbly liquids at large Reynolds numbers. *J. Fluid Mech.* **250**, 307–337.

SANTOS, N. B. C., FAGUNDES, F. M., DE OLIVEIRA AROUCA, F. & DAMASCENO, J. J. R. 2018 Sedimentation of solids in drilling fluids used in oil well drilling operations. *J. Petrol. Sci. Eng* **162**, 137–142.

SARAMITO, P. 2016 A damped Newton algorithm for computing viscoplastic fluid flows. *J. Non-Newton. Fluid Mech.* **238**, 6–15.

SEO, J. H. & MITTAL, R. 2011 A sharp-interface immersed boundary method with improved mass conservation and reduced spurious pressure oscillations. *J. Comp. Phys.* **230**, 7347–7363.

SMYRNAIOS, D. N. & TSAMOPOULOS, J. A. 2001 Squeeze flow of Bingham plastics. *J. Non-Newton. Fluid Mech.* **100**, 165–190.

STIMSON, M. & JEFFERY, G. B. 1926 The motion of two spheres in a viscous fluid. *P. Roy. Soc. A-Math. Phy.* **111**, 110–116.

TABUTEAU, H., OPPONG, F. K., DE BRUYN, J. R. & COUSSOT, P. 2007 Drag on a sphere moving through an aging system. *Europhys. Lett.* **78**.

TAGAKI, S., OGUZ, H. N., ZHANG, Z. & PROSPERETTI, A. 2003 PHYSALIS: a new method for particle simulation part II: two-dimensional Navier–Stokes flow around cylinders. *J. Comp. Phys.* **187**, 371–390.

TAKASHI, NOMURA & HUGHES, THOMAS J.R. 1992 An arbitrary Lagrangian-Eulerian finite element method for interaction of fluid and a rigid body. *Comput. Method. Appl. M.* **95** (1), 115–138.

TANG, H. S., JONES, S. C. & SOTIROPOULOS, F. 2003 An overset-grid method for 3D unsteady incompressible flows. *J. Comp. Phys.* **191**, 567–600.

TANNER, R. I. 1993 Stokes paradox for power-law flow around a cylinder. *J. Non-Newton. Fluid Mech.* **50**, 217–224.

TATUM, J. A., FINNIS, M. V., LAWSON, N. J. & HARRISON, G. M. 2005 3-d particle image velocimetry of the flow field around a sphere sedimenting near a wall part 2. effects of distance from the wall. *J. Non-Newton. Fluid Mech.* **127**, 95–106.

TEZDUYAR, T. E., BEHR, M. & LIOU, J. 1992 A new strategy for finite element computations involving moving boundaries and interfaces – the deforming-spatial-domain/space-time procodure: I. The concept and the preliminary numerical tests. *Comput. Methods Appl. Mech. Engrg.* **94**, 339–351.

THOMPSON, R. L. & SOARES, E. J. 2016 Viscoplastic dimensionless numbers. *J. Non-Newton. Fluid Mech.* pp. 1–8.

TOKPAVI, D. L., JAY, P. & MAGNIN, A. 2009 Interaction between two circular cylinders in slow flow of Bingham viscoplastic fluid. *J. Non-Newton. Fluid Mech.* **157**, 175–187.

TOKPAVI, D. L., MAGNIN, A. & JAY, P. 2008 Very slow flow of Bingham viscoplastic fluid around a circular cylinder. *J. Non-Newton. Fluid Mech.* **154**, 65–76.

TRESKATIS, T., MOYERS-GONZÁLEZ, M. & PRICE, C. J. 2016 An accelerated dual proximal gradient method for applications in viscoplasticity. *J. Non-Newton. Fluid Mech.* **238**, 115–130.

TRESKATIS, T., ROUSTAEI, A., FRIGAARD, I. & WACHS, A. 2018 Practical guidelines for fast, efficient and robust simulations of yield-stress flows without regularisation: a study of accelerated proximal gradient and augmented Lagrangian methods. *J. Non-Newton. Fluid Mech.* **262**, 149–164.

UHLMANN, M. 2005 An immersed boundary method with direct forcing for the simulation of particulate flows. *J. Comp. Phys.* **209**, 448–476.

UHLMANN, M. & DOYCHEV, T. 2014 Sedimentation of a dilute suspension of rigid spheres at intermediate Galileo numbers: the effect of clustering upon the particle motion. *J. Fluid Mech.* **752**, 310–348.

UMEMURA, A. 1982 Matched-asymptotic analysis of low-Reynolds-number flow past two equal circular cylinders. *J. Fluid Mech.* **121**, 345–363.

VÁZQUEZ-QUESADA, A., TANNER, R. I. & ELLERO, M. 2016 Shear thinning of noncolloidal suspensions. *Phys. Rev. Lett.* **117**.

VIERENDEELS, J., DUMONT, K., DICK, E. & VERDONCK, P. 2005 Analysis and stabilization of fluid-structure interaction algorithm for rigid-body motion. *AIAA J.* **43** (12), 2549–2557.

VOWINCKEL, B., KEMPE, T. & FRÖHLICH, J. 2014 Fluid–particle interaction in turbulent open channel flow with fully-resolved mobile beds. *Adv. Water Resour.* **72**, 32–44.

WACHS, A. 2009 A DEM-DLM/FD method for direct numerical simulation of particulate flows: Sedimentation of polygonal isometric particles in a Newtonian fluid with collisions. *Comput. Fluids* **38**, 1608–1628.

WACHS, A. & FRIGAARD, I. A. 2016 Particle settling in yield stress fluids: limiting time, distance and applications. *J. Non-Newton. Fluid Mech.* **238**, 189–204.

WACHS, A., HAMMOUTI, A., VINAY, G. & RAHMANI, M. 2015 Accuracy of finite volume/staggered grid distributed Lagrange multiplier/fictitious domain simulations of particulate flows. *Comput. Fluids* **115**, 154–172.

WALTON, I. C. & BITTLESTON, S. H. 1991 The axial flow of a Bingham plastic in a narrow eccentric annulus. *J. Fluid Mech.* **222**, 39–60.

WAN, D. & TUREK, S. 2006 Direct numerical simulation of particulate flow via multigrid FEM techniques and the fictitious boundary method. *Int. J. Numer. Meth. Fl.* **51**, 531–566.

WANG, C. & ELDREDGE, J. D. 2015 Strongly coupled dynamics of fluids and rigid-body systems with the immersed boundary projection method. *J. Comp. Phys.* **295**, 87–113.

WILSON, K. C., HORSLEY, R. R., KEALY, T., REIZES, J. A. & HORSLEY, M. 2003 Direct prediction of fall velocities in non-Newtonian materials. *Int. J. Miner. Process.* **71**, 17–30.

YANG, J. & BALARAS, E. 2006 An embedded-boundary formulation for large-eddy simulation of turbulent flows interacting with moving boundaries. *J. Comp. Phys.* **215**, 12–40.

YANG, J. & STERN, F. 2012 A simple and efficient direct forcing immersed boundary framework for fluid-structure interactions. *J. Comp. Phys.* **231**, 5029–5061.

YANG, J. & STERN, F. 2015 A non-iterative direct forcing immersed boundary method for strongly-coupled fluid-solid interactions. *J. Comp. Phys.* **295** (779–804).

YU, Z. & WACHS, A. 2007 A fictitious domain method for dynamic simulation of particle sedimentation in Bingham fluids. *J. Non-Newton. Fluid Mech.* **145**, 78–91.

ZAHLE, F., JOHANSEN, J., SØRENSEN, N. N. & GRAHAM, J. M. R. 2007 Wind turbine rotor-tower interaction using an incompressible overset grid method. paper 2007-425. AIAA.

ZHANG, Z. & PROSPERETTI, A. 2003 A method for particle simulation. *ASME* **70**, 64–74.

ZISIS, T. & MITSOULIS, E. 2002 Viscoplastic flow around a cylinder kept between parallel plates. *J. Non-Newton. Fluid Mech.* **105**, 1–20.